Order Number 9021677

Deep localized hyperthermia with ultrasound-phased arrays using the pseudoinverse pattern synthesis method

Ebbini, Emad S. A., Ph.D.

University of Illinois at Urbana-Champaign, 1990

U·M·I
300 N. Zeeb Rd.
Ann Arbor, MI 48106

DEEP LOCALIZED HYPERTHERMIA WITH ULTRASOUND PHASED ARRAYS USING THE PSEUDOINVERSE PATTERN SYNTHESIS METHOD

BY

EMAD S. A. EBBINI

B.Sc., University of Jordan, 1985
M.S., University of Illinois, 1987

THESIS

Submitted in partial fulfillment of the requirements
for the degree of Doctor of Philosophy in Electrical Engineering
in the Graduate College of the
University of Illinois at Urbana-Champaign, 1990

Urbana, Illinois

UNIVERSITY OF ILLINOIS AT URBANA-CHAMPAIGN

THE GRADUATE COLLEGE

DECEMBER 1989

WE HEREBY RECOMMEND THAT THE THESIS BY

EMAD S. A. EBBINI

ENTITLED DEEP LOCALIZED HYPERTHERMIA WITH ULTRASOUND PHASED ARRAYS USING THE PSEUDOINVERSE PATTERN SYNTHESIS METHOD

BE ACCEPTED IN PARTIAL FULFILLMENT OF THE REQUIREMENTS FOR THE DEGREE OF DOCTOR OF PHILOSOPHY

Charles A Cain
Director of Thesis Research

N. Narayana Rao
Head of Department

Committee on Final Examination†

W O'Brien
Chairperson

Leon A. Frizzell

S. W. Lee

Charles A Cain

† Required for doctor's degree but not for master's.

O-517

ABSTRACT

One of the major limitations of hyperthermia as a cancer treatment modality is the lack of heating equipment and techniques capable of consistent therapeutic heating of deep-seated tumors. This thesis introduces a new pattern synthesis method capable of precisely controlling the power deposition level at a set of *control points* in the treatment volume using ultrasound phased arrays. This method, called the pseudoinverse pattern synthesis method, reduces the pattern synthesis problem to one of estimating the minimum-norm least-square solution to a matrix equation of the form, $\mathbf{Hu} = \mathbf{p}$, where $\mathbf{u}$ is the array excitation vector, $\mathbf{p}$ is the desired complex pressure at the control points, and $\mathbf{H}$ is a matrix propagation operator from the surface of the array to the control points. A useful solution to this problem is obtained when the number of control points is less than the number of elements of the array and the matrix $\mathbf{H}$ is full rank. This solution, called the minimum-norm solution, allows the array to be focused at several points simultaneously. This multiple-focus approach is important when ultrasound is used as a heating agent as it reduces the spatial-peak temporal-peak intensity required to generate a specified heating pattern. Furthermore, the minimum-norm solution allows the optimization of the array excitation efficiency and the intensity gain at the control points. These quantities are very significant for achieving deep localized heating with phased arrays. In fact, optimization of the intensity gain at the control points generally results in removal of high intensity interference patterns from the synthesized field. The removal of high intensity interference patterns eliminates one of the major disadvantages of multiple focusing. The pseudoinverse pattern synthesis method is introduced and discussed in detail. Simulation results are used to demonstrate its powerful capabilities as a pattern synthesis method. Its generality is demonstrated by the use of several different array structures to synthesize different multiple-focus patterns. Simulation results indicate that direct synthesis of multiple-focus patterns can provide an alternative to single-focus scanning. Finally, measured intensity profiles using a prototype cylindrical-section array agree well with theoretically predicted profiles.

ACKNOWLEDGEMENTS

I would like to sincerely thank my advisor, Professor Charles A. Cain, for the encouragement and support during the last three years and for giving me the opportunity to pursue both the theoretical and experimental aspects of the phased-array pattern synthesis problem. I learned a great deal from Dr. Shin-ichiro Umemura both on the theoretical and experimental aspects of ultrasound phased arrays. Thanks are due to Professor W. D. O'Brien, Jr., for his careful review of the thesis and his constructive remarks. I would also like to thank Professors Leon A. Frizzel and Shung-Wu Lee for their useful suggestions. This thesis research uses techniques and builds on concepts covered skillfully by Professors W. C. Chew, K. S. Arun and Hua Lee in their respective special topic classes.

The experimental work reported in this thesis is the result of team work which included a number of graduate and undergraduate colleagues. I would like to especially thank Francis Ngo for carrying out the design for the digital controller and amplifier circuits and the various tasks that he undertook to set up the experiment. Thanks are extended to Fred Heyman and Gregory Kerr for their excellent job in programming the digital driver and the stepper motor controller for ultrasonic measurements. The superb job of Bill McNeil and Scot Sprague in fabricating the cylindrical-section array prototype is greatly appreciated. I would also like to thank Joe Cobb for his careful calibration of the measurement probes. The acquisition of instrumentation and equipment for our laboratory was made much easier by Mrs. Wanda Elliott.

Finally, I would like to express my gratitude to the members of my family for their unlimited love and support through the years. Special thanks go to my brother Mukhles whose help and companionship made the last few months much more tolerable. I would also like to thank my friends and colleagues, Mohammad Nasir, Adel Marzougi and Ammar Kouki for helping me in preparing the final manuscript.

This work was supported in part by the National Institute of Health under Grant CA 44124, in part by the Hitachi Central research Laboratory, and in part by the National Center for Supercomputing Applications under Grant ECS 870001. The simulations presented herein were all obtained using the National Center for Supercomputing Applications CRAY XMP-48 supercomputer.

TABLE OF CONTENTS

CHAPTER 1

INTRODUCTION

Hyperthermia is a cancer treatment modality which aims at the preferential killing of malignant cells by elevating their temperatures to therapeutic levels for specified periods of time [1]. Historically, simple forms of hyperthermia were applied to small, nonulcerating cancers as early as 2000 B.C. More recently, spontaneous tumor regressions were observed in patients with illnesses associated with infectious fevers of about $40°C$ which lasted for several days [47]. In the late nineteenth century, Coley [32] administered measured doses of bacterial toxins to induce artificial fever in the treatment of malignant tumors. He reported disease-free survival of one to seven years in 3 of 17 inoperable carcinomas and 7 of 17 inoperable sarcomas [47].

More recent biological and clinical research accumulated clear evidence regarding the viability of hyperthermia as a cancer treatment modality [1, 2, 37, 41, 44]. Biological studies carried over in the last 15 years indicate clearly that mildly elevated temperatures have cytotoxic properties which are useful in the treatment of solid tumors [4]. This was attributed to the physical environment surrounding tumor cells which is characterized by nutritional depravation, low pH, and chronic hypoxia. Such conditions render tumor cells heat sensitive [1]. Furthermore, the tumor cell killing rate due to heating is enhanced by "heat-induced" vascular damage which reduces the blood flow in the tumor [36]. The combined effect of the hostile tumor

environment and the vascular damage during hyperthermia triggers a selective and irreversible inhibition of metabolism that correlates with a loss of malignancy, and ultimately to tumor regression [48].

Hyperthermia can be combined with other cancer treatment modalities such as radiation therapy and chemotherapy. Indeed, it has been suggested that combined heat and radiation therapy has a synergistic effect on the response of several tumors [44]. This is especially important since radiation therapy is the second most widely used cancer treatment modality and the introduction of any agent that can enhance its efficacy will have a significant positive effect on cure rates [1]. The combination of heat and several different cytotoxins is an active research area with promising results already evident [68, 69].

Hyperthermia can be administered to the whole body (systemic or whole-body hyperthermia) or to a specified volume of the body (regional hyperthermia). Regional hyperthermia, in turn, can include a volume which contains malignant and normal tissues or be confined to the tumor volume (localized hyperthermia). Depending on the depth of the tumor from the skin, hyperthermia can be classified as superficial or deep. Hyperthermia can be applied by various techniques, including fluid immersion (systemic hyperthermia), electric currents (interstitial, localized hyperthermia), and elctromagnatic and acoustic waves (noninvasive, localized hyperthermia). Among these techniques, electromagnetic and acoustic external beam heating techniques are the most attractive. Ultrasonic heating is based on the absorption of high energy waves by the tissue [70]. The particle velocity of the tissue created by the longitudinal waves causes frictional losses which convert mechanical energy into heat. Ultrasonic beams may be focused or unfocused, stationary or translocating. For deep heating applications, generally more than one transducer are used simultaneously to increase power deposition [4, 6, 7]. Multiple-transducer applicators can be used as phased arrays which allow electronic scanning of focused beams thus eliminating the need

for mechanical translocation of the applicator head. The absorption of electromagnetic waves in the tissue is due to conduction and displacement currents (function of conductivity and permittivity of the tissue). Microwaves offer the best heat localization among electromagnetic waves. However, a major disadvantage of microwave applicators is their limited usefulness to superficial heating because of the high attenuation coefficients (especially in fat). This is still a problem even with phased array microwave applicators where the penetration depth is on the order of 4 to 6 cm [31].

Despite the mounting evidence of the usefulness of hyperthermia, alone or in conjunction with other modalities, it is still far from being the physician's first choice as a cancer treatment modality. Among the reasons for the slow progress of hyperthermia in gaining wider acceptance in the clinic are failure to quantify the heat dose to provide a basis for the evaluation of the efficacy of this modality, the lack of heating equipment capable of consistent uniform heating of specified tumor volumes in the presence of tissue heterogeneities, and the lack of noninvasive temperature mapping equipment to provide the necessary feedback to account for the rapidly varying tumor environment.

The objective of this thesis is the investigation of noninvasive heating applicators and heating techniques capable of producing uniform consistent heating in deep-seated tumors. In other words, the emphasis is on noninvasive, deep, localized hyperthermia. For this type of application, focused ultrasound is clearly the preferred heating modality since it offers sufficient penetration depths for deep hyperthermia. Furthermore, the wavelength of ultrasonic waves at frequencies suitable for hyperthermia is small enough to provide small focal spots suitable for heat localization.

There exist several ultrasonic applicator systems for deep localized hyperthermia in clinical use [4, 7] or in preclinical trial phases [71]. All of these systems employ some kind of mechanical translocation of the applicator head to scan the beam(s)

around the tumor volume to achieve uniform heating. Encouraging results have been reported with these systems [4, 7] for a variety of tumor types, sizes, and locations. However, the need for a large bolus remains a serious problem with mechanically scanned applicator systems which can lead to cumbersome applicator-patient interface [25] or poor usage of the available acoustical windows due to extremely large applicator surface. The latter effect seriously limits these applicators' capabilities to localize heat inside the tumor volume.

Phased arrays can provide a useful alternative to mechanically scanned applicator systems since 1) the beam can be scanned electronically thus avoiding the need for mechanical scanning, 2) they can be designed to conform to the body portals for optimal use of available acoustical windows, and 3) with the proper pattern synthesis technique, useful heating patterns tailored to the tumor geometry can be easily generated and modified on line. These gains are achieved at the expense of using a larger number of elements with associated driving electronics. This factor is becoming less significant with the advent of low-power solid-state amplifiers. Moreover, the proper choice of the array structure and phasing technique can yield efficient applicators that can be realized with a moderate number of elements [8, 17]. Thus, ultrasound phased-array applicators can provide the most efficient heating of deep-seated tumors since they combine the ability of ultrasound for deep penetration with the flexibility of arrays to focus and steer beams at very fast rates.

The research conducted for this thesis emphasizes the investigation of new ultrasound phased array structures as potential deep, localized hyperthermia applicators. A new pattern synthesis method is introduced for precise control of the power deposition levels at a selected set of *control points* in the treatment volume. This method, called the *pseudoinverse pattern synthesis method*, proved useful in optimizing the array excitation efficiency and/or intensity gain for many useful heating patterns with different array structures. Simulated field profiles show that highly localized

heating patterns are possible using arrays with a moderate number of elements. Furthermore, preliminary experimental data from a prototype phased-array applicator show good agreement with theoretically predicted data obtained using the simulation algorithms.

The dissertation is organized into ten chapters. Chapter 2 defines and introduces some basic concepts relevant to deep, localized hyperthermia. Numerical algorithms used for this thesis research are described in Chapter 3. Chapter 4 describes some nonplanar phased array structures investigated as potential hyperthermia applicators in the course of this thesis research. Chapter 5 discusses the different methods of heating pattern generation with phased arrays. The pseudoinverse pattern synthesis method is introduced and discussed in Chapter 6. Chapter 7 discusses methods for improving the performance of a phased array in terms of some specified quantity, e.g., array excitation efficiency and intensity gain, based on the pseudoinverse method. This chapter also discusses the problem of optimal placement of control points for a specified pattern and the effect of quantization. Examples of simulated heating patterns obtained with different array structures are discussed in Chapter 8. A prototype cylindrical-section phased array is described in Chapter 9 along with the field measurement system. Finally, Chapter 10 summarizes the conclusions drawn from this work and provides some suggestions for future work.

CHAPTER 2

DEEP LOCALIZED HYPERTHERMIA: BASIC CONCEPTS

2.1 Deep Localized Hyperthermia

The objective of localized hyperthermia is to deliver sufficient power deposition levels to the tumor volume to insure therapeutic temperatures throughout the tumor for a specified period of time while maintaining low or controlled power deposition levels in the surrounding normal tissues. The current advent of diagnostic techniques enables the detection of tumors with diameters on the order of few centimeters. When small tumors are to be heated with external ultrasonic beams, the effective size of the beam has to be contained within the tumor volume in order to ensure heat localization. Hence, localization requirements prompt the use of focused ultrasonic beams for heating. In addition to heat localization, focusing is advantageous in combating the effect of attenuation when deep-seated tumors are to be treated. Furthermore, focusing can achieve high power deposition levels in the target volume while sparing the intervening normal tissues. For the purposes of this thesis, tumors located 7 cm or more beneath the skin are considered deep-seated. Tumors located deeper than 7 cm will necessarily require focused beams for efficient localized heating. Some applicator systems were designed to heat tumor sites from 10 cm [7] to 15 cm [6]. The phased arrays investigated in this thesis (to be introduced in Chapter 4) are

designed to cover this range of tumor sites.

2.2 Applicator Configurations

Single-transducer applicator systems were used with a reasonable degree of success in inducing localized hyperthermia in various types of tumors [4]. Focusing can be achieved with a lens attached to a disk transducer or by using shell transducers. The lens approach is used in the Scanned Intensity Modulated Focused Ultrasound (SIMFU) hyperthermia applicator system at MIT [4]. However, when deep-seated tumors are to be heated effectively, multiple-transducer applicator systems are more appropriate. This approach was used in constructing the multiple-transducer system for localized hyperthermia of deep tissues at Stanford [6]. This system utilizes 6 unfocused disk transducers mounted on a spherical shell such that their individual beams converge to the target volume near the geometrical center of the spherical shell. Therefore, the system is capable of providing the necessary gain for heating deep tumors. Unfortunately, this applicator configuration was not successful in localizing heating to the tumor volume and patient pain was reported to be a problem.

The multiple-transducer approach was also utilized in a scanned, focused system for localized hyperthermia constructed at the University of Arizona [7]. This system is a modification of a commercial diagnostic ultrasound scanner which has a gantry that can be translated, rotated and tilted by stepper motors. In addition to a set of diagnostic transducers, part of the original system, two high-power focused transducers were added to each side of the gantry. The gantry and the transducer assembly are immersed in a water bath on top of which the patient lies. This system has some useful features such as computer control of the gantry, existence of the diagnostic system for monitoring purposes, and the relative comfort of the patient during treatment. However, the large size of the transducer aperture (over 40 cm) necessitates locating the transducers far from the patient's body. This leads to poor utilization of the available acoustical windows and might render heat localization

difficult.

A more sophisticated multiple-transducer system is the Helios [71]. This system utilizes 30 lightly focused transducers mounted on a spherical surface in four coaxial rings containing 6, 6, 6, and 12 transducers. The transducer assembly is mounted on a gantry which is immersed on a water bath. Similar to the Arizona system, Helios directs ultrasonic beams upwards to the patient's body which is positioned on top of the water tank in the center of the treatment couch. The gantry has five degrees of freedom for flexibility of heating pattern generation under different treatment conditions.

It is evident that there is a general trend toward the utilization of multiple-transducer systems for deep, localized hyperthermia. Multiple-transducer applicators are needed for providing the necessary intensity gain at the target. Furthermore, the inhomogeneity of the treatment volume can be accounted for by independent control of the driving signals to the individual transducer. Therefore, the choice of phased arrays as heating applicators can be justified as a step in that direction. Several phased-array geometries were analyzed for potential use as hyperthermia applicators such as the linear array [24, 23], the annular array [16, 17], and the two-dimensional rectangular array [45]. These array structures were very similar to their counterparts used in ultrasonic imaging, except possibly for change of size. This was followed by the introduction of new applicator structures especially designed for hyperthermia such as the sector-vortex array [17], the cylindrical-section array [8, 9], and the spherical-section array described later in this thesis. Currently, only prototypes of phased-array applicators are being tested [43, 73, 74, 23]. The preliminary experimental data from these prototypes, however, are very encouraging. A prototype cylindrical-section array is described in Chapter 9.

Irrespective of the applicator configuration, basic definitions regarding acoustic wave propagation apply. The rest of this chapter develops the basic background for

acoustic wave propagation in homogeneous media and defines some of the terms that are frequently used in this thesis.

2.3 Radiation of Acoustic Waves from Baffled Sources

A linear, time-harmonic baffled source, $e^{j\omega t}$ time convention, radiating in an infinite, homogeneous, lossy medium produces a complex pressure field described by the Rayleigh-Sommerfeld diffraction integral

$$p(\mathbf{r}) = \frac{j\rho\omega}{2\pi}\int_{S'} u(\mathbf{r}')\frac{e^{-jk|\mathbf{r}-\mathbf{r}'|}}{|\mathbf{r}-\mathbf{r}'|}dS' \tag{2.1}$$

where $j = \sqrt{-1}$, ρ is the density of the medium, $k = w/c = k_o - ja$ is the complex propagation constant (a is the attenuation coefficient), S' is the surface of the source, u is the particle velocity normal to the surface of the source, and $\mathbf{r}$ and $\mathbf{r}'$ are the observation and source points, respectively.

The power deposition at $\mathbf{r}$ due to the radiating source is given by [18]

$$Q(\mathbf{r}) = \alpha\frac{p^*(\mathbf{r})p(\mathbf{r})}{\rho c}, \tag{2.2}$$

where α is the absorption coefficient in the medium, and the asterisk (*) denotes complex conjugation. Generally, $\alpha < a$, i.e., absorption is less than attenuation in biological media [39, 72].

2.4 Focusing

As mentioned above, focusing of acoustic waves can be achieved with lenses, shell transducers, or with phased arrays. For shell transducers, e.g., spherical and cylindrical, the focus forms at or near the geometric center of the shell. Ultrasonic focusing lenses are generally planoconcave attached to a vibrating piston, e.g., a disk, from one side to produce convergent wavefronts that form caustics at points determined by the lens design. In the case of phased arrays, a focus can be formed by driving the array elements with signals phase shifted with respect to each other in such a way that the individual beams from the array elements add constructively at

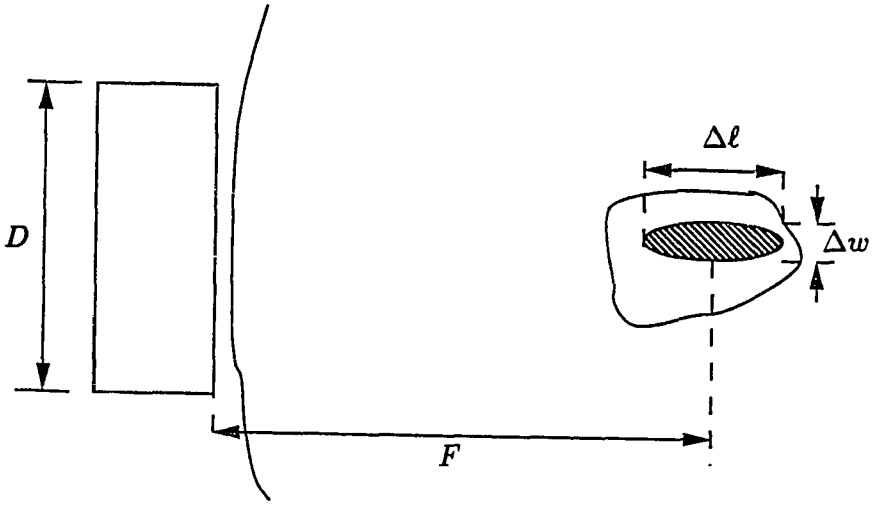

Figure 2.1. A generic focusing system with aperture D and focused at a single point with fo. al length F.

the desired focal point. Figure 2.1 shows a generic focusing structure with aperture size D used to produce a focal spot at a distance F from the surface. The 6-dB dimensions of the focal spot in the longitudinal, $\Delta\ell$, and transverse, Δw, are given by

$$\Delta\ell = K_1\lambda\left(\frac{F}{D}\right)^2 \tag{2.3}$$

and

$$\Delta w = K_2\frac{\lambda F}{D} \tag{2.4}$$

where λ is the wavelength of the propagated sound field and K_1 *and* K_2 are constants determined by the geometry of the focusing transducer. For $\frac{F}{D} < 1$ (typical of hyperthermia transducers), Δw is on the order of $1 - 2\lambda$ and $\Delta\ell$ is on the order of $3 - 10\lambda$.

This chapter is concluded with a series of definitions of terms frequently used throughout this thesis. Definitions of acoustical quantities and dimensions of focal beams are based on definitions used in [51].

The *focal spot* is the volume surrounding the focal point of a focused transducer

defining the 6-dB dimensions of the focal beam. The focal spot is often associated with a point-focus where the transducer (shell, lens, or array) is focused at a single point. In this thesis, however, this term will also be used for shaped or diffuse foci which are possible using phased arrays and special lenses.

The *f number* of a focused transducer is the ratio of the focal length, F, to the aperture, D, of the transducer. (See Figure 2.1.)

The *spatial-peak temporal-average* intensity at the focus of a time-harmonic radiating source is given by

$$I_{SPTA} = \frac{p^*(\mathbf{r}_f)p(\mathbf{r}_f)}{2\rho c}, \tag{2.5}$$

where $\mathbf{r}_f$ defines the focal point. When the source is driven by a periodically gated sinusoid, the *spatial-peak pulse-average* is given by

$$I_{SPPA} = \frac{p^*(\mathbf{r}_f)p(\mathbf{r}_f)}{2\rho c}, \tag{2.6}$$

where the time average is taken over the pulse duration. Hence, the time-average intensity is related to the pulse-average intensity as follows:

$$I_{SPTA} = \frac{\tau I_{SPPA}}{T} \tag{2.7}$$

where τ and T are the duty cycle and the period of the gating function, respectively.

The *spatial-average time-average* intensity, I_{SATA}, of a beam is the time-average acoustical signal averaged over the effective cross section of the beam (defined by the 6-dB lateral dimensions).

The *spatial-peak temporal-peak* intensity, I_{SPTP}, is the highest peak value of the instantaneous intensity at a spatial peak. It is given by

$$I_{SPTP} = \frac{p_m^2}{\rho c} \tag{2.8}$$

where p_m is the maximum instantaneous pressure.

The *intensity gain* at the focal point of a transducer is given by

$$G = \frac{I_{SPTA}}{I_{SATA,T}} \tag{2.9}$$

where $I_{SATA,T}$ is the spatial-average time-average intensity over the transducer surface. A general formula for the intensity gain of a focused transducer is given by (see Figure 2.1)

$$G = K_3 \left(\frac{D^2}{\lambda F} \right)^2 . \tag{2.10}$$

The following definitions are for a phased-array transducer consisting of N elements having an arbitrary geometry. The elements of the array are assumed to be driven by independent time-harmonic signals.

The *array excitation vector*, $\mathbf{u}$, is an N-element vector of complex numbers, $\mathbf{u} = [u_1, u_2, \ldots, u_N]^t$, describing the particle velocity at the surface of each array element. The particle velocity at the surface of the ith array element is given by $u_i = a_i e^{j\phi_i}$ where a_i and ϕ_i are the amplitude and phase, respectively.

The *array excitation efficiency*, η_A, is given by

$$\begin{aligned} \eta_A &= \frac{< \mathbf{u}, \mathbf{u} >}{N U_{max}^2} \times 100\% \\ &= \frac{\sum_{i=1}^{N} u_i^* u_i}{N U_{max}} \times 100\%, \end{aligned} \tag{2.11}$$

where U_{max} is the maximum amplitude particle velocity at the surface of the array, and $< \cdot, \cdot >$ defines the inner product of two complex column vectors.

CHAPTER 3

COMPUTER SIMULATIONS

3.1 General

The theoretical analysis of ultrasound hyperthermia applicator systems requires the numerical simulation of field patterns resulting from a known distribution of particle velocity at the applicator surface. When the applicator is radiating in an infinite homogeneous medium, Equation (2.1) can be used for the evaluation of the complex pressure field. The power deposition, $Q(\mathbf{r})$, is then given by Equation (2.2).

The power deposition profile in the treatment volume is responsible for heat generation and consequently temperature elevation in the target volume. The most common representation of the spatial and temporal distributions of temperature in living systems is the *bio-heat transfer equation* (*BHTE*) [70]. This equation takes the general form

$$\rho C \frac{\partial T}{\partial t} = \nabla \cdot (K \nabla T) - W_b C_b (T - T_a) + Q, \tag{3.1}$$

where T is the tissue temperature, K is the intrinsic thermal conductivity of tissue, W_b is the blood perfusion rate, C_b is the specific heat of the blood, and T_a is the arterial blood temperature. The *BHTE* models the thermal response of the tissues in the treatment volume to the heating stimulus, Q [19].

This chapter describes the numerical models used for the ultrasonic fields and

thermal response computations. It also illustrates the numerical discretization algorithms for the Rayleigh-Sommerfeld integral and the $BHTE$.

3.2 Ultrasonic Field Computations

The acoustic signal in the region of interest is assumed to be generated by an array of transducers radiating in an infinite homogeneous (possibly lossy) medium. By superposition, the total complex pressure due to an N-element array is given by

$$p(\mathrm{r}) = \frac{j\rho ck}{2\pi} \sum_{n=1}^{N} u_n \int_{S'_n} \frac{e^{-\jmath k|\mathrm{r}-\mathrm{r}'_n|}}{|\mathrm{r}-\mathrm{r}'_n|} dS'_n \tag{3.2}$$

where u_n is the particle velocity at the surface of the nth element of the array. All array structures analyzed in this thesis are composed of rectangular elements. These arrays are not assumed to be planar hence computing the pressure field by transform methods, e.g., Fourier transform, is generally inefficient. The rectangular radiator method [24, 51] is an efficient numerical technique for computing the complex field at a point of observation due to a rectangular continuous wave source surrounded by a plane rigid baffle. A detailed description of the method can be found in [51]. A brief description of the method given here is slightly modified (notation only) from Ocheletree's description [51] for purposes of this thesis.

The method assumes that the rectangular element is baffled in the (x, z) plane and radiates into the $y > 0$ half-space with the (x, y, z) coordinate system centered at the center of the element (see Figure 3.1). For an observation point at x, y, z, the element is divided into subelements with dimensions (Δw) and (Δh) small enough for the observation point to be considered in the far field of the subelement. Assuming that the particle velocity is uniform over the surface of the subelement, the complex pressure at the observation point due to the subelement, centered at $(x_s, 0, z_s)$, can be given by

$$p_{sub} = \frac{j\rho ck}{2\pi} \frac{\Delta w \Delta h u e^{-\jmath kR}}{R} \operatorname{sinc}\frac{k(x-x_s)\Delta w}{2R} \operatorname{sinc}\frac{k(z-z_s)\Delta h}{2R} \tag{3.3}$$

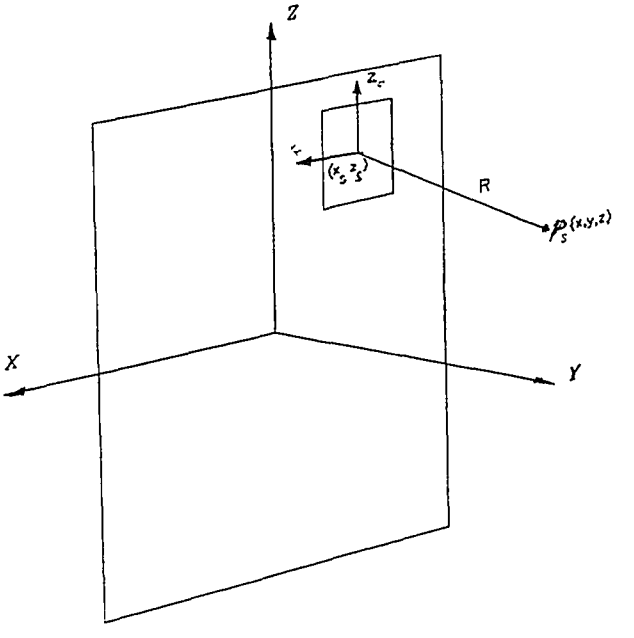

Figure 3.1. Coordinate system and geometry used for the rectangular radiator method.

where R is the distance from the center of the subelement to the observation point. The total pressure at the observation point is the sum of the pressures produced by all the subelements covering the surface of the element.

As seen above, the complex pressure due to a subelement can be computed easily when the observation coordinate system is centered at the element. However, for a nonplanar array geometry, the observation coordinate system is not centered at the elements of the array. Therefore, it is necessary to transform the observation point from the observation coordinate system to the element coordinate system using the general transformation

$$\mathbf{r}_n = \mathbf{T}_n \mathbf{r} + \mathbf{t}_n \tag{3.4}$$

where $\mathbf{T}_n$ and $\mathbf{t}_n$ are rotation and translation operators associated with the nth element of the array. The specific form of these operators is determined by the element's orientation and location with respect to the center of the observation coordinate system. These operators will be given explicitly for the different array structures analyzed in this thesis.

3.3 Thermal Computations

The thermal response of the tumor and the surrounding tissues to a power deposition profile produced by a time average acoustic field can be simulated by solving the *BHTE* in rectangular coordinates. Figure 3.2 shows a cross section of the thermal model used in the simulations. The model parameters are assumed to be a function of depth only and are constant in the lateral dimensions. The tumor is assumed to be spherical in shape and to have the same blood perfusion as the normal tissue. The latter assumption is a departure from the common modeling of a tumor as a multilayered sphere with a necrotic core (which makes it easier to heat the tumor.) If the tumor is indeed necrotic, then this approach results in underestimating the temperature levels inside the tumor.

The transient *BHTE* can be solved numerically by discretizing the temporal

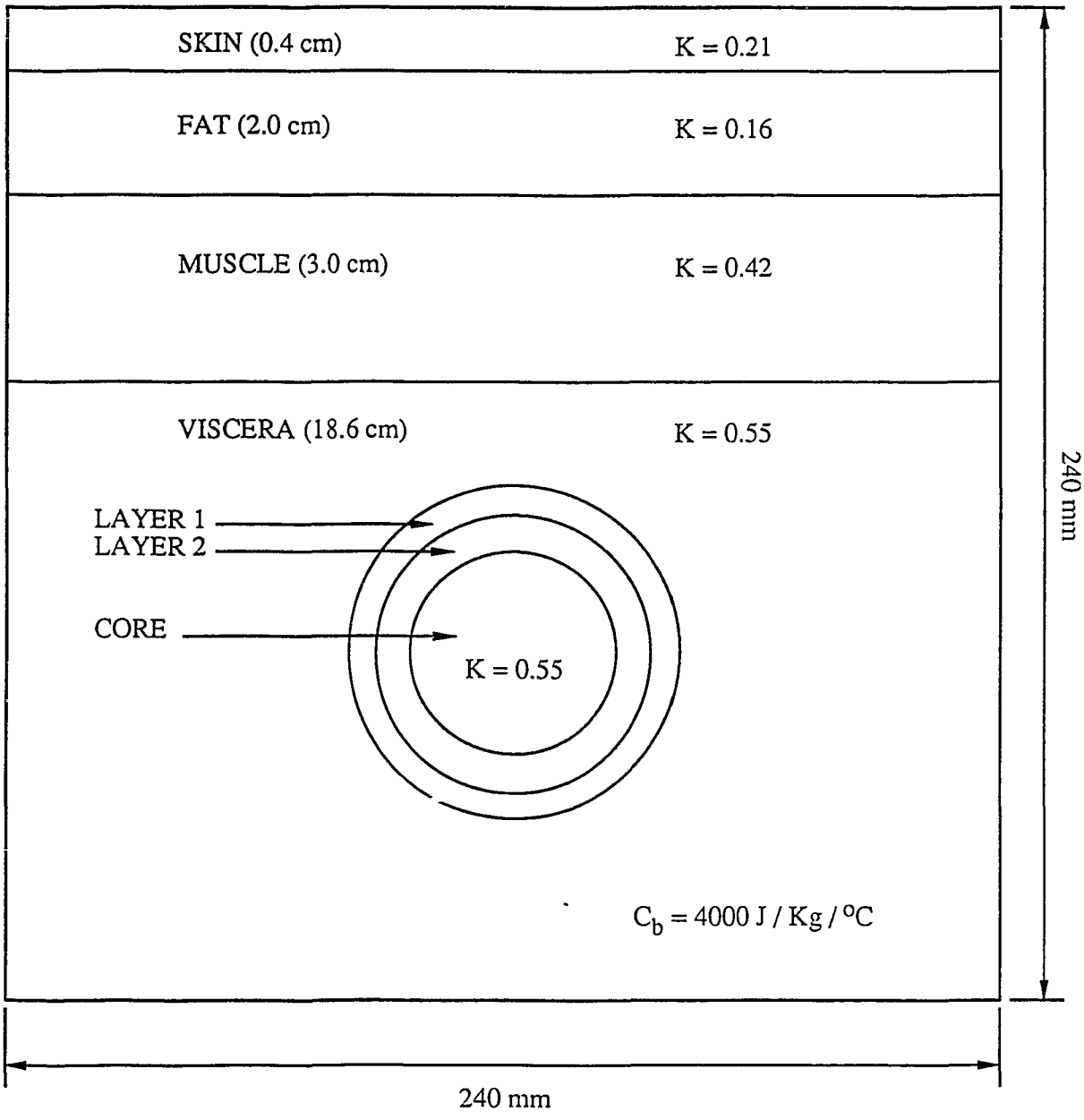

Figure 3.2. A cross section of the thermal model used for temperature simulations.

and spatial partial derivatives using the finite difference method. A conditionally stable solution for this equation can be obtained when the central difference in space and the forward difference in time are used [62, 63]. Solving the transient $BHTE$ is useful for the evaluation of the heating rate at the beginning of the treatment, the presence of temperature fluctuations in the tumor due to slow scanning speed, and thermal dose computations. However, if one is interested only in determining whether a specified heating pattern is capable of inducing therapeutic temperatures within the tumor volume, then solving the steady-state $BHTE$ would suffice. That is, one would need to solve

$$\nabla \cdot (K \nabla T) - W_b C_b (T - T_a) + Q = 0. \tag{3.5}$$

The discretization of this equation begins by expressing the spatial derivative in Cartesian coordinates

$$\nabla \cdot (K \nabla T) = \frac{\partial}{\partial x} K \frac{\partial T}{\partial x} + \frac{\partial}{\partial y} K \frac{\partial T}{\partial y} + \frac{\partial}{\partial z} K \frac{\partial T}{\partial z}. \tag{3.6}$$

Utilizing the fact that the thermal model parameters are independent of the lateral dimensions

$$\nabla \cdot (K \nabla T) = K(y) \frac{\partial^2 T}{\partial x^2} + \frac{\partial}{\partial y} K(y) \frac{\partial T}{\partial y} + K(y) \frac{\partial^2 T}{\partial z^2}. \tag{3.7}$$

Letting $T(x, y, z) = T_{m,n,p}$ and $K(y) = K_{m,n,p}$ at a grid point $x = m\Delta x, y = n\Delta y,$ *and* $z = p\Delta z$, and using central differencing, the partial derivatives can be written as

$$K(y) \frac{\partial^2 T}{\partial x^2} = \frac{K_{m,n,p}}{(\Delta x)^2} [T_{m+1,n,p} - 2T_{m,n,p} + T_{m-1,n,p}] \tag{3.8}$$

$$\begin{aligned} \frac{\partial}{\partial y} K(y) \frac{\partial T}{\partial y} &= \frac{1}{(\Delta y)^2} \Big\{ K_{m,n+\frac{1}{2},p} T_{m,n+1,p} - [K_{m,n+\frac{1}{2},p} + K_{m,n-\frac{1}{2},p}] T_{m,n,p} \\ &\quad + K_{m,n-\frac{1}{2},p} T_{m,n-1,p} \Big\} \end{aligned} \tag{3.9}$$

$$K(y) \frac{\partial^2 T}{\partial z^2} = \frac{K_{m,n,p}}{(\Delta z)^2} [T_{m,n,p+1} - 2T_{m,n,p} + T_{m,n,p-1}]. \tag{3.10}$$

For the case $\Delta x = \Delta y = \Delta z = \Delta s$, straightforward algebraic manipulation yields the discretized version of the steady-state $BHTE$

$$T_{m,n,p} = \frac{\Gamma + (\Delta s)^2(Q_{m,n,p} + W_b C_b T_a)}{4K_{m,n,p} + K_{m,n-1,p} + K_{m,n-1,p} - (\Delta s)^2 W_b C_b}, \tag{3.11}$$

where

$$\begin{aligned} \Gamma &= K_{m,n,p}(T_{m+1,n,p} + T_{m-1,n,p} + T_{m,n,p+1} + T_{m,n,p-1}) \\ &\quad + K_{m,n+1,p}T_{m,n+1,p} + K_{m,n-1,p}T_{m,n-1,p}. \end{aligned} \tag{3.12}$$

In the discretized equation, the following substitutions were made

$$K_{m,n+\frac{1}{2},p} = K_{m,n+1,p} \tag{3.13}$$

and

$$K_{m,n-\frac{1}{2},p} = K_{m,n-1,p}. \tag{3.14}$$

The over-relaxation version of the discretized $BHTE$ is given by

$$T^{[i]}_{m,n,p} = \omega \frac{\Gamma + (\Delta s)^2(Q_{m,n,p} + W_b C_b T_a)}{4K_{m,n,p} + K_{m,n-1,p} + K_{m,n-1,p} - (\Delta s)^2 W_b C_b} + (1-\omega)T^{[i-1]}_{m,n,p}, \tag{3.15}$$

where $1 < \omega < 2$ is the over-relaxation parameter and $[i]$ denotes the ith iteration. The successive over-relaxation technique achieves faster convergence rates when the parameter ω is chosen properly. The choice of ω depends on the grid size and the spatial distribution of the stimulus Q and is determined experimentally. The convergence criterion was chosen such that

$$\max_{\forall m,n,p} |T^{[i]}_{m,n,p} - T^{[i-1]}_{m,n,p}| \leq 10^{-6}. \tag{3.16}$$

The discretization of the transient $BHTE$ uses central differencing spatially and forward differencing temporally. Letting $T(x,y,z,t) = T^l_{m,n,p}$ at a grid point $x = m\Delta x, y = n\Delta y, z = p\Delta z$ and time instant $t = l\Delta t$, and using forward differencing, the temporal partial derivative can be written as

$$\rho C \frac{\partial T}{\partial t} = \rho C \frac{T^{l+1}_{m,n,p} - T^l_{m,n,p}}{\Delta t}. \tag{3.17}$$

The right-hand side of the transient $BHTE$ is discretized similarly to the above procedure used for the steady-state $BHTE$. After simple algebra, the discretized version of the transient $BHTE$ takes the following form

$$T^{l+1}_{m,n,p} = \frac{\Delta t}{\rho C}\left\{\frac{\Gamma^l - (4K_{m,n,p} + K_{m,n+1,p} + K_{m,n-1,p})T^l_{m,n,p}}{(\Delta s)^2} - W_b C_b (T^l_{m,n,p} - T_a) + Q^l_{m,n,p}\right\} + T^l_{m,n,p}, \tag{3.18}$$

where Γ^l is same as Γ given above with temporal dependence explicitly shown.

CHAPTER 4

NONPLANAR PHASED-ARRAY STRUCTURES

4.1 General

The use of phased arrays as hyperthermia applicators will lead to more versatile applicator systems which should help ultrasound gain wider acceptance in the clinic. The ability of phased arrays to scan focused beams around the tumor volumes without the need for physically moving the applicator head should greatly simplify the machine-patient interface. This is extremely important since hyperthermia sessions can be expected to last up to 30-60 min. Furthermore, for deep hyperthermia, a phased array applicator can be brought very close to the patient's body, thus allowing optimal use of the available acoustical windows. Therefore, it is clear that a significant improvement in the efficacy of an ultrasonic hyperthermia system can be achieved if mechanical scanning can be replaced by electronic scanning. However, electronic scanning is typically associated with problems that are not encountered when mechanical scanning is used. Specifically, as the beam is scanned away from the axis of the array, a reduction of intensity gain at the focus typically occurs. The loss of intensity gain at the focus due to scanning can limit the ability of a phased array to effectively heat deep tumors. Another problem associated with scanning, especially with uniform-lattice arrays, is the formation of grating lobes away from the focus. The size and location of the grating lobe associated with a scanned focus

puts limits on the size of tumor that can be treated with a specified array. Hence, for a phased array to provide a viable alternative to a mechanically scanned applicator, scanned beams generated by this array have to have sufficient intensity gain at every point along the scan path. In addition, grating lobes, if any, should not exceed a specified intensity level with respect to the main focus lest they cause hot spots outside the tumor volume. This must be achieved with the minimum possible number of elements in order for the applicator to be realized at reasonable cost and to reduce the complexity of the driving electronics.

4.2 Design Criteria for Phased-Array Applicators

Ultrasonic wave propagation inside the body is significantly affected by tissue inhomogeneities. In fact, deep penetration of ultrasonic waves into the tissues is possible only in regions void of bone structures or gas spaces (known as acoustical windows). Clearly this requires that several different highly specialized applicators be available in the clinic for treating different tumor types at different locations in the body. Ultimately, a generation of conformal array designs should evolve for achieving optimal hyperthermia treatments at different tumor locations.

Assuming that the therapist has a variety of applicators to choose from for treating a deep-seated tumor, his or her choice of specific applicator design will probably be guided by the following considerations:

1. *Applicator Size*

   The location of the tumor determines the available acoustical window. The therapist must choose the largest possible applicator for this window to ensure maximum possible intensity gain. The focal depth F (see Equations (2.3), (2.4) and (2.10)) is determined.

2. *Operation Frequency*

   The depth of the tumor and the attenuation/absorption values in the tissue

determine the operation frequency (wavelength). Using Equation (2.10), the size of the transducer is determined (the parameter D).

3. *Applicator Geometry*

   The size and shape of the tumor determines the maximum scan depth and angle around the tumor. These factors determine the maximum acceptable $\Delta\ell$ [4] (see Equation (2.3)), the the maximum acceptable intensity gain loss and maximum grating lobe level to ensure efficient localized heating. The geometry of the applicator is chosen to satisfy these requirements.

4.3 Nonplanar Phased Arrays

This chapter introduces three nonplanar phased-array applicator structures that could offer some advantages over their planar counterparts. Single-focus field patterns are used in demonstrating the capabilities of these arrays and how they compare with planar arrays with an equal number of elements and equivalent surface area. This approach is helpful in understanding the basic properties of phased arrays as scanning applicators. As will be shown in Chapter 6, multiple-focus field patterns can be generated with phased arrays. In general, the characteristics of a phased array as a single-focus scanner remain unchanged when it is used as a multiple-focus scanner.

4.3.1 The 1D cylindrical-section phased array

Figure 4.1 shows a schematic isometric view of the 1D cylindrical-section phased array, henceforth referred to as the CSA1D. A complete analysis of this array is given in [8, 9]. This section describes the array geometry, the characteristic focus of this array, and a steered-focus beam pattern. The performance of any phased array as a hyperthermia applicator can be evaluated by investigating the relation between its geometric focus and shifted focus. The geometric and shifted foci are compared in terms of intensity gain, size and shape, and the relative intensity of the grating lobe.

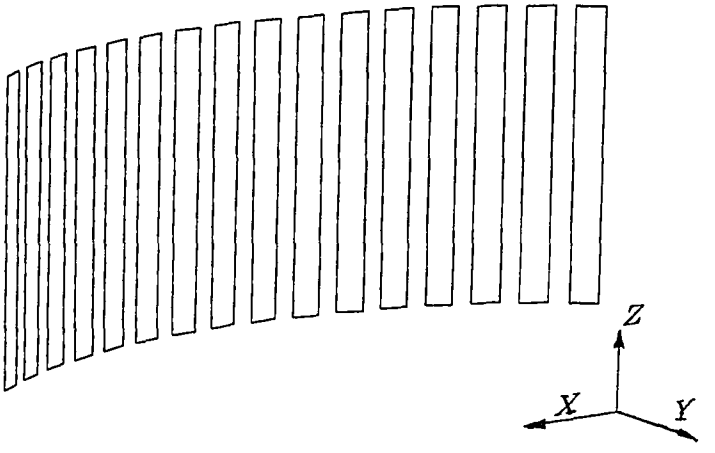

Figure 4.1. Isometric view of the 1D cylindrical-section array.

Array Geometry

Figure 4.2 shows a cross section of the CSA1D. The array consists of N rectangular elements distributed uniformly inside the circular surface of a cylindrical wedge of radius R, angular opening $2\phi_o$ and height h. The array is assumed to be symmetrical around the (x,y) plane, i.e., rectangular elements extend from $z = -h/2$ to $z = h/2$. For convenience of presentation, the origin of the (x,y) coordinate system coincides with the geometric center of the array. The angle between the centers of two consecutive elements is $\theta_o = 2\phi_o/N$. The center-to-center spacing between two consecutive elements is $d_c = 2R\sin(\theta_o/2)$, which also defines the maximum element width, w. The center of the nth element makes an angle $\theta_n = \theta_o(n - N)/2$ with the x-axis. The distance between the center of each array element and the center of the array is $r_c = R\cos(\theta_o/2)$. The lateral aperture of the array is given by the chord length, $D = 2R\sin(\phi_o)$, and the elevation aperture is equal to the height h.

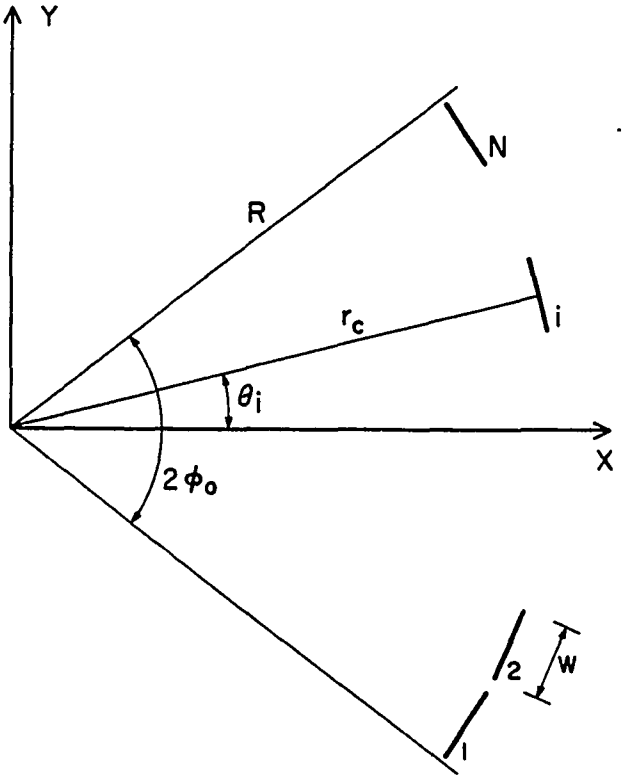

Figure 4.2: Cross section of the CSA1D.

The contribution of the nth array element to the complex pressure at an observation point defined by $\mathbf{r} = [x, y, z]^t$ can be computed using the rectangular radiator method. This can be most conveniently performed by transforming the observation point to the coordinate system centered at the nth element. Under this transformation, the point at $\mathbf{r}$ will be transformed to the point $\mathbf{r}_n = [x_n, y_n, z_n]^t$ according to

$$\mathbf{r}_n = \begin{pmatrix} \cos(\theta_n) & -\sin(\theta_n) & 0 \\ -\sin(\theta_n) & -\cos(\theta_n) & 0 \\ 0 & 0 & 1 \end{pmatrix} \cdot \mathbf{r} + \begin{pmatrix} 0 \\ r_c \\ 0 \end{pmatrix}. \tag{4.1}$$

This equation defines the operators $\mathbf{T}_n$ and $\mathbf{t}_n$ in Equation (3.2).

The Characteristic Focus

The characteristic focus of the array can be obtained by driving all array elements with uniform phase and amplitude distribution. In this case, the array behaves as a cylindrical shell which focuses energy at its geometrical center. An approximate

analytical expression was derived for a dense array of radius R, angular opening $2\phi_o$, and consisting of N point sources each of infinitesimal area δA, with $R >> \lambda$ [9]. The complex pressure in the vicinity of the center of the array can be expressed as a series of the form

$$p(r,\theta) = \frac{j\rho ck}{2\pi}(N\delta A)\frac{e^{-jkR}}{R}u_o\left[J_o(kr) + \frac{2}{\phi_o}\sum_{n=1}^{\infty} j^n \frac{J_n(kr)}{n}\sin(n\phi_o)\cos(n\theta)\right] \quad (4.2)$$

where j, ρ, c, k are as in Equation (2.1) and the medium is assumed to be lossless, u_o is the amplitude of the particle velocity of each point source, J_n is the nth-order Bessel function of the first kind, and r *and* θ are the polar coordinates at the center of the array in the (x, y) plane. A dense array of point sources with a radius $R = 200$ mm was simulated in a lossless medium and results were compared to those obtained analytically by the above series form. The resulting intensity profiles suggest that the simulated values are in good agreement with analytical values for values of $kr < 0.1kR$ [9].

The array described above was then simulated with $R = 200$ mm, $2\phi_o = 75°$, $N = 80$, $f = 500$ kHz, $w = 3$ mm, and $h = 50$ mm. The speed of sound was assumed to be 1500 m/s and the attenuation in the medium was 1 dB/cm/MHz. Figure 4.3 shows the intensity profile of the characteristic focus in the $z = 0$ plane and along a line passing through the array center in the elevation direction. The dimensions of the focal spot for the characteristic focus of this array are $\Delta w = 3.3$ mm, $\Delta\ell = 12$ mm, and $\Delta z = 30$ mm. The intensity profile of the characteristic focus in the elevation direction is determined by the Fresnel diffraction phenomenon as one might expect. Finally, the intensity gain at the characteristic focus of the CSA1D is 15.1 dB. Considering the dimensions of the CSA1D described herein, this value of intensity gain is sufficient for obtaining focal intensity levels capable of therapeutic heating of many realistic size tumors at depth.

Steered-Focus Patterns

The phase distribution of the driving signals to the array elements can be set such

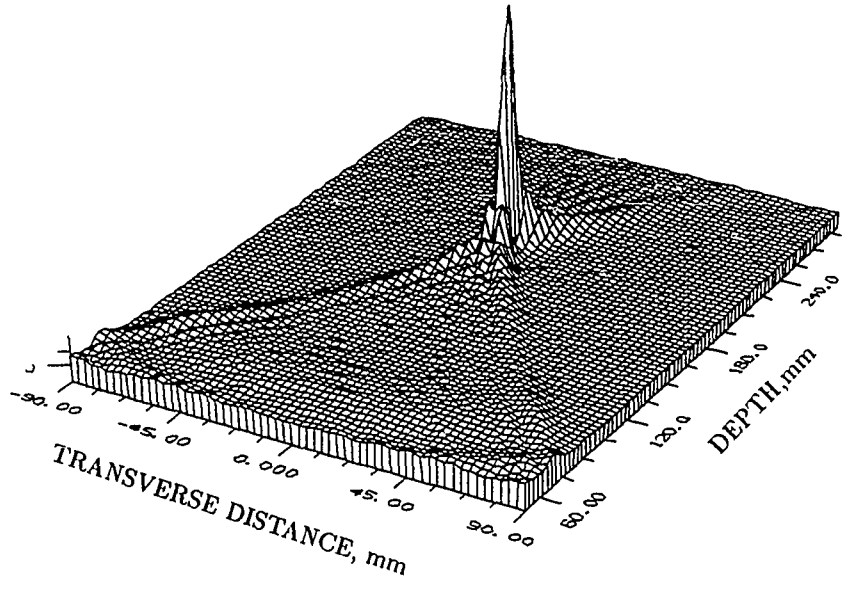

a) $z = 0$ plane.

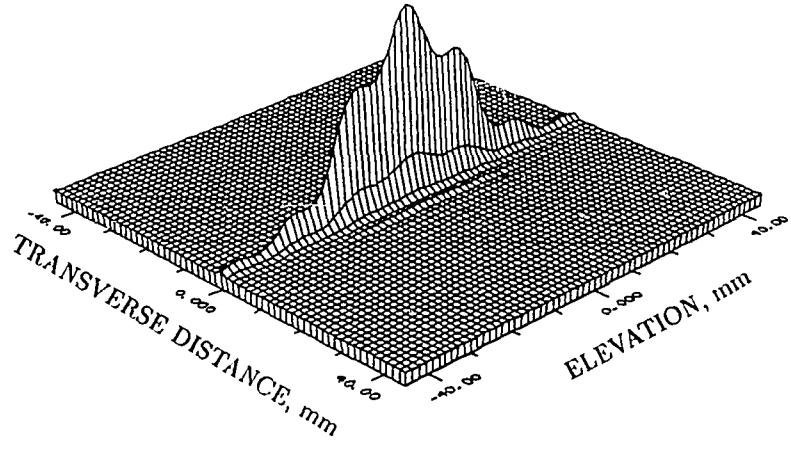

b) Focal plane.

Figure 4.3. Intensity profiles of the characteristic focus of the CSA1D.

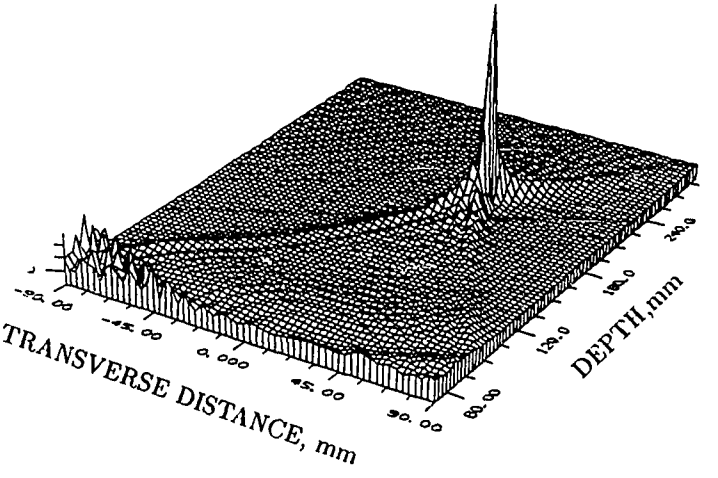

Figure 4.4: Intensity profile of a shifted focus produced by the CSA1D.

that a focus can be formed at any desired point within the near field of the aperture. In reference to Figure 4.2, the array can be focused at a point P, with coordinates (x_f, y_f) by computing the distances $d_i, i = 1, 2, \ldots, N$ between the focal point and the ith element of the array. The corresponding phase shift of the driving signal of the ith array element is given by

$$\begin{aligned} \phi_i &= -\frac{\omega_o d_i}{c} \\ &= -\frac{\omega_o \sqrt{r_f^2 + r_c^2 - 2 r_f r_c \cos(\theta_f - \theta_i)}}{c} \end{aligned} \tag{4.3}$$

where $r_f = \sqrt{x_f^2 + y_f^2}$, and $\theta_f = \arctan(y_f / x_f)$.

The array described above was focused at a point P, at depth 200 mm and transverse distance 30 mm from the center of the array. Figure 4.4 shows the resulting intensity profile. This case represents a typical steered focus to be utilized in a scanning situation. The size and shape of the focal spot at P are essentially unchanged

when compared to those of the characteristic focus. Furthermore, the intensity gain at this focus is 14.6 dB which is only 0.5 dB below the intensity gain at the characteristic focus. Hence, the CSA1D preserves the shape, size, and intensity gain of the focal spot as the beam is steered off the axis of symmetry of the array. This property makes the CSA1D a very useful spot-scanning applicator system when scanning is confined to transverse and longitudinal directions.

Comparison with the Linear Phased Array

A comparison between the CSA1D and a linear phased array with 80 elements each of which has $w = 3$ mm and $h = 50$ mm, i.e., equivalent surface area and center-to-center spacing was reported in [8]. The CSA1D typically produces focal intensity gains nearly 3 dB higher than those of the linear array (with $F/D = 0.83$ fixed for both arrays). Furthermore, the relative intensity level of the grating lobes generated by the linear array is 4 dB higher than that generated by the CSA1D. These results show clearly that the CSA1D outperforms the linear array as a spot-scanning hyperthermia applicator.

4.3.2 The 2D cylindrical-section phased array

The cylindrical geometry of the CSA1D proved very useful in the generation of highly focused beams suitable for deep localized heating. However, the CSA1D is limited to scanning in the transverse and longitudinal directions and cannot scan the beam in the elevation direction. Such a limitation can be removed by dissecting the elements of the cylindrical-section array in the elevation direction thus creating a two-dimensional array. The 2D cylindrical-section array, CSA2D, is capable of scanning focused beams in three dimensions, hence providing more precise control over the heating pattern. Figure 4.5 shows an isometric view of the CSA2D.

Array Geometry

The array consists of N rectangular elements each of width w and height h distributed in N_r rows and N_c columns ($N = N_r \times N_c$) over the circular surface of

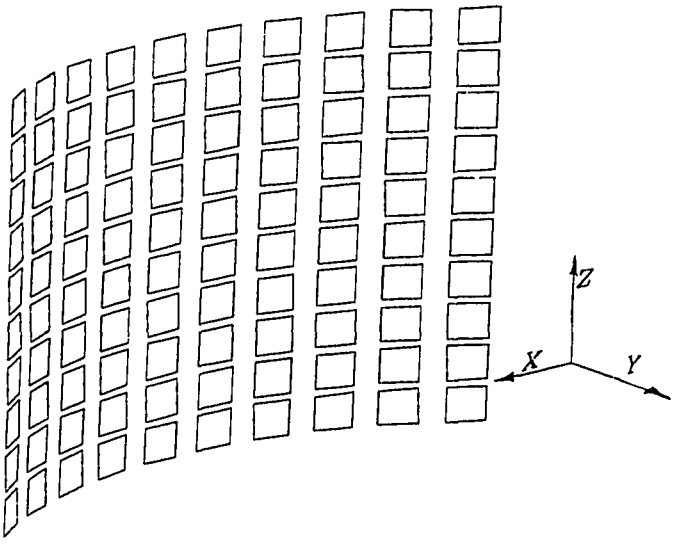

Figure 4.5: Isometric view of the CSA2D.

a cylindrical wedge of radius R, angular opening $2\phi_o$, and height $H = N_c h$. Each row of elements has a cross section as that shown in Figure 4.2 with N replaced by N_r. The contribution of the nth element of the array (located at the n_rth row and n_c column) to the complex pressure at an observation point defined by $\mathbf{r} = [x, y, z]^t$ can be computed using the rectangular radiator method. The transformation needed according to Equation (3.2) is

$$\mathbf{r}_n = \begin{pmatrix} \cos(\theta_{n_c}) & -\sin(\theta_{n_c}) & 0 \\ -\sin(\theta_{n_c}) & -\cos(\theta_{n_c}) & 0 \\ 0 & 0 & 1 \end{pmatrix} \cdot \mathbf{r} + \begin{pmatrix} 0 \\ r_c \\ h(n_r - (N_r+1)/2) \end{pmatrix}. \qquad (4.4)$$

This equation defines the operators $\mathbf{T}_n$ and $\mathbf{t}_n$ in Equation (3.2).

The Characteristic Focus

The CSA2D was simulated with $N_r = 20$, $N_c = 20$, $R = 120$ mm, $w = h = 6$ mm, and $2\phi_o = 60^o$ at $f = 500$ kHz with $\rho, c, and\ \alpha$ as in Section 4.3.1. The array was focused at its geometric center to generate its characteristic focus. The intensity profiles of the characteristic focus of the CSA2D are shown in Figure 4.6. The dimensions of this focus are $\Delta w = 4$ mm, $\Delta \ell = 24$ mm, and $\Delta z = 5$ mm. The intensity gain at the focus is 21.2 dB.

Steered-Focus Patterns

The CSA2D was focused at a point P_1, at depth 120 mm, transverse distance 21 mm, and elevation 0. The intensity profiles corresponding to this case are shown in Figure 4.7. The presence of the grating lobe can be seen clearly with a relative intensity level of -8 dB below the main focus.

The CSA2D was then focused at a point P_2, at depth 120 mm, transverse distance 0, and elevation 21 mm. Figure 4.8 shows the intensity profiles due to the focus at P_2. The relative intensity of the grating lobe associated with this focus is - 3.9 dB. Obviously, the performance of the CSA2D as a scanning applicator depends on the lateral dimension in which scanning is performed, i.e., transverse or elevation. The grating lobe level associated with the focus at P_1 can be tolerated in most scanning

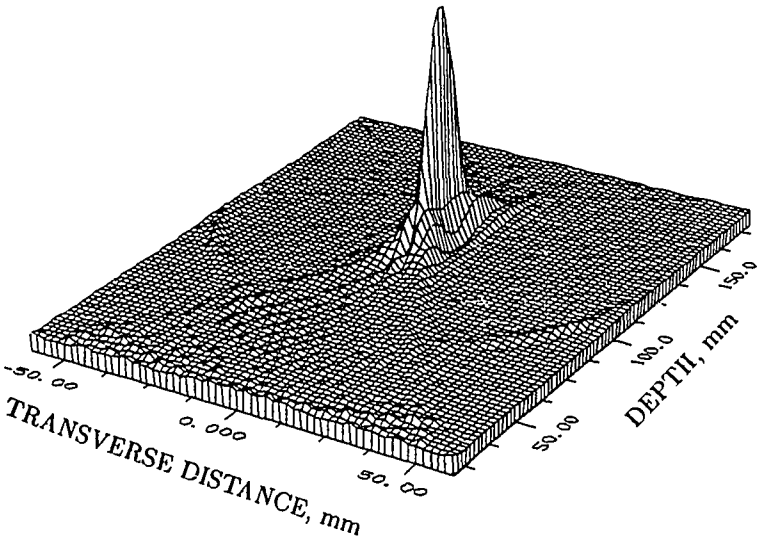

a) $z = 0$ plane.

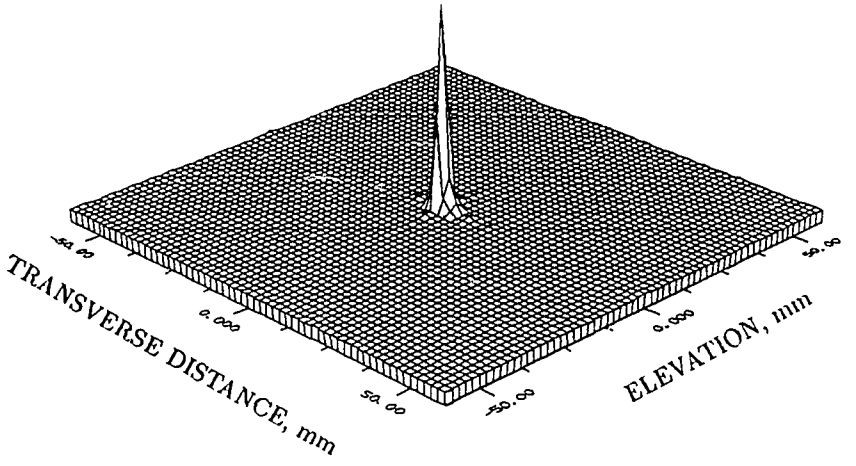

(b) Focal plane.

Figure 4.6. Intensity profiles of the characteristic focus of the CSA2D.

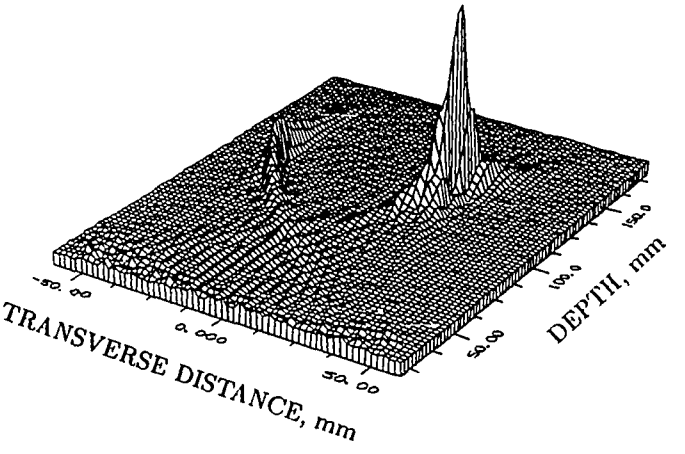

a) $z = 0$ plane.

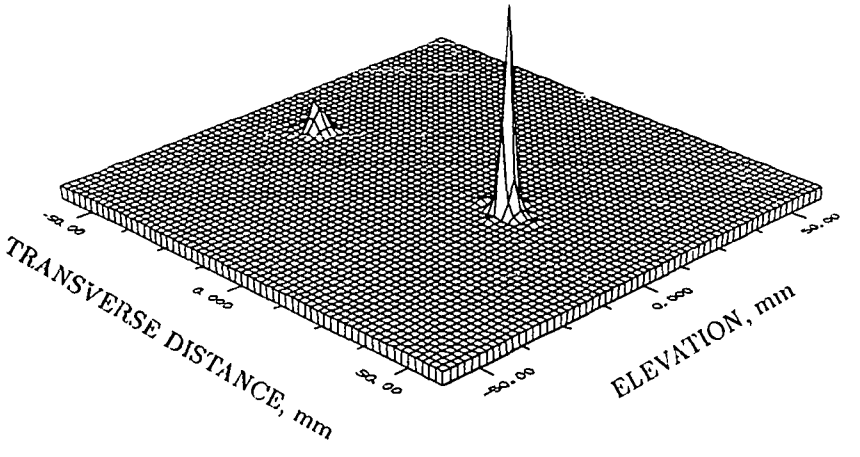

b) Focal plane.

Figure 4.7. Intensity profiles of a transversally shifted focus with the CSA2D.

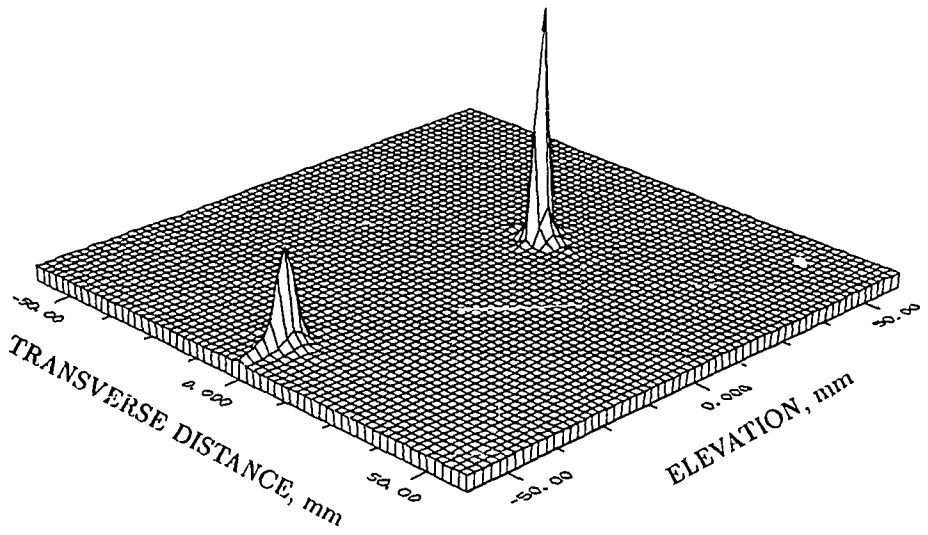

Figure 4.8. Intensity profile in the focal plane of a laterally shifted focus by the CSA2D.

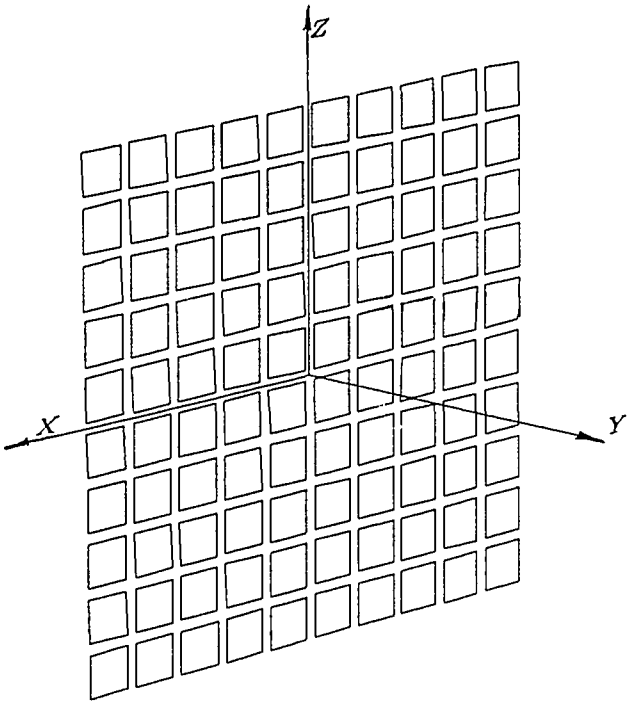

Figure 4.9: Isometric view of the $N \times N$ square array.

situations. The same does not hold true in the case of focusing at P_2. Therefore, to make the best use of the CSA2D, scanning in the elevation direction should be avoided. One alternative is to focus the CSA2D at a set of points distributed on a vertical line and scanning this shaped focus in the transverse and depth directions. This approach is illustrated in Chapter 8.

Comparison with the $N \times N$ Array

To demonstrate the effect of the cylindrical geometry on the performance of the CSA2D, a square $N \times N$ array, Figure 4.9, was simulated under similar conditions as those described for the CSA2D. The dimensions of the $N \times N$ array were chosen such that it has the same surface area, the same number of elements, and the same

center-to-center spacing as the CSA2D. In other words, $N_r = 20$, *and* $w = h = 6$ mm and the width of the array aperture was equal to the arc length of the CSA2D. The $N \times N$ array was focused at a point Q_1 at depth 120 mm, transverse distance 0, and elevation 0. The resulting intensity profiles are shown in Figure 4.10. The dimensions of the focal spot are $\Delta w = 5$ mm, $\Delta \ell = 35$ mm, and $\Delta z = 5$ mm. The intensity gain at the focus is 18.2 dB. One can see clearly two grating lobes forming to either side of the main beam in the transverse direction. No such grating lobes form in the elevation direction. The reason for this behavior is that the center-to-center spacing in the transverse direction corresponds to that of the CSA2D and is larger than the center-to-center spacing in the elevation direction.

The $N \times N$ array was then focused at a point Q_2 at depth 120 mm, transverse distance 20 mm, and elevation 0. The resulting intensity profiles are shown in Figure 4.11. The relative intensity of the grating lobe associated with this focus is -5.6 dB.

A comparison of the foci produced by the $N \times N$ at Q_1 and Q_2 with those produced by the CSA2D at P_1 and P_2 demonstrates the relative performance of these two array structures. One can clearly see that the CSA2D provides higher intensity gain at the focus and a smaller grating-lobe intensity level than its equivalent $N \times N$ array.

3.3.3 The spherical-section array

The CSA2D was shown to be capable of 3D scanning of focused beams. Furthermore, as will be shown in Chapter 6, it can also be simultaneously focused at a set of points with 3D distribution in the treatment volume. However, scanning in the elevation direction with the CSA2D can be limited by intensity gain loss and/or excessive grating lobe levels. This is to be expected since the CSA2D behaves as a planar array in the elevation direction.

The limitations of the CSA2D can be eliminated by mounting the array elements on a spherical shell rather than a cylindrical shell. This results in the spherical-

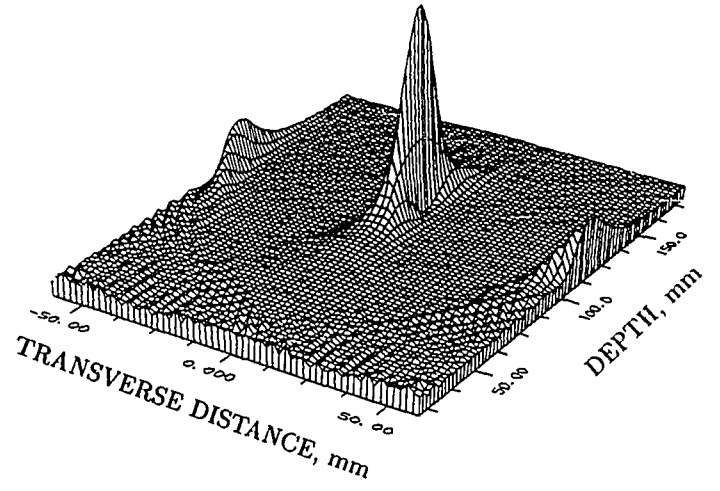

a) $z = 0$ plane.

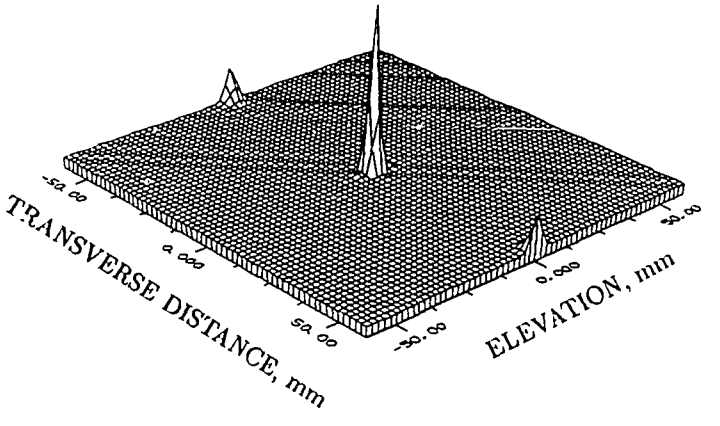

b) Focal plane.

Figure 4.10. Intensity profiles produced by the $N \times N$ array when focused at a point 120 mm deep along its central axis.

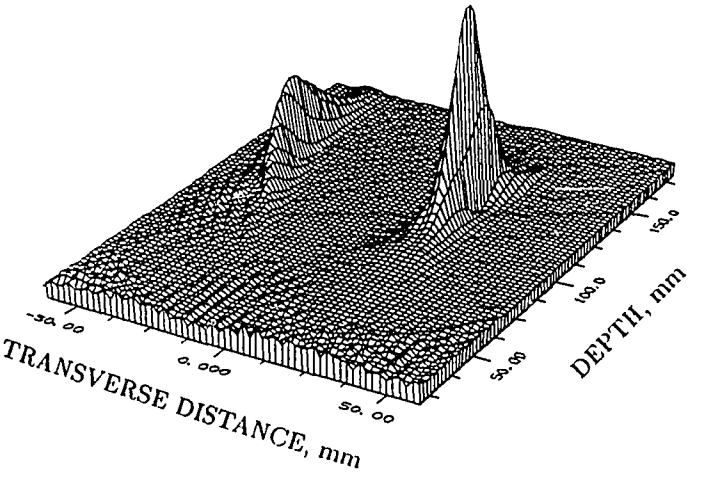

Figure 4.11. Intensity profile in the $z = 0$ plane of a shifted focus produced by the $N \times N$ array. Focal point at a depth of 120 mm and a transverse distance of 20 mm.

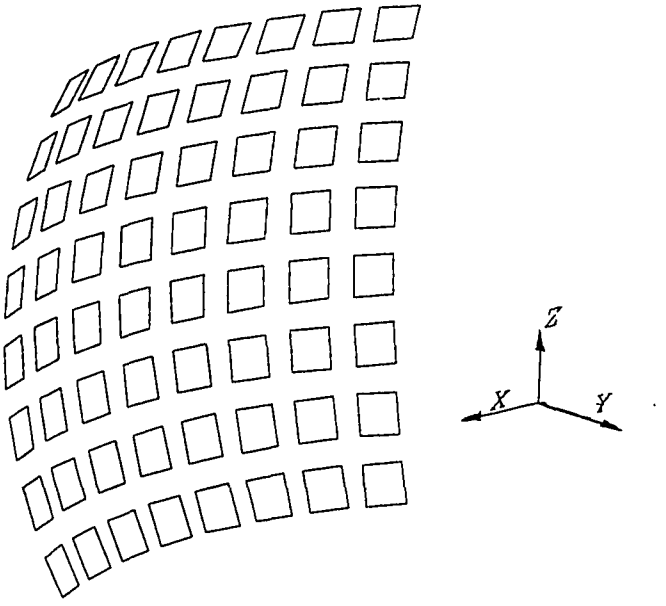

Figure 4.12. Isometric view of the spherical-section array, SSA.

section array, SSA, which is shown in Figure 4.12. This array will be shown to have higher intensity gain at the focus and improved scanning capabilities in the elevation direction when compared to the CSA2D.

Array Geometry

The array consists of $N_r \times N_r$ square elements of width (w) distributed uniformly on a spherical section of radius (R) and angular opening ($2\phi_o$) both transversely and laterally. The nth element of the array (located at row n_r and column n_c) makes an angle ϕ_{n_r} with the (x, y) plane. Its projection on the (x, y) plane makes an angle θ_{n_c} with the x axis. An observation point $\mathbf{r} = [x, y, z]^t$ can be transformed to the

coordinate system centered at the nth element according to

$$\mathbf{r}_n = \begin{pmatrix} \cos(\theta_{n_c}) & -\sin(\theta_{n_c}) & 0 \\ -\sin(\theta_{n_c})\cos(\phi_{n_r}) & -\cos(\theta_{n_c})\sin(\phi_{n_r}) & -\sin(\phi_{n_c}) \\ -\cos(\theta_{n_c})\cos(\phi_{n_r}) & -\cos(\theta_{n_c})\sin(\phi_{n_r}) & -\cos(\phi_{n_c}) \end{pmatrix} \cdot \mathbf{r} + \begin{pmatrix} 0 \\ r_c \\ 0 \end{pmatrix}. \quad (4.5)$$

This equation defines the operators $\mathbf{T}_n$ and $\mathbf{t}_n$ in Equation (3.2).

The Characteristic Focus

The SSA was simulated with $N_r = 16$, $R = 120$ mm, $w = 6$ mm, and $2\phi_o = 60^o$ at $f = 500$ kHz. The intensity profiles of the characteristic focus of the SSA are shown in Figure 4.13. The dimensions of this focus are $\Delta w = 3$ mm, $\Delta \ell = 20$ mm, and $\Delta z = 3$ mm. The intensity gain at the focus is 23.8 dB.

Steered-Focus Pattern

The SSA was focused at a point P at depth 120 mm, transverse distance 20 mm, and elevation of 0. The resulting intensity profiles are shown in Figure 4.14. The intensity gain at the focal point is 22.1 dB. A grating lobe with intensity level of -8 dB below the focal intensity appears at $x = -25$ mm and $z = 0$ mm in the focal plane. The dimensions of the shifted focal beam are essentially unchanged from those of the characteristic focus.

4.4 Concluding Remarks

The simulation results shown in this chapter outline some of the advantages of nonplanar phased arrays as potential hyperthermia applicators. The results from the CSA2D and the $N \times N$ array (Section 4.3.2) show clearly that the CSA2D is capable of providing higher focal intensity gain (the two arrays have the same number of elements and surface area.) Furthermore, the grating-lobe intensity level associated with a shifted focus was lower in the case of the CSA2D.

These conclusions hold true for the SSA which provides additional intensity gain and grating-lobe reduction for shifted beams. This was true for the SSA simulated herein in spite of the fact that it has a smaller number of elements covering roughly

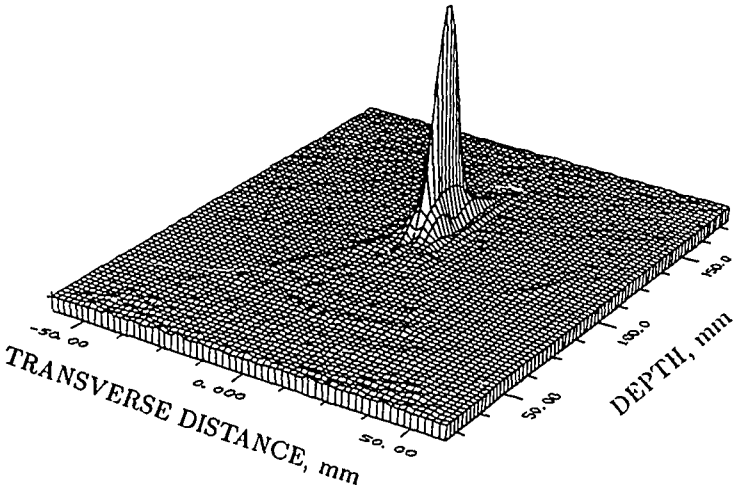

a) $z = 0$ plane.

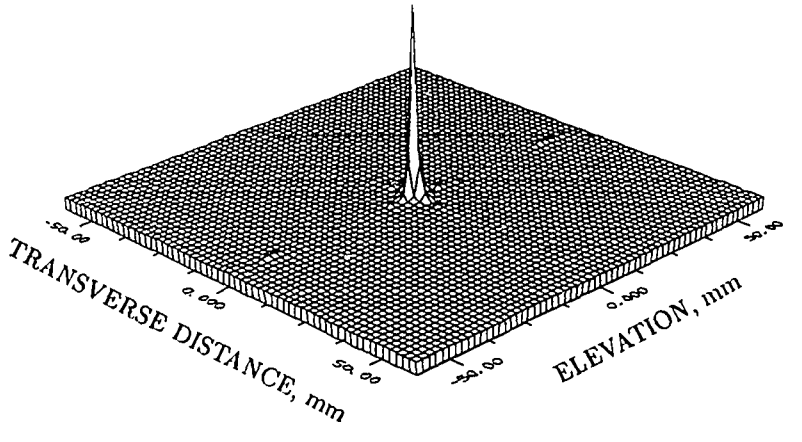

b) Focal plane.

Figure 4.13. Intensity profiles of the characteristic focus of the SSA.

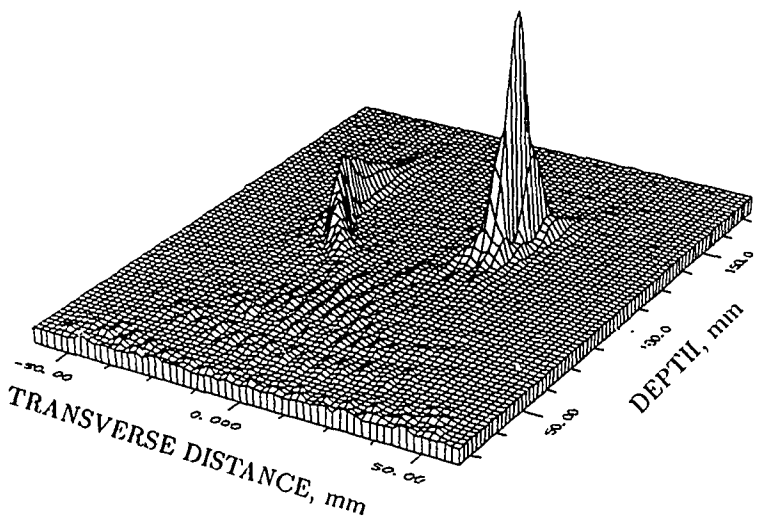

Figure 4.14. Intensity profile in the $z = 0$ plane of a shifted focus produced by the SSA. Focal point is 120 mm deep and 20 mm off-axis.

the same surface area as the CSA2D and the $N \times N$ arrays simulated earlier. This observation demonstrates another advantage of the nonplanar phased arrays; the use of nonplanar phased arrays allows the design of arrays with a large surface area (to provide the necessary intensity gain) with a smaller number of elements than what would be necessary when using planar phased arrays for the same purpose. This conclusion is also supported by the performance of the CSA2D when used to scan in the transverse and elevation direction. The grating-lobe intensity level was smaller when the array was scanned in the transverse direction (where the nonplanar geometry determines the grating-lobe intensity level).

The higher intensity gain achieved by nonplanar (geometrically-focused) arrays is due to the fact that the element directivity pattern is maximum near the geometric center of the array for all its elements. This is also mainly responsible for the reduction in the grating lobe level associated with shifted foci. The location of the grating lobe, however, is a function of the array lattice only and is independent of the element directivity pattern. Generally, approximate formulae for the determination of the location and relative intensity of the grating lobes for cylindrical arrays exist [57].

CHAPTER 5

HEATING PATTERN GENERATION WITH PHASED ARRAYS

5.1 General

The previous chapter described several array geometries potentially useful as hyperthermia applicators. However, irrespective of their geometry, phased arrays used as hyperthermia applicators usually have a large surface area to provide sufficient intensity gain to insure efficient heating. When near-field focusing is attempted with such array structures, a focal spot is generated within a small volume defined by an ellipsoid extending on the order of one wavelength laterally and a few wavelengths longitudinally. At frequencies suitable for hyperthermia, the size of this focal spot is too small to induce uniform heating even in small tumors. Hence, it is necessary to spread out the power deposition throughout the tumor volume in order to produce the desired heating pattern. A suitable power deposition pattern is one which allows inducing and maintaining uniform therapeutic temperature levels throughout the tumor volume for specified time durations while maintaining the temperature in normal tissues surrounding the tumor below a specified maximum acceptable temperature level. Power deposition can be spread out by dynamic scanning of the focal spot along a specified trajectory. Scanning can also be used with multiple-focus and diffuse-focus field patterns. Another alternative is the direct synthesis of the heat-

ing pattern. Methods for generating single-focus, diffuse-focus, multiple-focus, and shaped beam patterns are discussed in Chapter 6. Specifically, all the results shown in this chapter are obtained using the pseudoinverse method which is described in full detail in Chapter 6. The details entailed in how each of these patterns is generated are also given in Chapter 6. In this chapter, however, these patterns are presented as typical examples of single-focus, multiple-focus, diffuse-focus, and directly synthesized fields defined below. The rest of this chapter discusses the generation of heating patterns based on these four different approaches and outlines the merits and limitations of each of them.

5.2 Single-Focus Scanning

Depending on the tumor geometry and the existence or nonexistence of a necrotic core or special directivity of blood flow in the treatment volume, different scanning procedures can be used [4, 7, 9]. However, irrespective of the scanning procedure, it is necessary to insure therapeutic localized heating in the tumor volume. For example, when heating necrotic tumors, it was found that scanning around the periphery of the tumor can be advantageous in inducing uniform heating, i.e., uniform temperature profiles within the tumor [4, 52].

Electronic scanning is achieved by sequentially focusing at one of a series of fixed points distributed along the scan trajectory such that the spatio-temporal average of the scalar sum of the power deposition patterns of the individual focal points produces the desired time-average power deposition pattern throughout the treatment volume. A single focal spot can be generated by instantaneously changing the phases of the driving signals only, i.e., uniform amplitude distributions are used. The intensity gain at the focal spot varies as the focal point is moved in the treatment volume. Losses in intensity gain can be compensated for by either varying the amplitude level of the driving signals or changing the dwell time at each of the focal points. To illustrate this, assume that their exist N_f focal points along the scan path that are

periodically scanned with a scan period smaller than the thermal time constants of the tissues in the treatment region. If equal dwell times are used at each focal point and loss in intensity gain is compensated for by weighting of the amplitude of the driving signals, the time-average power deposition in the treatment volume is given by

$$Q_{av}(\mathbf{r}) = \frac{1}{N_f} \sum_{l=1}^{N_f} Q_l(\mathbf{r}) w_l, \tag{5.1}$$

where $Q_l(\mathbf{r})$ is the power deposition pattern associated with the lth focal point, and w_l is a weighting factor accounting for intensity modulation. On the other hand, if the amplitude level is held constant for all focal points and the dwell time is varied to compensate for loss in intensity gain, the time-average power deposition of the scanned field is given by

$$Q_{av}(\mathbf{r}) = \frac{1}{T_s} \sum_{l=1}^{N_f} Q_l(\mathbf{r}) \Delta T_l, \tag{5.2}$$

where T_s is the scan period, and ΔT_l is the dwell time at the lth focal point. The power deposition is the source of heat generation in the treatment volume. The power deposition due to a field pattern associated with the lth focal point [18]

$$Q_l(\mathbf{r}) = \alpha \frac{p(\mathbf{r}) p^*(\mathbf{r})}{\rho c}, \tag{5.3}$$

where α is the absorption coefficient, $p(\mathbf{r})$ is the complex pressure, and ρ and c are the speed of sound and the density of the medium, respectively. The volumetric heat generation in the tissue is given by either Equation (5.1) or Equation (5.2) and represents the driving source to the *bioheat transfer equation, BHTE*,

$$\nabla.(K \nabla T) - W_b C_b (T - T_a) + Q = \rho C \frac{\partial T}{\partial t}, \tag{5.4}$$

where T is the tissue temperature, K is the intrinsic thermal conductivity of tissue, W_b is the blood perfusion rate, C_b is the specific heat of the blood, and T_a is the arterial blood temperature. The $BHTE$ models the thermal response of the tissues in the treatment volume to the heating stimulus, Q [19].

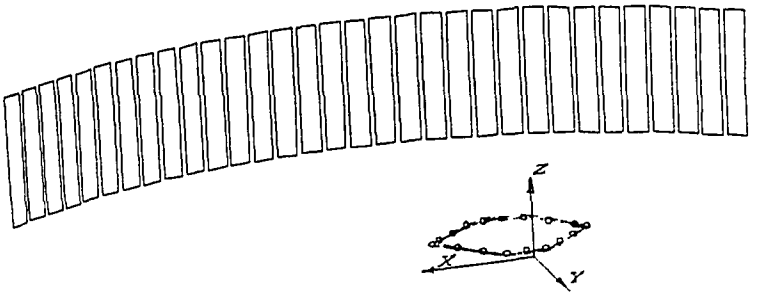

Figure 5.1. A typical scan trajectory with the CSA1D.

Electronic scanning of beams to produce time-average heating patterns entails instantaneous switching of driving signal distributions to move the focus from one point to another along the scan path. This implies that individual focal points along the scan path are distributed at a finite number of discrete locations. The distribution of the focal points along the scan trajectory is decided based on the half-power dimensions of the focal spots. Therefore, it is necessary to estimate how these dimensions change as the beam is moved along the scan trajectory. The neighboring focal spots along the scan trajectory should have a sufficient degree of overlap to insure uniform power deposition levels. A typical scan trajectory is shown in Figure 5.1 with the CSA1D. The scan trajectory follows a hexagonal ring which is fitted inside the periphery of an assumed tumor centered at the center of the tumor. The scan trajectory in this case is chosen to heat both the front and the back of the tumor. Figure 5.2 shows the scanned-field power deposition pattern produced by the

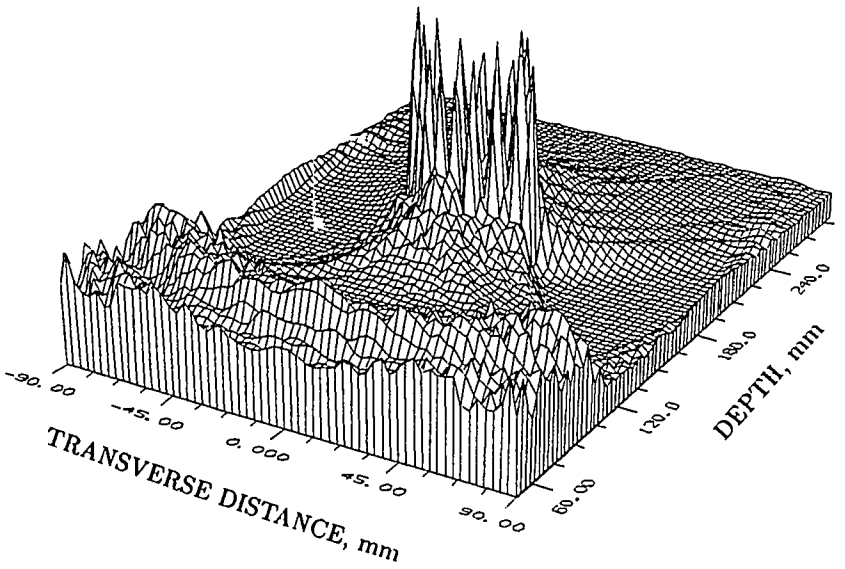

Figure 5.2. Scanned-field power deposition pattern produced by single- spot scanning around the scan trajectory of Figure 5.1 using the CSA1D.

CSA1D when used to scan the trajectory shown in Figure 5.1. The scanned field profile shown in this example appears to be "rough." However, as will be shown in Chapter 8, the temperature profiles resulting from this pattern are smooth and uniform. This is due to the lowpass filter effect of the bioheat equation. To see this, consider the steady-state homogeneous $BHTE$,

$$K\nabla^2 T - W_b C_b T + Q = 0, \tag{5.5}$$

where, for convenience, T now represents the difference between the actual temperature and the arterial blood temperature. This equation can be transformed to the spatial frequency domain by using the Fourier transform which yields

$$-K\omega_s^2 \tilde{T} + W_b C_b \tilde{T} - \tilde{Q} = 0, \tag{5.6}$$

where $\omega_s = \sqrt{\omega_x^2 + \omega_y^2 + \omega_z^2}$ is the spatial frequency, and $\tilde{T}$ and $\tilde{Q}$ are the Fourier

transforms of T and Q, respectively. The temperature can now be expressed as a function of power deposition in the frequency domain as follows

$$\tilde{T} = \frac{1}{K} \frac{\tilde{Q}}{\omega_s^2 + \frac{W_b C_b}{K}}. \tag{5.7}$$

Therefore, the transfer function, $\tilde{G} = \frac{\tilde{T}}{\tilde{Q}}$, can be given by

$$G(\omega_s) = \frac{1}{K} \frac{1}{\omega_s^2 + \frac{W_b C_b}{K}}, \tag{5.8}$$

which represents a second-order lowpass filter with a cutoff spatial frequency of

$$\omega_{s_c} = \pm j \sqrt{\frac{W_b C_b}{K}}. \tag{5.9}$$

Therefore, the irregularities in the power deposition patterns (which correspond to higher frequency components) will be smoothed out in the resulting temperature profiles.

Scanning of single-focus patterns to generate a desired heating pattern is advantageous mainly in the following respects:

1. It utilizes uniform amplitude driving signals hence simplifying the driving electronic circuitry and allowing the most efficient use of the array elements.

2. The small focal spot is ideal for heat localization.

3. Any power-deposition build-up outside the target volume can be easily predicted.

The first two advantages stated here are self-explanatory. The third advantage, however, can be explained by the following.

The most significant power-deposition build-up outside the scanned volume is caused by the overlapping transmission volumes of individual beams due to the large cross section of the beams near the array surface. This power-deposition build-up is usually smooth with relative power deposition level well below that in the target volume. Figure 5.2 shows a "banana-shaped" power deposition pattern near the surface

of the array. Simulated thermal response to this heating pattern given in Chapter 8 indicates that such a power-deposition build-up can be tolerated. Furthermore, improvement on such heating pattern can be achieved by using an array with higher intensity gain, e.g., the SSA. This is illustrated by an example in Chapter 8.

The main disadvantage of single-focus scanning is the possible need for high focal intensities which might be objectionable because of nonthermal damaging effects. A focal intensity may be objectionable if it is higher than the cavitation threshold or if intensity saturation due to nonlinear effects can occur. Collapse cavitation can cause hemorrhage [4] and extreme pain, and intensity saturation can cause most of the power deposition to occur in the intervening tissues prior to the tumor site, consequently causing hot spots to occur or failure of the treatment altogether [10, 11]. It is important to emphasize, however, that cavitation has not been reported as a serious problem in clinical treatments with focused ultrasonic applicator systems. Therefore, with the current lack of precise cavitation thresholds in tissues in vivo at frequencies below 1 MHz, safety requires that focal intensity levels in excess of 100 W/cm^2 should be avoided [41, 46].

5.3 Multiple-Focus Scanning

Multiple-focus scanning can be used in a similar way as outlined for a single-focus scanning. The main difference is that the "snapshot" at one time instant of field patterns has more than one focal spot. This approach has the advantage of producing the desired time-average power deposition levels while avoiding the use of extremely high focal intensities. This scanning approach can be very useful in situations where a major blood vessel passes through the tumor. In such situations, it has been suggested [3] that the incoming blood should be warmed before entering the tumor so that the difference between the tumor temperature and the blood temperature is reduced which, consequently, reduces the heat carried away by blood flow. To achieve this, one can use a double-focus scanning scheme in which one

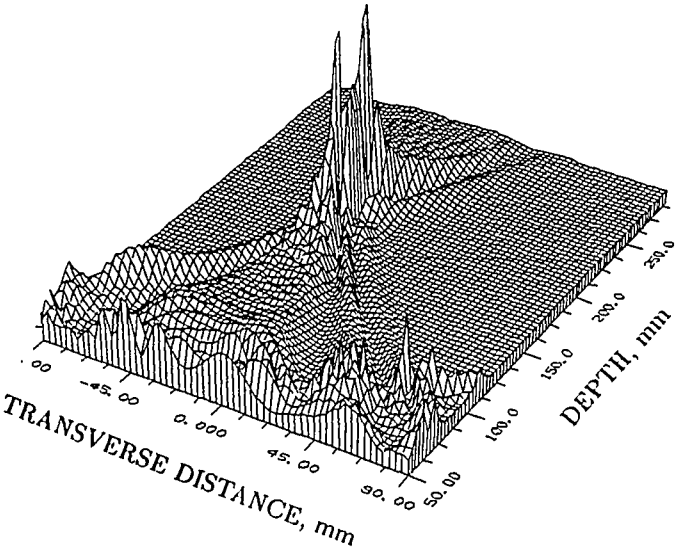

Figure 5.3: Intensity profile of a double-focus field pattern produced by the CSA1D.

focus is scanned around the tumor and the other, at a relatively lower intensity level, is scanned along the blood vessel to warm the incoming blood. Figure 5.3 shows a double-focus field pattern produced by the CSA1D. This field pattern can be used, for example, for scanning the trajectory shown in Figure 5.1. This approach is illustrated further in Chapter 8.

The disadvantage of the multiple-focus approach is that the interference patterns formed when the array is focused at several points simultaneously are usually complex and their final contribution to the heating pattern is not easily predicted. However, when a small number of focal points is used, successful generation of desired heating patterns can be achieved without significant hot spots outside the tumor volume. Another disadvantage of this approach is that the driving signals for the array elements often vary in both amplitude and phase. Amplitude variation could result in low array excitation efficiency which might not be acceptable under certain condi-

tions. However, a method for improving the array excitation efficiency can be used successfully with most multiple-focus field patterns makes the latter disadvantage less significant. The method uses an iterative weighting algorithm which achieves improved array excitation efficiency by suppressing the dynamic range of the amplitude distribution to the array elements. This method is described in Chapter 7.

5.4 Diffuse-Focus Scanning

An excitation vector can be found to generate more diffuse focal patterns which behave like a single beam with the energy spread out in one or two dimensions. This increases the volume of the focal spot and allows for a small number of focal points along the scan trajectory at reduced focal intensity levels. This approach is advantageous in the generation of heating patterns with reduced focal intensity levels. In addition, the power deposition build-up due to scanning can be easily predicted from the shape of the focal beam. The disadvantages of this approach are nonuniform amplitude distributions and poor localization of heating when beams with very large cross sections are used. Figure 5.4 shows a diffuse focus produced by the CSA2D in which the focal spot is extended in the elevation direction while basically maintaining its original shape transversely and longitudinally (compare to the intensity profiles in Figure 4.6). The beam profile in the elevation direction for this focus was synthesized (using the pseudoinverse method, Chapter 6) to follow the formula

$$Q(z) = Q_o \frac{1 + (\frac{z}{rt})^2}{1 + (\frac{z}{rt})^4}. \tag{5.10}$$

This type of focus can be scanned transversely to induce the desired power deposition pattern in the treatment volume.

5.5 Direct Synthesis of Heating Patterns

Heating patterns can be directly synthesized, in principle, by focusing a phased array simultaneously at a set of points conforming to a specified tumor geometry.

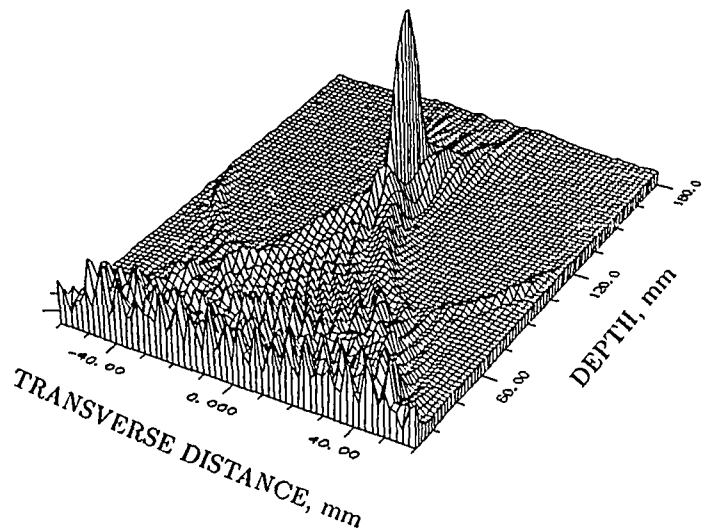

a) $z = 0$ plane.

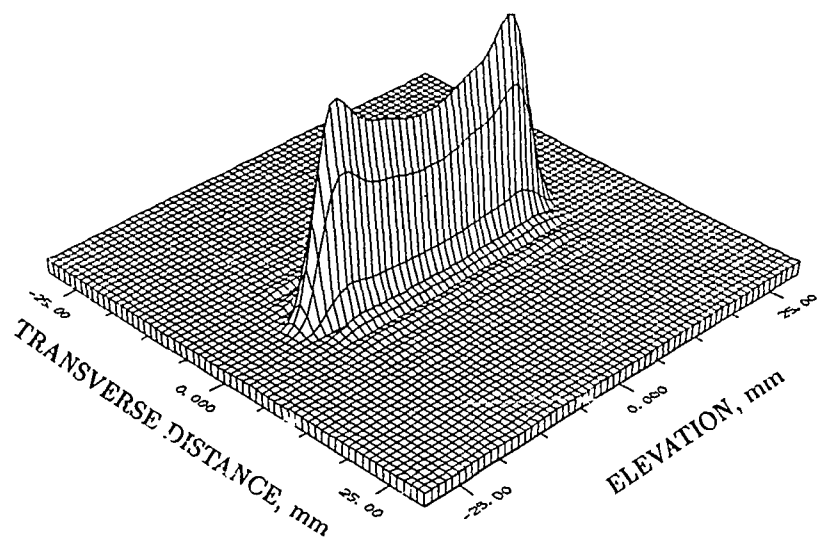

b) Focal plane.

Figure 5.4. Intensity profiles of a diffuse-focus field pattern produced by the CSA2D.

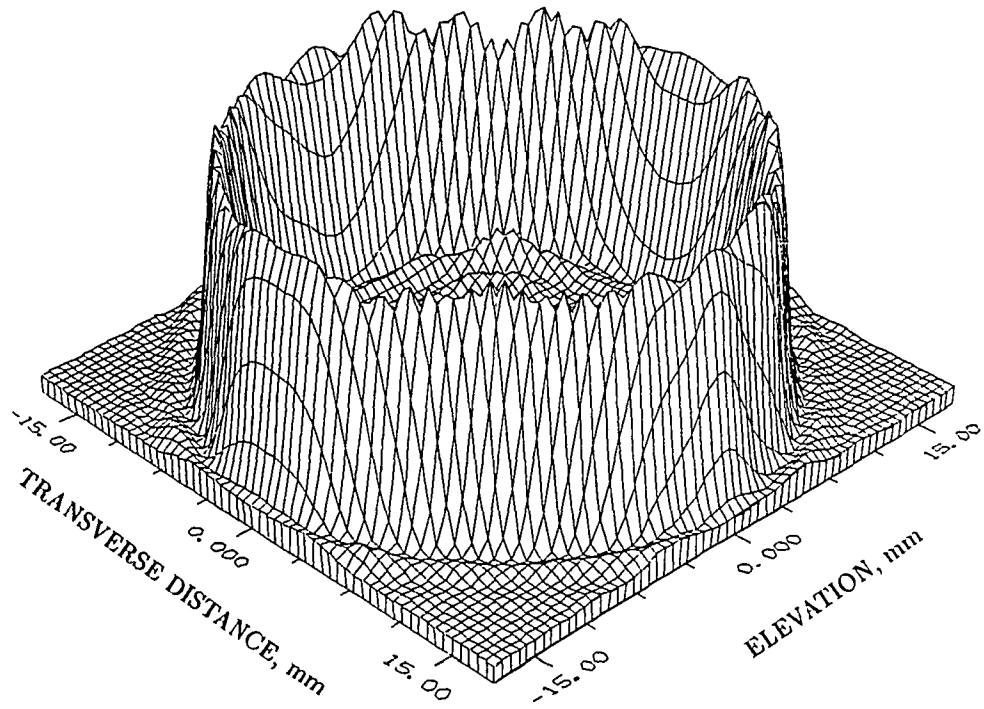

Figure 5.5. Intensity profile in the focal plane of an annular-ring field pattern produced by the SSA.

The distribution of these focal points can, for example, be identical to the distribution of the focal points along a prescribed scan path in single-focus scanning. When direct synthesis is performed with arbitrary distribution of the focal points, the potential interference patterns are often unavoidable and very hard to predict in advance. However, some geometrical patterns are possible where potential interference patterns can be anticipated and techniques to reduce them are developed. An example of these patterns is one in which an annular ring is synthesized which could be useful in heating the periphery of spherical or cylindrical tumors. Figure 5.5 shows the intensity profiles of an annular ring pattern produced by the SSA.

As in the multiple-focus pattern generation, the driving signal distribution varies in amplitude and phase which could mean low array excitation efficiency. While this can provide an alternative to single-focus scanning when cavitation and intensity saturation are anticipated, it has no significant advantage over the multiple-focus

scanning approach (except, possibly, in cases where scanning can be avoided completely using this technique).

CHAPTER 6

THE PSEUDOINVERSE PATTERN SYNTHESIS METHOD

6.1 General

The previous chapter illustrated the different methods with which a desired heating pattern can be generated using a phased array. Multiple-focus field patterns not only allow one to prevent the use of extremely high focal intensity levels, but also to tailor the heating pattern to a particular tumor environment. This, in addition to the fast switching capability of driving-signal distributions, makes phased arrays the most flexible and adaptive applicator systems.

This chapter describes methods for evaluating phased-array excitation vectors capable of producing desired multiple-focus field patterns. The problem of phased-array pattern synthesis is defined followed by a brief discussion of the previous phased-array pattern synthesis methods used in hyperthermia. Then the pseudoinverse pattern synthesis method is introduced and discussed in detail including some useful special cases. The chapter is concluded by a set of numerical examples to illustrate the capabilities of the pseudoinverse pattern synthesis method. The examples also demonstrate how does the pseudoinverse method compare with previously used methods. The term "Multiple-Focus Field Patterns" as used in this and the subsequent chapters is equally applicable to "Diffuse-Focus" and "Directly-Synthesized" field

patterns.

6.2 Phased-Array Pattern Synthesis

The problem of phased array pattern synthesis aims at finding answers to the basic question: given a *desired* field pattern, F_d, and some *constraints*, e.g., the array size, number of elements, and the propagation medium, what is the driving-signal distribution, $\mathbf{u}$, at the surface of the array which is capable of realizing F_d. Of course, F_d can rarely be realized exactly. Hence, it is necessary to define what would be an acceptable approximation for F_d, i.e., an approximation criterion must be defined. Furthermore, in the most general case, F_d is a function of azimuth, elevation, and range. This is certainly the case for the near-field pattern synthesis utilized for hyperthermia. Specifying F_d everywhere in the field of the array would result in a huge problem that cannot be easily solved even on a supercomputer. Furthermore, overspecifying the field pattern almost certainly would result in violating the set of constraints which might result in large errors in the synthesized pattern. Therefore, it is desired to specify the field pattern at a minimum number of points which allows the realization of F_d with the closest possible fit.

This definition of the phased-array pattern synthesis problem is similar to several problems in physics and engineering, e.g., antenna pattern synthesis [59], design of frequency selective finite impulse response filters, FIR [60], etc. This problem belongs to a general problem referred to in the literature as *beamforming* [61], a term derived from the fact that early spatial filters were designed to form pencil beams. This term applies for both radiation and reception of energy. In this thesis, however, the array is used to radiate energy for power deposition in the target volume.

6.3 Previous Work

Two methods were previously proposed to generate multiple-focus field patterns with phased arrays for localized hyperthermia [12, 13]. As will be seen later in this

section these two methods were not posed in terms of the definition given in Section 6.2. Both of these methods attempt to maximize the power deposition level at a set of focal points without specifying an error criterion with which the realized field approximates the desired pattern. In other words, they do not guarantee the degree of fit between the desired and realized field patterns. However, both of these methods were successfully used to generate multiple-focus field patterns. A brief discussion of these two methods is given in this section.

The discussion in this section is confined to time-harmonic analysis with $e^{j\omega t}$ time convention in homogeneous, possibly attenuating, media. Under the time-harmonic assumption, it suffices to describe the driving signal to an array element by $Ae^{j\phi}$, where A and ϕ are real numbers representing the amplitude and phase, respectively. The speed of sound, density, and attenuation coefficient of the medium are typical of those in tissues and will be explicitly given when needed.

6.3.1 Conformal focusing

Ocheletree [12] discussed the simplified problem of M omnidirectional sources focused at N points in a lossless medium. Conformal focusing is performed by focusing the M sources at N points simultaneously. This is achieved by choosing the driving phase of the mth source, θ_{opt}, such that the contribution of the source is maximized at each focal point. The quantity

$$\gamma = \sum_{n=1}^{N} A_n \cos(\theta - \theta_n), \tag{6.1}$$

is the sum of the in-phase components of the mth source at the focal points in which A_n is the desired amplitude at the nth focal point, and θ_n is the phase on the mth source necessary for it to add in phase to the field at the nth focal point, $\theta_n = kd_n$ where k is the wavenumber and d_n is the distance between the source and the nth focal point. The optimal phase θ_{opt} satisfies

$$\frac{\partial \gamma}{\partial \theta} = -\sum_{n=1}^{N} A_n \sin(\theta_{opt} - \theta_n) = 0, \tag{6.2}$$

subject to $\frac{\partial^2 \gamma}{\partial \theta^2} < 0$. After simple algebra, one can show that

$$\theta_{opt} = tan^{-1} \frac{\sum_{n=1}^{N} A_n \sin(\theta_n)}{\sum_{n=1}^{N} A_n \cos(\theta_n)}, \tag{6.3}$$

and the driving signal on the mth source is

$$s_m = \sum_{n=1}^{N} A_n e^{jkd_n}, \tag{6.4}$$

which is simply the sum of the complex signals required to focus the source at each of the focal points alone. As is clearly seen from the above derivation, this method attempts to maximize the contribution of the mth source to the signal at the nth focal point. It does not say anything about the degree of fit between the realized and desired field profiles.

6.3.2 The field conjugation method

This method replaces the desired focal points by small fictitious sources (continuous sources are possible). The total field due to all of these fictitious sources is computed at the surface of each array element. The driving signal for that element is the conjugate of the computed field due to the imaginary sources. For the case of M omnidirectional sources focused at N focal points in a lossless medium, it is easy to show that the driving signal to the mth array element is given by

$$s_m = \sum_{n=1}^{N} A_n \frac{e^{jkd_n}}{d_n}, \tag{6.5}$$

where A_n and d_n are as defined above. One can see that the only difference between the field conjugation method and the conformal focusing method is that the latter ignores the $\frac{1}{r}$ term in the Green's function which is utilized in the field conjugation method. As applied in [13], the field conjugation method does not provide precise control over the field level at each of the fictitious sources.

6.4 The Pseudoinverse Method

The above two synthesis methods produce field patterns that approximate the desired field patterns even at the defined focal points. This approximation depends

on the specific choice of the focal points with respect to the array and is not governed by any error criterion. The pseudoinverse method introduced herein allows one to specify the complex field value at a set of points, henceforth called *control points.* If the number of control points is less than or equal to the number of elements of the array, then the reconstructed field satisfies the specified field levels at all of the control points. The field can assume any value at the unspecified points. However, simulation results performed for this thesis and elsewhere [55] show that the energy tends to fall off around the control points as determined by the point-spread function of the array used, i.e., energy concentration or focusing at the control points is achieved. Of course, this does not prevent one from choosing the field level at a control point such that the power deposition level is forced to take a relatively small value to avoid potential hot spots.

6.4.1 Notation

The following discussion assumes finite dimensional complex-valued signals. The excitation vectors (particle velocity distribution) of an N-element array $\mathbf{u} \in C^N$ where C^N is the set of N-tuples of complex numbers. The field is sampled at a set of M control points in the observation space of the array. The complex pressure at these points is given by $\mathbf{p} \in C^M$ where C^M is the set of M-tuples of complex numbers which define the control-point space. The underlying observation space is a Hilbert space of square summable bandlimited signals. The Euclidian (L_2) inner product on the control-point space is defined by

$$< \mathbf{x}, \mathbf{y} >_{C^M} = \sum_{m=1}^{M} x_m^* y_m \tag{6.6}$$

where the asterisk sign indicates conjugation. This defines the norm of control sequence $\mathbf{x}$ as $\| \mathbf{x} \|^2 \stackrel{\text{def}}{=} < \mathbf{x}, \mathbf{x} >_{C^M} = \sum_{m=1}^{M} | x_m |^2$ which is directly proportional to the sum of the power deposition at the control points. Similarly, the norm of an excitation vector $\mathbf{y}$ is $\| \mathbf{y} \|^2 \stackrel{\text{def}}{=} < \mathbf{y}, \mathbf{y} >_{C^N} = \sum_{n=1}^{N} | x_n |^2$ which is directly propor-

tional to the power available at the surface of the array. The notation developed in this subsection is important to the analysis of the pseudoinverse pattern synthesis method.

6.4.2 Theoretical formulation of the pseudoinverse method

The theory of the pseudoinverse method for multiple-focus pattern synthesis is as follows.

The complex acoustic pressure at a point in the field due to continuous source is given by the Rayleigh-Sommerfeld integral

$$\frac{j\rho ck}{2\pi}\int_{S'} u(\mathbf{r}')\frac{e^{-jk|\mathbf{r}-\mathbf{r}'|}}{|\mathbf{r}-\mathbf{r}'|}dS' = p(\mathbf{r}), \tag{6.7}$$

where $j = \sqrt{-1}$, ρ and c are, respectively, the density and the speed of sound in the medium, $k = \frac{\omega}{c}$ is the wavenumber, S' is the surface of the source, u is the particle velocity normal to the surface of the source, and $\mathbf{r}$ and $\mathbf{r}'$ are the observation and source points, respectively. For an array consisting of N elements having arbitrary geometry, Equation (6.7) can be written as

$$\frac{j\rho ck}{2\pi}\sum_{n=1}^{N} u_n \int_{S'_n}\frac{e^{-jk|\mathbf{r}-\mathbf{r}'_n|}}{|\mathbf{r}-\mathbf{r}'_n|}dS'_n = p(\mathbf{r}), \tag{6.8}$$

where S'_n and u_n are, respectively, the surface and the particle velocity of the nth element of the array, and $\mathbf{r}'_n$ represents points on the nth element of the array. If the complex pressure is known, or specified, at M control points, one can write

$$\frac{j\rho ck}{2\pi}\sum_{n=1}^{N} u_n \int_{S'_n}\frac{e^{-jk|\mathbf{r}_m-\mathbf{r}'_n|}}{|\mathbf{r}_m-\mathbf{r}'_n|}dS'_n = p(\mathbf{r}_m); \qquad m = 1, 2, ..., M. \tag{6.9}$$

This equation can be expressed in matrix form as

$$\mathbf{Hu} = \mathbf{p}, \tag{6.10}$$

where $\mathbf{u}$ is the complex excitation vector of the array elements $\mathbf{u} = [u_1, u_2, ..., u_N]^t$, and the vector $\mathbf{p}$ denotes the complex pressure at the control points in the field $\mathbf{p} =$

$[p(\mathbf{r}_1), p(\mathbf{r}_2), ..., p(\mathbf{r}_M)]^t$, and $\mathbf{H} : C^N \longrightarrow C^M$ is the forward propagation operator with elements

$$H(m,n) = \frac{j\rho ck}{2\pi} \int_{S'_n} \frac{e^{-jk|\mathbf{r}_m - \mathbf{r}'_n|}}{|\mathbf{r}_m - \mathbf{r}'_n|} dS'_n. \tag{6.11}$$

Using the notation introduced above, the pattern synthesis problem can be stated as follows: for a given control-point vector $\mathbf{p} \in C^M$, find the minimum-energy particle velocity vector $\mathbf{u} \in C^N$ which minimizes $\| \mathbf{Hu} - \mathbf{p} \|^2$.

The statement of the pattern synthesis problem calls for the so-called minimum-norm least-square approximation for the solution vector $\mathbf{u}$ denoted $\hat{\mathbf{u}}$. Several numerical methods have been proposed to solve this problem [75]. One solution can be obtained by solving the constrained optimization problem

$$\text{find } \hat{\mathbf{u}} \in C^N \text{minimizing } J(\mathbf{u}) = \| \mathbf{Hu} - \mathbf{p} \|^2 + \gamma \| \mathbf{u} \|^2 . \tag{6.12}$$

The parameter γ is referred to in the literature as the regularization parameter [56]. The name "regularization parameter" is due to the fact that, in certain problems, the matrix operator $\mathbf{H}$ is ill-conditioned. The minimizing vector can be found by setting $J(\mathbf{u} + \delta\mathbf{u}) - J(\mathbf{u})$ equal to 0. The resulting vector is given by

$$\hat{\mathbf{u}} = (\gamma \mathbf{I} + \mathbf{H}^{*t}\mathbf{H})^{-1}\mathbf{H}^{*t}\mathbf{p}, \tag{6.13}$$

where $\mathbf{I}$ is the identity matrix and $\mathbf{H}^{*t}$ is the conjugate transpose (adjoint) of $\mathbf{H}$. The matrix $\mathbf{H}^{*t}$ represents the backward propagation operator from the control-point space to the source space. The regularization parameter can be found using the method of Lagrange multipliers [54] and the problem is readily solved.

A more popular solution to the minimum-norm least-squares problem is provided by the Moore-Penrose Pseudoinverse $\mathbf{H}^\dagger$ [22] of the matrix $\mathbf{H}$ (also referred to as the generalized inverse). The pseudoinverse is obtained from the singular value decomposition, SVD, of $\mathbf{H}$ according to

$$\mathbf{H} = \mathbf{U}\Sigma\mathbf{V}^{*t} \tag{6.14}$$

and

$$\mathbf{H}^{\dagger} = \mathbf{V}\mathbf{\Sigma}^{-1}\mathbf{U}^{*t} \tag{6.15}$$

where $\mathbf{U}$ is an $m \times m$ orthogonal matrix, $\mathbf{V}$ is an $n \times n$ orthogonal matrix, and $\mathbf{\Sigma}$ is $diag\{\sigma_1, \sigma_2, \cdots, \sigma_{min(m,n)}\}$. The σ_i's determined by this method are unique and are called the singular values of $\mathbf{H}$. The singular values are usually ordered in descending order, i.e.,

$$\sigma_1 \geq \sigma_2 \geq \cdots \sigma_{min(m,n)} \geq 0. \tag{6.16}$$

The singular value decomposition provides valuable information about the operator $\mathbf{H}$ such as its rank (which is determined by the number of nonzero singular values), and its condition number $\frac{\sigma_1}{\sigma_{min(m,n)}}$. The condition number determines how "close" $\mathbf{H}$ is to being singular, which is very valuable in analyzing the stability of the solution against different sources of error.

Using the singular value decomposition, the minimum-norm least-square solution of Equation (6.10), $\hat{\mathbf{u}}$, is given by

$$\hat{\mathbf{u}} = \mathbf{H}^{\dagger}\mathbf{p}. \tag{6.17}$$

The solution given in Equation (6.17) can be rigorously shown to be the unique vector which minimizes $\| \mathbf{Hu} - \mathbf{p} \|^2$ which has the minimum norm $\| \mathbf{u} \|^2$ [15, 58]. This property of the solution vector picked up by the pseudoinverse is always satisfied, irrespective of the rank of $\mathbf{H}$. However, when the matrix $\mathbf{H}$ is full rank, the pseudoinverse takes the following special forms:

1. The minimum-norm solution

   When $M < N$, Equation (6.10) represents an underdetermined system of equations which has an infinite number of solutions. The pseudoinverse chooses the minimum norm solution, given by

$$\hat{\mathbf{u}} = \mathbf{H}^{*t}(\mathbf{H}\mathbf{H}^{*t})^{-1}\mathbf{p}. \tag{6.18}$$

2. Exact inverse solution

   When $M = N$, the pseudoinverse is simply the inverse of $\mathbf{H}$ and the solution is given by

$$\mathbf{u} = \mathbf{H}^{-1}\mathbf{p}. \tag{6.19}$$

3. The least-squares solution

   When $M > N$, Equation (6.10) represents an overdetermined system of equations which has a unique solution that minimizes the square error functional $\| \mathbf{Hu} - \mathbf{p} \|^2$. This solution takes the form

$$\hat{\mathbf{u}} = (\mathbf{H}^{*t}\mathbf{H})^{-1}\mathbf{H}^{*t}\mathbf{p}. \tag{6.20}$$

Note that the least-square solution is the solution to the constrained optimization problem, Equation (6.12), with $\gamma = 0$, i.e., no constraint on $\| \mathbf{u} \|^2$.

The above three special cases can be obtained in a straightforward manner by substituting for $\mathbf{H}$ and $\mathbf{H}^{*t}$ in Equation (6.18) and Equation (6.20) with their singular value decomposition ($\mathbf{H}^{*t} = \mathbf{V\Sigma U}^{*t}$).

In many cases of practical interest, it is desired to evaluate $\mathbf{u}$ based on a minimum number of control points in the field, e.g., the focal points and, possibly, any points where the field is to be forced to assume reduced levels to avoid potential hot spots in the heating pattern. In addition to its practical significance, the minimum norm solution offers several advantages which makes it most useful as a hyperthermia pattern synthesis technique. Therefore, this solution is emphasized in this thesis. The following subsection discusses the advantages of the minimum norm solution and provides a simple interpretation of how this technique works.

6.4.3 The minimum-norm solution

The minimum-norm solution offers several theoretical and practical advantages. From the practical view point, one is generally interested in specifying the field

at a small set of control points corresponding to the desired foci. In this case, the resulting underdetermined set of equations has an infinite number of solutions. The minimum-norm solution translates into a "minimum energy" solution at the surface of the array that is capable of providing the desired power deposition at the control points. This is an important property from an engineering perspective. This is especially important in hyperthermia since the objective is to utilize the array aperture efficiently to synthesize a desired pattern.

The minimum-norm solution reproduces the desired field values exactly at all the control points. To see this, simply examine the reconstructed field at the control points using $\hat{\mathbf{u}}$, $\mathbf{p}_r = \mathbf{H}\hat{\mathbf{u}}$. Substituting for $\hat{\mathbf{u}}$ by its minimum-norm solution, one can easily see that $\mathbf{p}_r = \mathbf{p}$, i.e., the resulting pressures at the control points are the same values specified by the vector $\mathbf{p}$. This is a very useful property of the minimum-norm solution since one might be interested in precisely controlling the relative power deposition levels at the control points.

The elements of the complex excitation vector vary in both amplitude and phase. A wide dynamic range of the amplitudes of the driving signals to the array elements means that the array operates with reduced array excitation efficiency, defined in Chapter 2. Hence, it might be necessary to increase the excitation efficiency of the array under some circumstances. This can be achieved by implementing the weighted minimum-norm solution. This solution can be easily derived from the unweigheted case in Equation (6.18) by defining a weighted inner product, $< \mathbf{p}_1, \mathbf{p}_2 >_{\mathbf{W}} = < \mathbf{p}_1, \mathbf{W}\mathbf{p}_2 >$ on the control-point space. The weighting matrix, $\mathbf{W}$, is an $N \times N$ positive definite matrix. This redefines the adjoint operator, $\mathbf{H}^{*t}$ of $\mathbf{H}$,

$$\mathbf{H}^{*t} : C^M \longrightarrow C^N \text{ such that } < \mathbf{Hu}, \mathbf{p} >_{\mathbf{W}} \stackrel{\text{def}}{=} < \mathbf{u}, \mathbf{WH}^{*t}\mathbf{p} > . \tag{6.21}$$

The weighted minimum-norm solution can be obtained by substituting $\mathbf{WH}^{*t}$ for

$\mathbf{H}^{*t}$ in Equation (6.18). The weighted minimum-norm solution takes the form

$$\hat{\mathbf{u}}_w = \mathbf{W}\mathbf{H}^{*t}(\mathbf{H}\mathbf{W}\mathbf{H}^{*t})^{-1}\mathbf{p}. \tag{6.22}$$

The judicious choice of $\mathbf{W}$ can achieve significant improvement in the array excitation efficiency when compared to the unweighted solution. A weighting algorithm based on the weighted minimum-norm solution is given in Chapter 7.

Another quantity which is useful to optimize is the *intensity gain* at the control points. This quantity is defined by

$$G = \frac{\| \mathbf{p} \|^2}{\| \hat{\mathbf{u}} \|^2} \tag{6.23}$$

where the norms of $\mathbf{p}$ and $\hat{\mathbf{u}}$ are taken in their respective spaces. Substituting for $\hat{\mathbf{u}}$ yields the following formula for the gain

$$G = \frac{\| \mathbf{p} \|^2}{\mathbf{p}^{*t}(\mathbf{H}\mathbf{H}^{*t})^{-1}\mathbf{p}}. \tag{6.24}$$

Techniques for maximizing the intensity gain of multiple-focus field patterns are given in Chapter 7. Simulation results show that the maximization of gain can result in a dramatic reduction of interference patterns in the synthesized field. This could eliminate a major difficulty with multiple-focus pattern synthesis.

An important advantage of the minimum-norm solution is its simple structure in which the mathematical operators are easily interpreted in terms of propagation phenomena. This can be helpful in understanding how the general pseudoinverse method accounts for various degradations associated with the propagation process. The reconstructed field at the control points $\mathbf{p}_r$ is obtained by a cascade of operators. First, the vector $\mathbf{p}$ is transformed into $\mathbf{p}_w = (\mathbf{H}\mathbf{H}^{*t})^{-1}\mathbf{p}$ which belongs to an intermediate control-point space by the matrix operator, $(\mathbf{H}\mathbf{H}^{*t})^{-1}$ which is a Hermitian matrix. This operator will be referred to as a pre-emphasis operator (this name will be justified shortly). Secondly, the excitation vector $\hat{\mathbf{u}}$ is obtained by backpropagating $\mathbf{p}_w$ to the surface of the array, $\hat{\mathbf{u}} = \mathbf{H}^{*t}\mathbf{p}_w$. Thirdly, the reconstructed field

at the control points is obtained by applying the forward propagation operator to $\hat{\mathbf{u}}$, $\mathbf{p}_r = \mathbf{H}\hat{\mathbf{u}}$. At this point, one should realize that both $\mathbf{H}$ and $\mathbf{H}^{*t}$ are, in fact, degradation operators. The degradation introduced by these operators is due to attenuation, element directivity, and the fact that propagation (both forward and backward) is a spatial lowpass filter with cutoff frequency $k_c = \frac{2\pi}{\lambda}$ associated with $1/r$ amplitude loss (λ and r are the wavelength and propagation distance, respectively). It is easily seen that the pre-emphasis operator is the exact inverse of the cascade $\mathbf{H}\mathbf{H}^{*t}$ that takes $\mathbf{p}_w$ into $\mathbf{p}_r$. In other words, the application of the pre-emphasis operator to the vector $\mathbf{p}$ corrects for the combined degradation introduced by the backward propagation-forward propagation cascade prior to the application of these operators to obtain $\mathbf{p}_r$, hence the name pre-emphasis.

An analogous interpretation can be given to the generalized inverse in Equation (6.17). Substituting for the pseudoinverse in Equation (6.17) yields

$$\hat{\mathbf{u}} = \bar{\mathbf{V}}\boldsymbol{\Sigma}^{-1}\mathbf{U}^{*t}\mathbf{p}. \tag{6.25}$$

First, the operator $\mathbf{U}^{*t}$ represents an orthogonal decomposition of the vector $\mathbf{p}$ with respect to the orthonormal vector set $\{\mathbf{u}_i : i = 1, 2, \ldots, M\}$. The $\mathbf{u}_i$'s are the columns of the matrix $\mathbf{U}$ (they do not represent excitation vectors here). The orthogonally decomposed vector is

$$\mathbf{p}_o = \mathbf{U}^{*t}\mathbf{p}. \tag{6.26}$$

Secondly, the operator $\boldsymbol{\Sigma}^{-1}$ is applied to the decomposed vector $\mathbf{p}_o$. The application of this operator normalizes the coefficients of the vector $\mathbf{p}_o$ to compensate for the various degradations due to forward and backward propagation as stated above. This results in the normalized vector

$$\mathbf{p}_n = \boldsymbol{\Sigma}^{-1}\mathbf{p}_o. \tag{6.27}$$

Thirdly, the operator $\mathbf{V}$ is applied to the normalized vector to obtain $\hat{\mathbf{u}}$. This operator represents a linear combination operator and is, in a sense, equivalent to the

backpropagation operator.

Finally, one can claim that specifying the field at a set of control points results in focusing the array at these points. It is very hard to prove this claim analytically. However, simulation results performed for this thesis and elsewhere [55], show that energy concentration or focusing occurs at the control points. It is also possible to gain some insight into this by analyzing single-focus and double-focus syntheses in some detail. To do this, one needs to define an $N \times 1$ matrix $\mathbf{h}$ which represents the forward propagation operator from the array surface to a single field point at $\mathbf{r}$. The propagation equation defined by $\mathbf{h}$ is

$$\mathbf{hu} = p \tag{6.28}$$

where p is the complex pressure at $\mathbf{r}$. The single-focus case is considered first.

The excitation vector resulting from focusing the array at a single point at $\mathbf{r}_1$ is given by

$$\hat{\mathbf{u}} = \frac{\mathbf{h}_1^{*t}}{\mathbf{h}_1\mathbf{h}_1^{*t}} p_1, \tag{6.29}$$

where p_1 is the specified complex pressure at $\mathbf{r}_1$. The complex pressure p at a point $\mathbf{r}$ in the field is given by

$$p = \frac{\mathbf{h}\mathbf{h}_1^{*t}}{\mathbf{h}_1\mathbf{h}_1^{*t}} p_1, \tag{6.30}$$

from which one obtains the power deposition at $\mathbf{r}$ which is proportional to

$$Q = \frac{|\mathbf{h}\mathbf{h}_1^{*t}|^2}{|\mathbf{h}_1\mathbf{h}_1^{*t}|^2} Q_1, \tag{6.31}$$

where Q_1 is the power deposition level at $\mathbf{r}_1$. Using the Cauchy-Schwartz inequality [22], one gets

$$Q \leq \frac{||\mathbf{h}||^2||\mathbf{h}_1||^2}{|\mathbf{h}_1\mathbf{h}_1^{*t}|^2} Q_1. \tag{6.32}$$

with equality when $\mathbf{h} = \gamma\mathbf{h}_1$ (γ is a real constant). Therefore, the power deposition assumes its maximum value when $\mathbf{h}$ points in the direction of $\mathbf{h}_1$, i.e., at the focal point. At points other than the focal point, the inner product $\mathbf{h}\mathbf{h}_1^{*t}$ represents the

point-spread function of the array at $\mathbf{r}_1$. Since the inner product in the numerator is the only quantity that varies with $\mathbf{r}$, the power deposition profile is determined by the point-spread function of the array at $\mathbf{r}_1$ with a maximum at $\mathbf{r}_1$, i.e., focusing.

A detailed analysis of a double-focus case might be helpful in understanding the different components of the solution vector $\hat{\mathbf{u}}$ when multiple-focus field patterns are synthesized. To illustrate this, assume the field is specified at two points $\mathbf{r}_1$ and $\mathbf{r}_2$ with complex pressures p_1 and p_2, respectively. The propagation equation corresponding to this case is given by

$$\begin{pmatrix} \mathbf{h}_1 \\ \mathbf{h}_2 \end{pmatrix} \mathbf{u} = \begin{pmatrix} p_1 \\ p_2 \end{pmatrix}. \tag{6.33}$$

The minimum-norm solution is then given by

$$\hat{\mathbf{u}} = \begin{pmatrix} \mathbf{h}_1^{*t} & \mathbf{h}_2^{*t} \end{pmatrix} \begin{pmatrix} \mathbf{h}_1\mathbf{h}_1^{*t} & \mathbf{h}_1\mathbf{h}_2^{*t} \\ \mathbf{h}_2\mathbf{h}_1^{*t} & \mathbf{h}_2\mathbf{h}_2^{*t} \end{pmatrix}^{-1} \begin{pmatrix} p_1 \\ p_2 \end{pmatrix}. \tag{6.34}$$

Manually inverting the 2×2 matrix and performing the algebraic manipulation results in

$$\hat{\mathbf{u}} = \Gamma \left(\mathbf{h}_1^{*t} \frac{p_1}{D_1^2} - \mathbf{h}_1^{*t}\mathbf{h}_1\mathbf{h}_2^{*t} \frac{p_2}{D_1^2 D_2^2} + \mathbf{h}_2^{*t} \frac{p_2}{D_2^2} - \mathbf{h}_2^{*t}\mathbf{h}_2\mathbf{h}_1^{*t} \frac{p_1}{D_1^2 D_2^2} \right), \tag{6.35}$$

where

$$\Gamma = \frac{D_1^2 D_2^2}{D_1^2 D_2^2 - \mathbf{h}_1\mathbf{h}_2^{*t}\mathbf{h}_2\mathbf{h}_1^{*t}}. \tag{6.36}$$

The real numbers $D_1^2 = \mathbf{h}_1\mathbf{h}_1^{*t}$ and $D_2^2 = \mathbf{h}_2\mathbf{h}_2^{*t}$ represent the array directivity factors at $\mathbf{r}_1$ and $\mathbf{r}_2$, respectively.

The formula for $\hat{\mathbf{u}}$ suggests that the excitation vector is obtained by summing the direct-focusing terms (the first and third terms in the above equation) and subtracting the indirect focusing terms (the second and fourth terms in the equation). A close examination of the indirect focusing terms reveals the mechanism by which the minimum norm solution accounts for multiple focusing. Consider the second term in the equation, it is the component of the excitation vector resulting from the cascade

action of $\mathbf{h}_2^{*t}, \mathbf{h}_1$, and $\mathbf{h}_1^{*t}$, in that order, on the control point at $\mathbf{r}_2$. The first operator $\mathbf{h}_2^{*t}$ (scaled by $1/D_2^2$) finds the excitation vector corresponding to a single-focus at $\mathbf{r}_2$. The second operator $\mathbf{h}_1$ computes the pressure at $\mathbf{r}_1$ resulting from this excitation vector; call this the residual pressure at $\mathbf{r}_1$ due to the focus at $\mathbf{r}_2$. The third operator $\mathbf{h}_1^{*t}$ (scaled by $1/D_1^2$) finds the excitation vector due to the residual pressure at $\mathbf{r}_1$. This is subtracted from the direct focusing term at $\mathbf{r}_1$. The fourth term in the equation corresponds to the residual pressure at $\mathbf{r}_2$ due to the focus at $\mathbf{r}_1$ and affects the direct focusing term at $\mathbf{r}_2$ in exactly the same way. This guarantees that the complex pressure at either of the control points is exactly equal to its specified value. To see this, the pressure at a point $\mathbf{r}$ in the field due to the overall excitation vector is given by

$$p = \Gamma \left(\mathbf{h}\mathbf{h}_1^{*t} \frac{p_1}{D_1^2} - \mathbf{h}\mathbf{h}_1^{*t}\mathbf{h}_1\mathbf{h}_2^{*t} \frac{p_2}{D_1^2 D_2^2} + \mathbf{h}\mathbf{h}_2^{*t} \frac{p_2}{D_2^2} - \mathbf{h}\mathbf{h}_2^{*t}\mathbf{h}_2\mathbf{h}_1^{*t} \frac{p_1}{D_1^2 D_1^2} \right). \tag{6.37}$$

One can clearly see that substituting $\mathbf{h}_1$ for $\mathbf{h}$ results in $p = p_1$. Similarly, substituting $\mathbf{h}_2$ for $\mathbf{h}$ results in $p = p_2$.

6.4.4 Numerical evaluation of the pseudoinverse operator

The pseudoinverse operator can be computed numerically, in its most general form, using the singular value decomposition, SVD, of the matrix $\mathbf{H}$. There exist several efficient subroutines implemented in standard mathematical libraries which evaluate the spectral value decomposition of a complex matrix $\mathbf{H}$. The simulations shown in this thesis use a LINPACK implementation subroutine to find the SVD of $\mathbf{H}$.

The minimum-norm solution requires evaluating the inverse of the $M \times M$ Hermitian matrix $\mathbf{H}\mathbf{H}^{*t}$ to find the pre-emphasis operator. This is followed by a matrix multiplication by the backpropagation operator $\mathbf{H}^{*t}$ (see Equation (6.18)). This can be easily computed by the usual inverse and matrix multiplication routines. However, the SVD subroutine is also used with the matrix $\mathbf{H}\mathbf{H}^{*t}$ since the singular values

and singular vectors obtained with this technique are valuable in the analysis of the propagation matrix.

In addition to the direct computation of the pseudoinverse using the SVD technique, iterative descent techniques to solve Equation (6.10) were also developed [14]. These techniques can be very useful when the size of the propagation matrix is too large or efficient subroutines to evaluate the SVD are not available. The successive approximation, steepest descent, and conjugate gradient techniques are guaranteed to converge to the minimum-norm least-squares solution obtained by the pseudoinverse [22]. These algorithms attempt to minimize the functional

$$f(\mathbf{u}) = ||\mathbf{H}\mathbf{u} - \mathbf{p}||^2, \tag{6.38}$$

which represents the square error in reconstruction. The functional f can be written explicitly as

$$f(\mathbf{u}) = \mathbf{u}^{*t}\mathbf{H}^{*t}\mathbf{H}\mathbf{u} - \mathbf{u}^{*t}\mathbf{H}^{*t}\mathbf{p} - \mathbf{p}^{*t}\mathbf{H}\mathbf{u} + \mathbf{p}^{*t}\mathbf{p}. \tag{6.39}$$

The conjugate gradient of this error functional with respect to $\mathbf{u}$ can be easily obtained and it takes the following form:

$$\nabla f^* = \mathbf{H}^{*t}(\mathbf{H}\mathbf{u} - \mathbf{p}). \tag{6.40}$$

Iterative techniques based on the above methods start with an initial estimate of $\hat{\mathbf{u}}$ (typically $\mathbf{0}$ to assure minimum-norm solution) and modifies this estimate by stepping in the direction of $-\nabla f^*$.

An iterative algorithm based on the steepest descent technique is given in [14]. The following algorithm illustrates the use of the conjugate gradient (CG) algorithm to solve Equation (6.10):

Step 0: $\hat{\mathbf{u}}_0 = \mathbf{0}$, the zero vector.

$$\mathbf{e}_0 = \mathbf{H}^{*t}[\mathbf{p} - \mathbf{H}\hat{\mathbf{u}}_0]$$

$$\mathbf{q}_0 = \mathbf{e}_0$$

Step 1: Iterate $i = 1, 2, \cdots$

$\hat{\mathbf{u}}_{i+1} = \hat{\mathbf{u}}_i + \gamma_i \mathbf{q}_i$

$\mathbf{e}_{i+1} = \mathbf{H}^{*t}[\mathbf{p} - \mathbf{H}\hat{\mathbf{u}}_{i+1}]$

$\mathbf{q}_{i+1} = \mathbf{e}_{i+1} + \alpha_i \mathbf{q}_i$

where

$\gamma_i = \frac{||\mathbf{e}_i||^2}{||\mathbf{H}\mathbf{q}_i||^2}$ and $\alpha_i = \frac{||\mathbf{e}_{i+1}||^2}{||\mathbf{e}_i||^2}$

Step 2: If

$\frac{\gamma^2 ||\mathbf{e}_i||^2}{||\mathbf{u}_i||^2} \geq \epsilon$,

Go to Step 1,

Else the excitation vector $\hat{\mathbf{u}} = \hat{\mathbf{u}}_i$.

In the above algorithm, the conjugate direction is determined by $\mathbf{e}_i = -\nabla f_i^*$. However, the step at the ith iteration is taken in the direction of $\mathbf{q}_i$ which memorizes all the previous steps (gradients). This formulation of the CG algorithm guarantees convergence in at most M steps for a size $M \times N$ propagation operator [22].

6.5 Numerical Examples of Multiple-Focus Synthesis

This section discusses a number of examples of multiple-focus field patterns synthesized using the pseudoinverse pattern synthesis method. These examples cover all of the different categories outlined in Chapter 5, i.e., multiple-focus, diffuse-focus, and directly-synthesized patterns. All nonplanar array structures described in Chapter 4 are used to demonstrate the generality of the pseudoinverse method. The number of elements and the dimensions of the different array structures simulated in this section are the same as those given in Chapter 4 unless stated otherwise. In some examples, pattern synthesis is performed both with the pseudoinverse and field conjugation and the results are compared. The simulated field profiles show clearly that the resulting field patterns satisfy the specified field pattern exactly at

the control points when the field is obtained using Equation (6.18).

A 64-element CSA1D was used to synthesize a four-focus field pattern in which the focal points were arbitrarily distributed across a transversal line passing the geometrical center of the array. The control points in this example were at $-6, 0, 12$, and 21 mm off the center of the array in the focal plane. For demonstration purposes, the relative intensity at all control points was chosen to be the same, i.e., $\mathbf{p} = P[1, 1, 1, 1]^t$ where P is a constant. The resulting intensity profiles for this case are shown in Figure 6.1. The result clearly shows that the relative intensity levels at the control points correspond to the specified values. Furthermore, a distinct focus corresponding to each control point can be identified. This is typical of synthesized fields in which the control points are separated by more than the dimensions of the point-spread function of the array. This result confirms the claim made earlier about the focusing capability of the minimum-norm solution.

To compare the performance of the pseudoinverse method with the previous methods described in Section 6.3, the field conjugation method was used to synthesize the field pattern shown in Figure 6.1. The resulting intensity profile is shown in Figure 6.2. One can clearly see that the field conjugation method fails to reproduce the desired relative intensity distribution at the control points. This is due to the fact that the field conjugation method obtains the driving signal distribution by applying the backpropagation operator to the elements of $\mathbf{p}$ directly and drops the pre-emphasis operator. Hence, the field conjugation method does not account for the degradation associated with backward and forward propagation operators resulting in error in synthesis. This error is not easily accounted for using ad hoc techniques. More significantly, this method does not provide any measure to characterize the resulting error.

The pseudoinverse method can also be used in synthesizing multiple-focus field patterns in which the focal points are located at different depths. Figure 6.3 shows

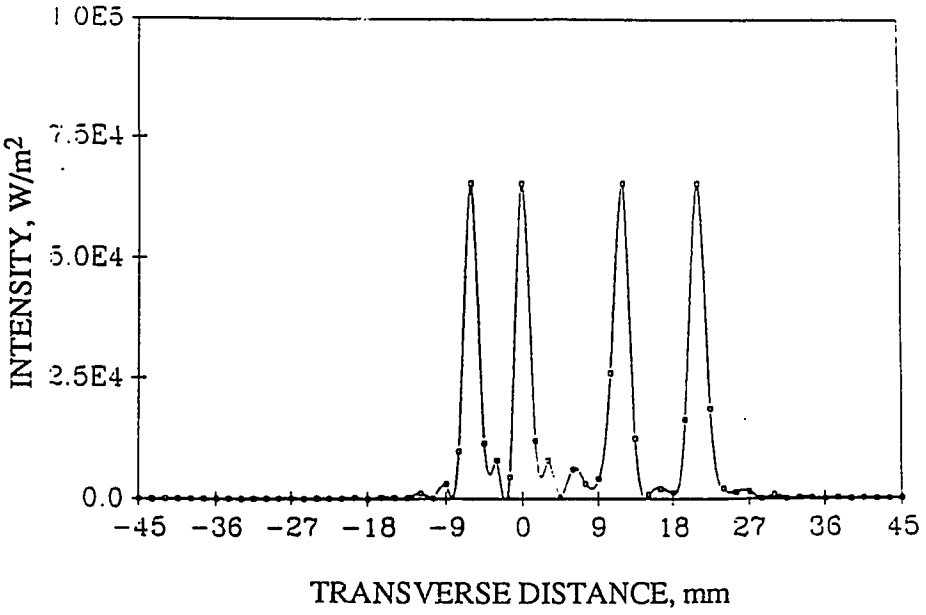

a) Transversal line passing through control points.

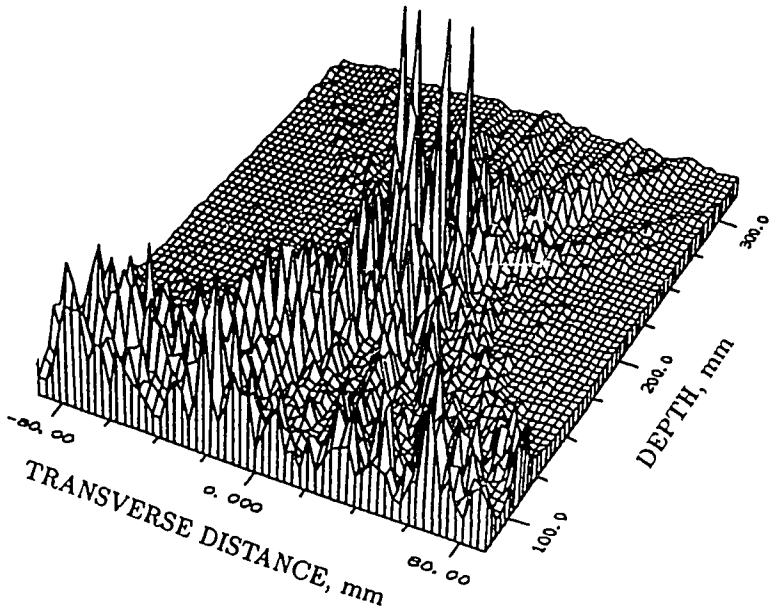

b) $z = 0$ plane.

Figure 6.1. Intensity profiles of a four-focus field patterns produced by the CSA1D using the pseudoinverse method.

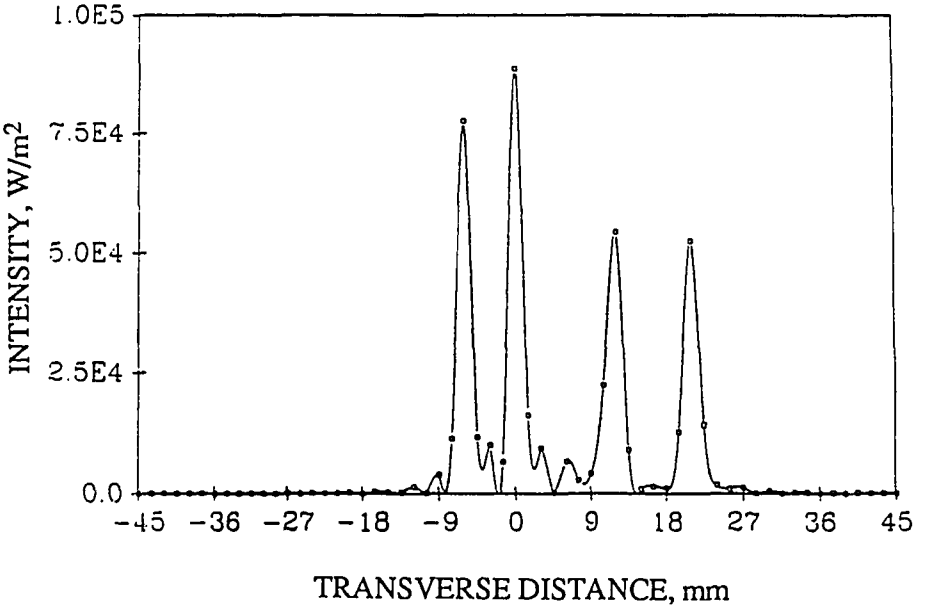

Figure 6.2. Intensity profile of a four-focus field pattern produced by the CSA1D using the field conjugation method.

the intensity profile of a two-focus field pattern in which the two control points were located at depths of 175 mm and 225 mm from the vertex of the CSA1D along a longitudinal line with off-axis distance of 21 mm. Once again the intensity levels at the control points were chosen to be equal which is clearly reflected in the resulting profile. The intensity profile obtained by the field conjugation method when used to synthesize this pattern is shown in Figure 6.4. The resulting intensity profile is shown in Figure 6.5. The intensity level at the deeper focus is -6.5 dB below the focal intensity of the one at 175 mm depth. It is important to note here that the relative magnitude of the two focal points produced by the field conjugation method does not depend solely on the absolute difference in depth between the two focal points.

A 12×10 CSA2D with a radius of 140 mm was used in synthesizing a three-focus field pattern in which three foci where distributed symmetrically along a vertical line at a depth of 140 mm and 15 mm off-axis distance. The control points were located at $z = -10$ mm, $z = 0$ and $z = 10$ mm with equal relative intensity. The resulting intensity profiles corresponding to this case are shown in Figure 6.5. Note that the intensity profile in the $z = 0$ plane basically corresponds to that of a shifted single-focus beam shown in Figure 4.7. The main difference between this 3-focus field pattern and the single-focus case is the formation of a significant interference pattern prior to the focal plane. This interference pattern is due to multiple focusing and the small number of elements used for this array. A gain maximization technique described in Chapter 7 is shown to significantly reduce this interference pattern.

Figure 5.4 was used to illustrate diffuse-focus patterns used in certain scanning applications. This field pattern was obtained by setting the pressure at seven control points distributed symmetrically along a vertical line according to the rule

$$p_i = P \sqrt{\frac{1 + \left(\frac{z_i}{r_t}\right)^2}{1 + \left(\frac{z_i}{r_t}\right)^4}}$$

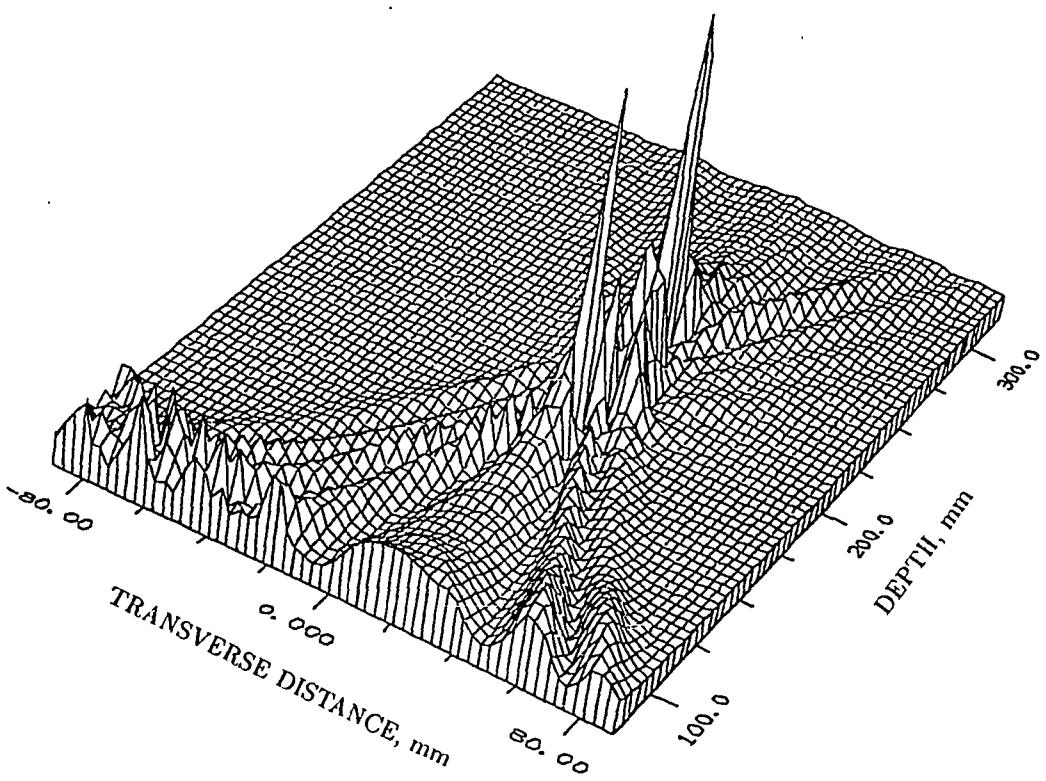

Figure 6.3. Intensity profile of a two-focus field pattern produced by the CSA1D using the pseudoinverse method.

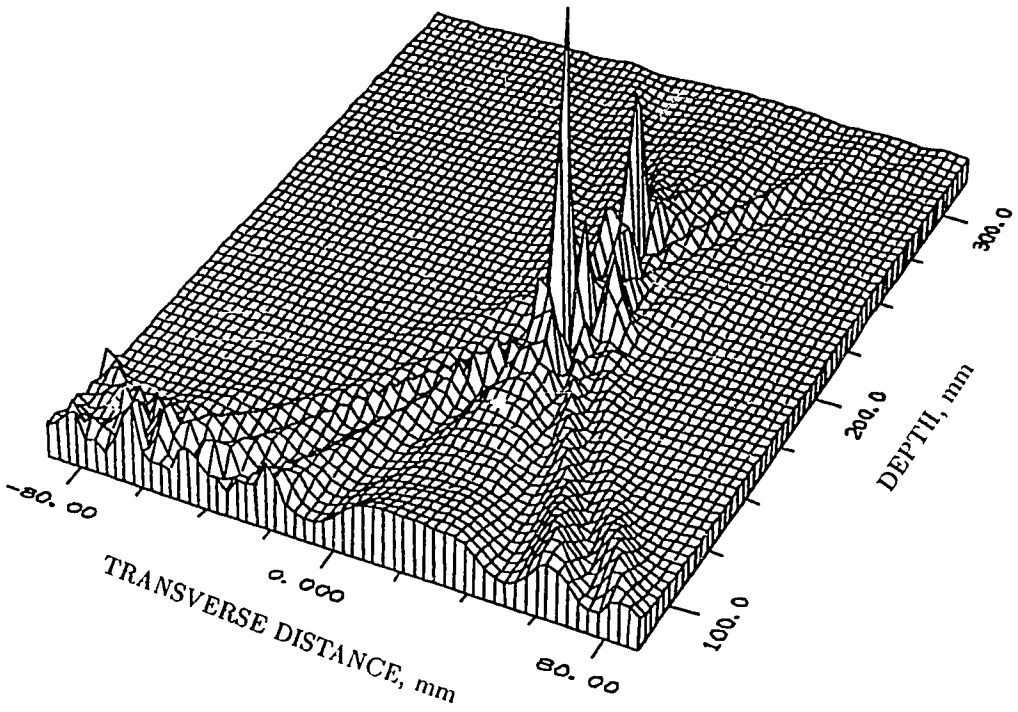

Figure 6.4. Intensity profile of a two-focus field pattern produced by the CSA1D using the field conjugation method.

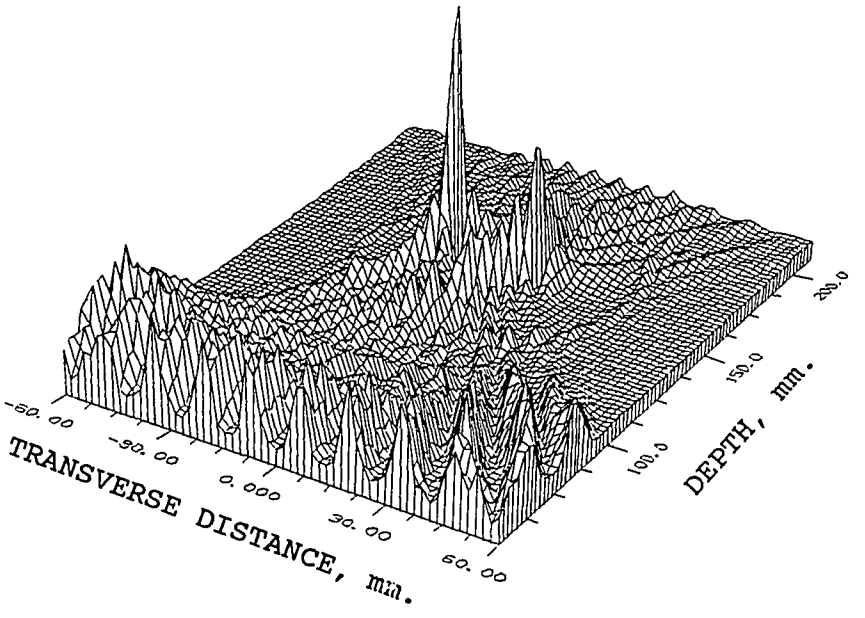

a) $z = 0$ plane.

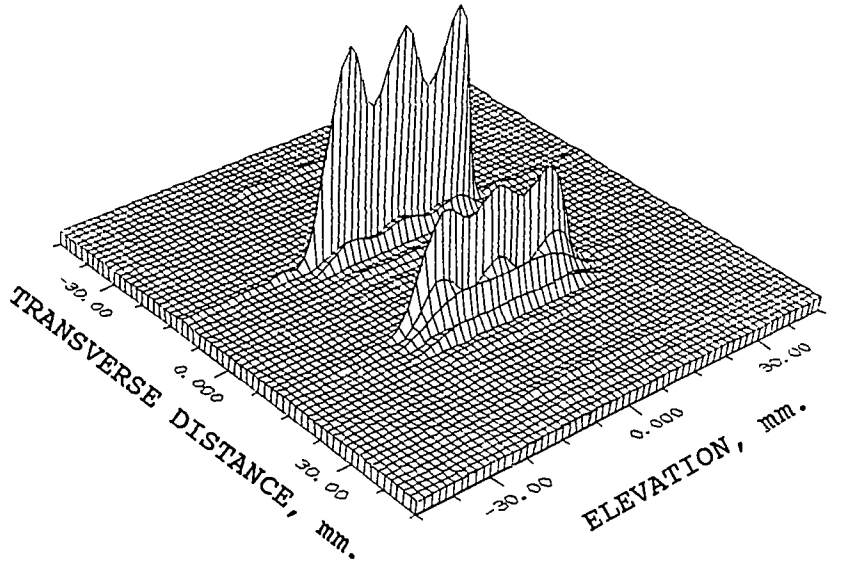

b) Focal plane.

Figure 6.5. Intensity profiles of a three-focus field pattern produced by the CSA2D using the pseudoinverse method.

where r_t is a constant, and $z_i = -r_t + \frac{2r_t}{7}(i-1)$, for $i = 1, 2, \ldots, 7$. The intensity profile for this diffuse focus along a vertical line is shown in Figure 6.6. In this case, r_t was chosen to be 10 mm. A close examination of Figure 6.6 shows clearly that the diffuse-focus intensity profile closely follows the formula

$$Q_i = Q_o \frac{1 + \left(\frac{z_i}{r_t}\right)^2}{1 + \left(\frac{z_i}{r_t}\right)^4}$$

where Q_o is the power deposition level at $z = 0$. The spacing between the control points in this case was nearly 5.2 mm which is slightly larger than the height (see Section 4.3.2) of the point-spread function of the array at the focal point. This spacing was determined to be sufficient to achieve continuity in the intensity profile. The choice of the optimal spacing between the control points necessary to produce the desired profile is discussed in Chapter 7.

The SSA was used to directly synthesize an annular ring pattern shown in Figure 5.5. To produce this pattern, a total of 28 control points were uniformly distributed around a 30 mm-diameter annular ring parallel to the aperture of the SSA at a depth of 100 mm. Annular heating patterns are very important in hyperthermia because they are believed to be ideal for heating spherical and cylindrical tumors. However, these patterns are typically associated with interference patterns prior and distal to the focal plane which can limit their usefulness. Figure 6.7 shows the intensity profile in the $z = 0$ plane corresponding to the focal plane pattern shown in Figure 5.5. One can clearly see the high intensity interference patterns forming along the central axis of the array in front of and beyond the focal plane. In fact, the intensity level at the focal ring is -8 dB below the maximum intensity occurring along the axis of the array.

The field pattern shown in Figure 6.7 represents a worst-case scenario of how the interference patterns can overshadow the desired heating pattern in the focal plane. The presence of such high-intensity interference patterns renders heat localization

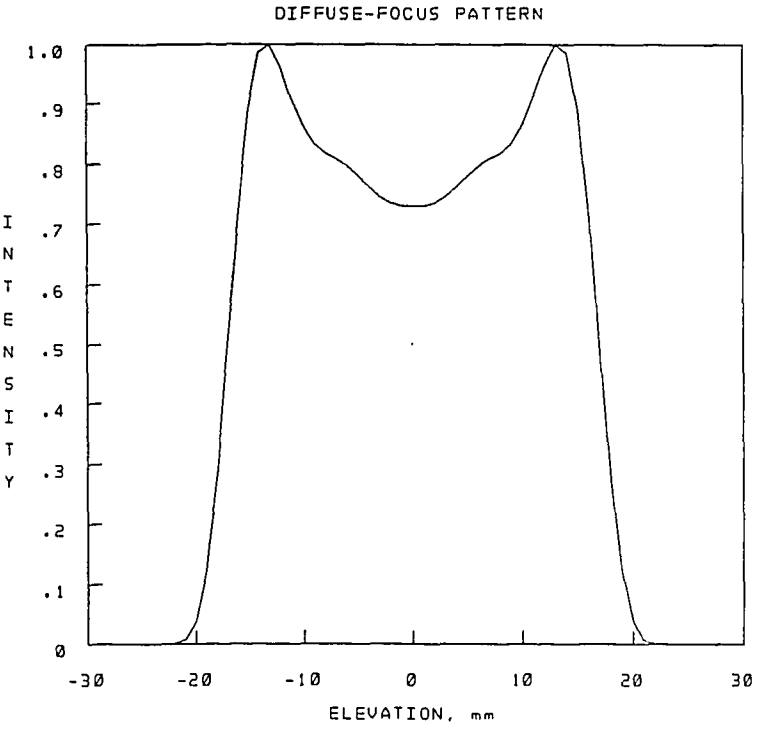

Figure 6.6. Intensity profile of the diffuse-focus pattern shown in Figure 5.4.

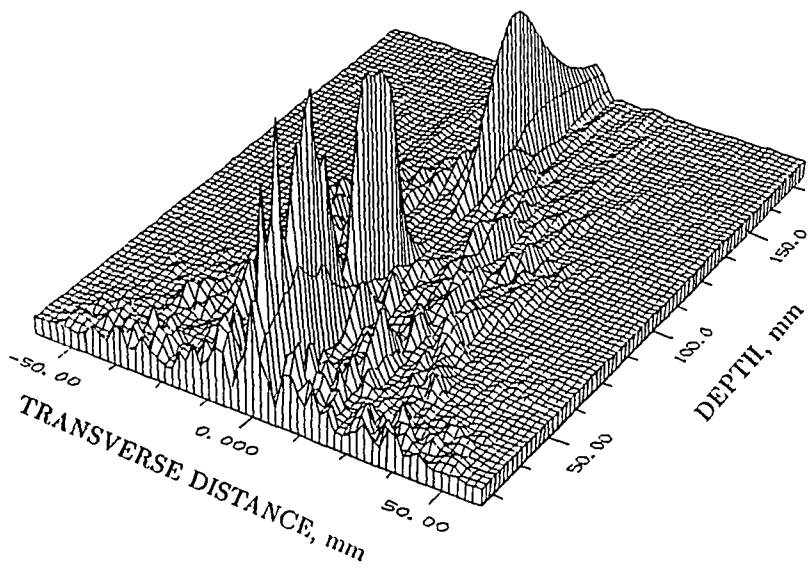

Figure 6.7. Intensity profile in the $z = 0$ plane associated with the annular ring pattern shown in Figure 5.5.

difficult. However, recognizing that the axial interference pattern shown is a result of the symmetry of the control points in the focal plane and inspired by the concept of phase rotation used with the sector-vortex array [17], a technique for removing this axial interference pattern was developed [76]. This can be achieved by choosing the complex pressures at the control points according to

$$p_i = p_o e^{j\frac{2\pi m}{M}(i-1)}; \quad \text{for } i = 1, 2, \ldots, M, \tag{6.41}$$

where M is the total number of control points forming the ring, and m (phase rotation index) is an integer equivalent to the vortex mode number. Stated in words, the last equation means that each two points that are spatially π radians apart have complex pressure values that are $m\pi$ apart. For $m \neq 0$, this phase distribution assures that the field along the axis of the array is identically zero, hence removing the axial interference. The interference pattern beyond the focal plane forms as a residual annular ring the diameter of which depends on the choice of the integer m above. In fact, analogous to the sector-vortex array, the interference pattern behaves as an mth order Bessel function. To prove this, one uses the Fresnel approximation of plane-to-plane propagation [64]

$$p(\rho, \phi, z_o) = \frac{e^{-jkz_o} e^{-j\frac{k\rho^2}{2z_o}}}{j\lambda z_o} \, FT\left\{p(\rho, \phi, 0) e^{-j\frac{k\rho^2}{2z_o}}\right\}, \tag{6.42}$$

where ρ, ϕ, and z represent the three-dimensional polar coordinates, $p(\rho, \phi, z)$ is the complex pressure field, $z = 0$ defines the focal plane and z_o defines the plane at which the pressure is computed, and $FT\{\cdot\}$ is the Fourier transform. If the complex pressure distribution at the control points satisfies Equation (6.41), then the pressure field in the focal plane can be expressed as follows:

$$p(\rho, \phi, 0) = p_o e^{j\frac{2\pi m}{M}(i-1)} \delta\left(\rho - a, \phi - \frac{2\pi m}{M}(i-1)\right), \tag{6.43}$$

where $\delta(\cdot)$ is the Dirac-delta function and a is the radius of the focal ring. Performing

the Fourier transform in polar coordinates with $k_\rho = \frac{k\rho}{z_o}$, one obtains

$$p(\rho, \phi, z_o) = \frac{e^{-jkz_o} e^{-j\frac{k(\rho^2+a^2)}{2z_o}}}{j\lambda z_o} \sum_{i=1}^{M} e^{jk\rho\cos(\phi_i)+jm\phi_i}, \tag{6.44}$$

where $\phi_i = \frac{2\pi m}{M}(i-1)$. The summation term appearing in the last equation can be substituted, in the limit, by an integral as follows:

$$\begin{aligned} \sum_{i=1}^{M} e^{jk\rho\cos(\phi_i)+jm\phi_i} &= \frac{M}{2\pi}\int_0^{2\pi} e^{jk\rho\cos(\phi)+jm\phi} d\phi \\ &= M e^{j\frac{m\pi}{2}} J_m(k\rho), \end{aligned} \tag{6.45}$$

where $J_m(k\rho)$ is the mth order Bessel function of the first kind. Substituting for the summation in Equation (6.44) results in

$$p(\rho, \phi, z_o) = \frac{e^{-jkz_o} e^{-j\frac{k(\rho^2+a^2)}{2z_o}}}{j\lambda z_o} M e^{j\frac{m\pi}{2}} J_m(k\rho). \tag{6.46}$$

This shows clearly that the envelope of the complex pressure field is an mth order Bessel function. Therefore, for $m \neq 0$, the pressure along the axis of the array beyond the focal plane is identically zero. The larger the value of the phase rotation index, m, the larger the diameter of the residual ring and the smaller its amplitude. This means that interference patterns can be effectively eliminated beyond the focal plane. However, the phase rotation index cannot be chosen to be arbitrarily large. This is due to the fact that the larger the value of m the higher the spatial frequency of the focal pattern. Hence, depending on the spacing between the control points, certain values of m result in spatial frequencies larger than $\frac{1}{\lambda}$ in the focal pattern which represent evanescent modes which are unrealizable. Furthermore, the above discussion does not apply the volume between the array surface and the focal plane where high intensity interference patterns can still be formed. An example of an annular-ring pattern obtained by the phase rotation technique is given in Chapter 7.

The interference patterns associated with multiple-focus field patterns can significantly limit their usefulness. For certain cases, one might be able to find a phase

distribution of the complex pressures at the control points to reduce such interference patterns. However, this is insufficient and leaves a lot of room for unguided experimentation with phase distributions. In Chapter 7, a gain maximization method based on Equation (6.24) is shown to significantly reduce interference patterns associated with several useful multiple-focus patterns. The method assigns values for the phases of the control-point vector, $\mathbf{p}$, derived from the propagation matrix, $\mathbf{H}$, and does not assume any prior knowledge of the phases of the elements of $\mathbf{p}$. The effect of the gain maximization scheme on interference patterns associated with the annular-ring pattern and the three-focus pattern (Figure 6.5) will be discussed. Interestingly enough, the gain maximization technique results in phase distributions of the elements of $\mathbf{p}$ that result in removal of interference patterns prior and beyond the focal plane.

CHAPTER 7

OPTIMIZATION OF THE DRIVING-SIGNAL DISTRIBUTIONS

7.1 General

In Chapter 6, the pattern synthesis problem was defined and was solved as a general least-squares problem using the pseudoinverse method. The minimum-norm solution was shown to produce the desired field level at the control points for **H** full rank. The solution chosen by the pseudoinverse operator is "optimal" in the sense that it is the minimum-norm vector that produces the least-square error in the reconstructed field. However, the "optimality" of the solution can be defined with respect to other parameters which can be of more significance in hyperthermia.

Two such parameters were identified to be potentially important under certain circumstances. The first of these parameters, *array excitation efficiency* (η_A), was defined in Chapter 2. This parameter reflects the uniformity of the amplitude distribution of the driving signals across the elements of the array. Ideally, one would like to synthesize multiple-focus field patterns with uniform amplitude distribution. Hence, an excitation vector might be considered optimal if it maximizes the parameter η_A. The second parameter, *intensity gain* (G), was defined in Chapter 6. This parameter reflects the ratio of the power deposition levels at the control points to the average power available at the surface of the array. The higher the intensity gain,

the higher the ability of the array to concentrate energy at the control points.

The choice of an excitation vector, $\mathbf{u}$, can be based on factors other than excitation efficiency and intensity gain. One very important factor is the robustness of the synthesized pattern. This factor reflects the behavior of the error functional, $\| \mathbf{Hu} - \mathbf{p} \|^2$, with respect to variations in the excitation vector, $\mathbf{u}$. The objective here is to choose an excitation vector, $\mathbf{u}$, such that a small error in this vector results in a small error in the synthesized field. It turns out that this is a property of the propagation matrix, $\mathbf{H}$. In other words, it is a function of the control-point placement in the field. The robustness of the synthesized pattern is associated with the condition number of the matrix, $\mathbf{H}$. The condition number, $cond_2(\mathbf{H})$ (defined with the L_2 norm), is the ratio of the largest singular value to the smallest singular value of the matrix. A large condition number of the propagation matrix indicates an ill-conditioned matrix which results in a synthesized field that is very sensitive to errors in $\mathbf{u}$. This requires one to find the optimal placement of the control points in the field to assure stable synthesis.

This chapter describes methods for optimization of excitation vectors with respect to array excitation efficiency, intensity gain, and optimal placement of control points. The minimum-norm solution is used throughout this chapter. The main reason for this choice is that the minimum-norm solution guarantees that the relative intensity levels at the control points are not changed by optimization techniques. This allows meaningful comparisons between the optimized field patterns and the unoptimized ones.

7.2 Optimization of Array Excitation Efficiency

The elements of the excitation vector vary in both amplitude and phase from element to element at the surface of the array. This is typical of most pattern synthesis methods (except for phase-only synthesis methods). The power available at the surface of an ultrasonic piezoelectric transducer is limited by the maximum

intensity a particular piezoelectric material can support. A wide dynamic range of the amplitudes of the driving signals to the array elements could mean that some of the array elements are being driven very hard while other elements are hardly utilized. This situation is clearly undesirable. In fact, this situation could mean that the array cannot provide sufficient power deposition in the target volume. Improving the array excitation efficiency allows the array to provide more power at its surface for realistic tumor heating. Furthermore, uniform amplitude excitation signals could result in great simplification in the driving electronics to the array elements.

An obvious approach for improving the array excitation efficiency is by suppressing the dynamic range of the excitation vector. One can see that the weighted minimum-norm solution can be used to achieve this objective. This can be achieved by suitably choosing the elements of the weighting matrix $\mathbf{W}$. The choice of the elements of $\mathbf{W}$ is arbitrary as long as it is a positive-definite $N \times N$ matrix. One intuitive choice of $\mathbf{W}$ is such that $\mathbf{W} = diag\{1/|u_1|, 1/|u_2|, \ldots, 1/|u_N|\}$ where the $|u_i|$'s are the amplitudes of the driving signals for the unweighted case. This choice of the elements of $\mathbf{W}$ is inspired by the single-focus case (applying this weighting matrix to any single-focus excitation vector results in $\eta_A = 100\%$). When this weighting matrix is applied to an excitation vector resulting from a multiple-focus pattern, it consistently results in improved efficiency. However, the resulting efficiency is generally less than 100%. Therefore, a weighting algorithm was developed to increase the array excitation efficiency to the desired level by repeatedly applying the weighted minimum-norm solution as follows:

Step 0: $\mathbf{W} = \mathbf{I}$, the identity matrix.

Step 1: Compute $\hat{\mathbf{u}}_w, \eta_A$ using

$$\hat{\mathbf{u}}_w = \mathbf{W}\mathbf{H}^{*t}(\mathbf{H}\mathbf{W}\mathbf{H}^{*t})^{-1}\mathbf{p},$$

$$\eta_A = \frac{\sum_{n=1}^{N} |\hat{u}_{wn}|^2}{NU_{max}} \times 100\%$$

If η_A is sufficient go to Step 3

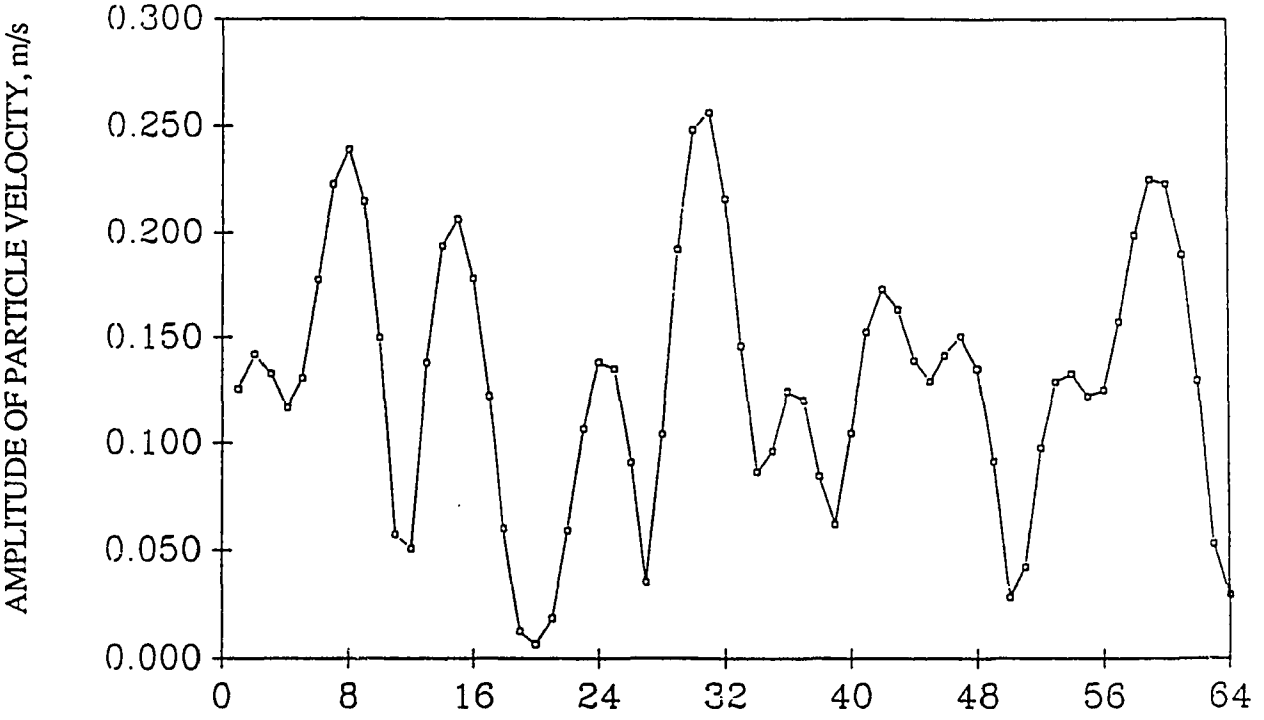

Figure 7.1. Amplitude distribution of the driving signals to the CSA1D responsible for producing Figure 6.1.

else $\mathbf{H}^{*t} = \mathbf{W}\mathbf{H}^{*t}$

Step 2: Evaluate new weighting matrix $\mathbf{W}$ such that

$$W(m,n) = \begin{cases} \frac{1}{|\hat{u}_{wn}|}, & \text{for } m = n; \\ 0, & \text{otherwise.} \end{cases}$$

Go to *Step 1*

Step 3: The excitation vector $\hat{\mathbf{u}} = \hat{\mathbf{u}}_w$.

This weighting algorithm, although straightforward, proved to be very useful in increasing the array excitation efficiency to near 100% with most field patterns. As a typical example of the performance of this weighting algorithm, consider the field pattern shown in Figure 6.1. The amplitude distribution corresponding to this case is shown in Figure 7.1. This signal has a large dynamic range which would result in low excitation efficiency. Indeed, the array excitation efficiency corresponding to this distribution is only 30%. To increase the array excitation efficiency, the weighting

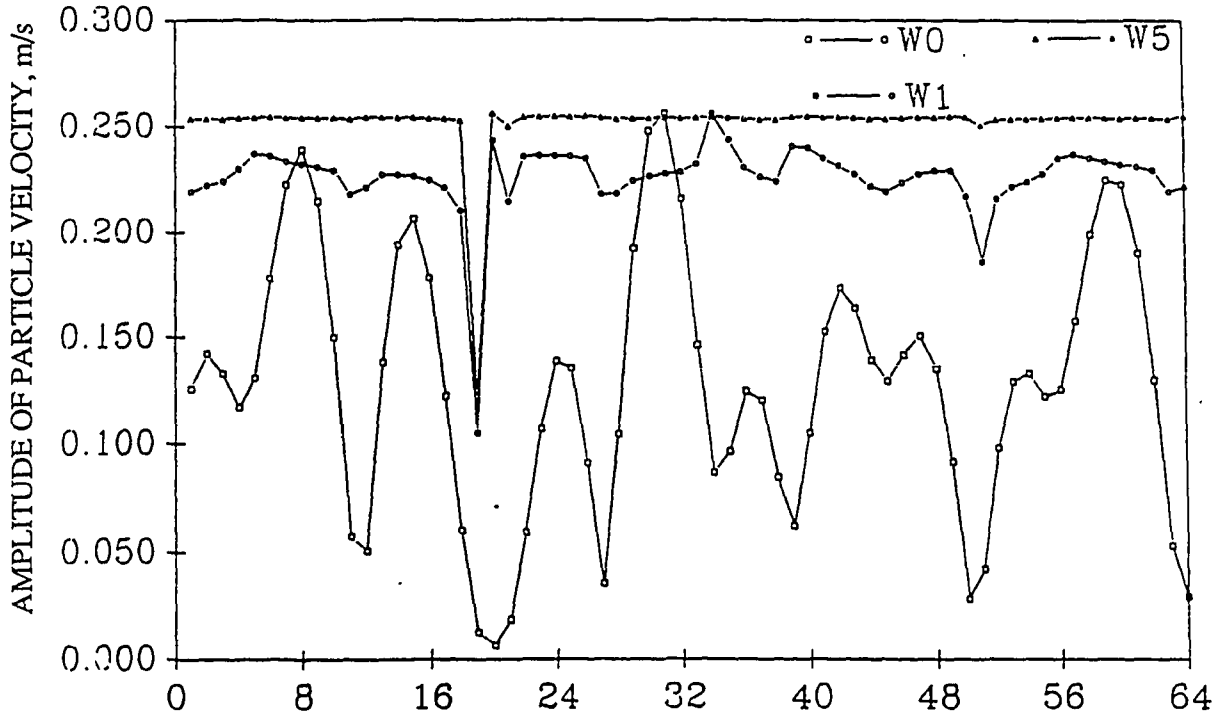

Figure 7.2. Amplitude distributions obtained by the pseudoinverse method with different weightings. W0 no weighting, W1 weighted once, and W5 weighted five times.

algorithm described herein was applied to the excitation vector. Figure 7.2 shows the amplitude distributions of the excitation vectors for the unweighted solution (W0), the weighted solution after one iteration (W1), and the weighted solution after five iterations (W5). The array excitation efficiency was improved to 78.4% after the first iteration and to 97.3% after the fifth iteration. Figure 7.3 shows the corresponding intensity profiles in the focal plane. This result indicates clearly that the increase in the array excitation efficiency translates into an increase in the power deposition level in the field.

Another advantage of the weighting algorithm is that it could provide a possible means of phase-only synthesis, i.e., the excitation vectors have uniform amplitude distributions. To demonstrate this with an example, the amplitude distribution of the W5 case above was replaced by a uniform amplitude distribution while maintaining

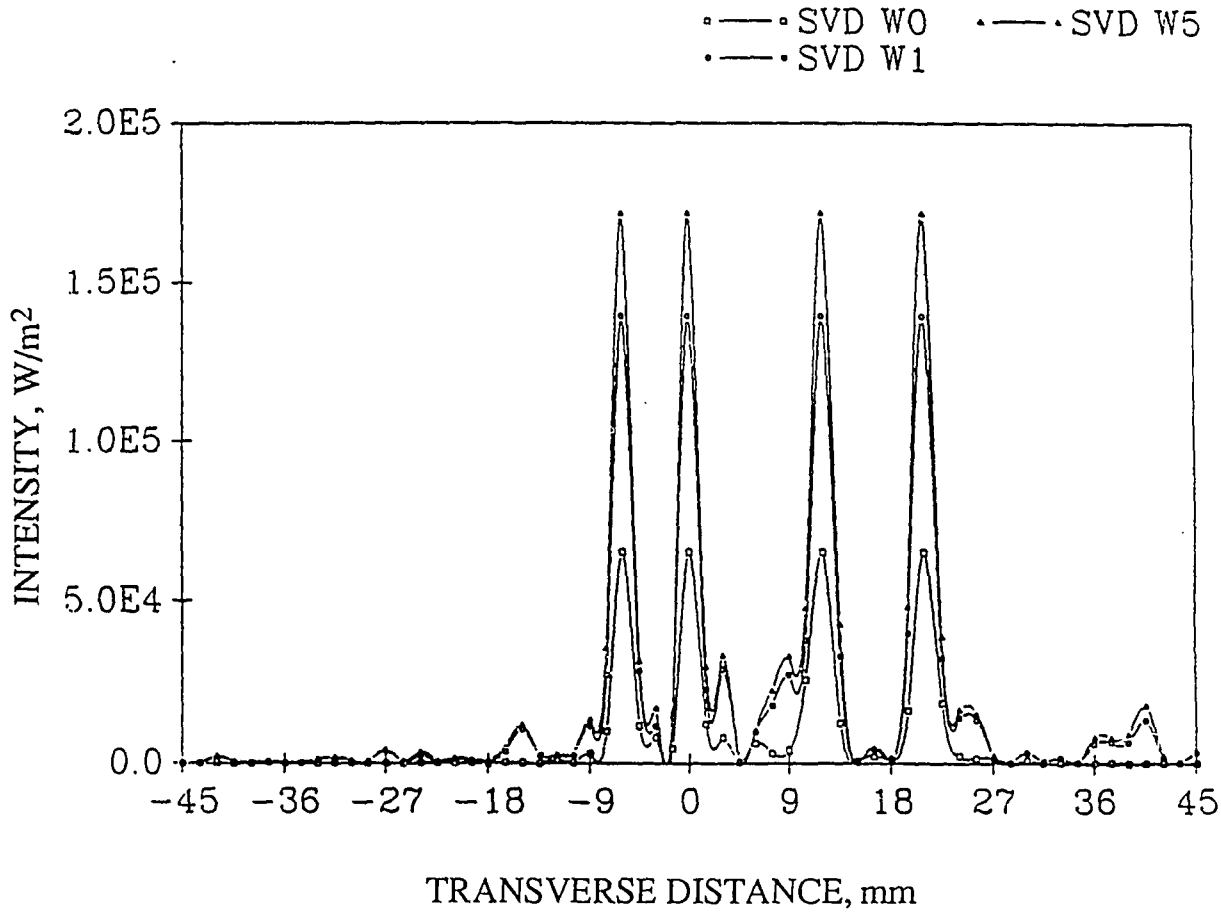

Figure 7.3. Intensity profiles in the focal plane corresponding to different weighted solutions shown in Figure 7.2.

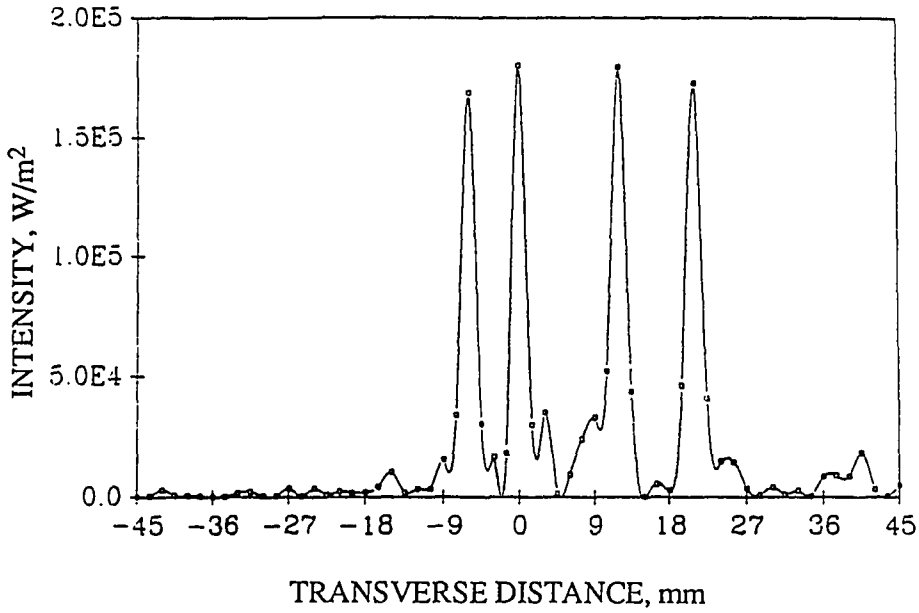

Figure 7.4. Intensity profile of phase-only excitation vector distribution obtained from W5 solution with uniform amplitude.

the phase distribution. When this new excitation vector was used to compute the field in the focal plane, the intensity profile of Figure 7.4 resulted.

7.3 Optimization of Intensity Gain

The definition of the intensity gain given in Chapter 7 provides a measure of the efficiency with which the power available at the surface of the array is transmitted to the control points. The formula derived for this quantity based on the minimum-norm solution is given by

$$G = \frac{\mathbf{p}^{*t}\mathbf{p}}{\mathbf{p}^{*t}(\mathbf{H}\mathbf{H}^{*t})^{-1}\mathbf{p}}. \tag{7.1}$$

One can see that, for a certain selection of control- point locations (which determines $\mathbf{H}$), the value of intensity gain is a function of the complex pressure values at the control points.

Typically, the pressure levels at the control points are chosen based on the desired

power deposition at these points, which is a phase-insensitive quantity. This gives one the freedom of choosing the phases of the complex pressures at the control points to maximize the gain. Two approaches were taken in solving this problem. The first approach was to choose an arbitrary initial phase distribution for complex pressure at the control points and incrementally change the phases at these points in a direction that maximizes G. This led to the iterative procedure given in the following subsection.

The second approach was to determine the control-point vector with arbitrary amplitude and phase distribution that maximizes G. The phase distribution at this maximizing vector was then combined with the amplitude distribution specified by the desired power deposition at the control points. This approach results in a "suboptimal" solution. However, it can be evaluated directly and typically results in a dramatic improvement in intensity gain at the control points. This approach is described in Section 7.3.2 below.

7.3.1 Iterative method for gain maximization

This method assumes that the vector $\mathbf{p}$ of complex pressures at the control points takes the following form

$$\mathbf{p} = \begin{pmatrix} p_1 e^{j\gamma_1} \\ p_2 e^{j\gamma_2} \\ \vdots \\ p_M e^{j\gamma_M} \end{pmatrix}, \tag{7.2}$$

where the p_i's are the initial complex pressures at the control points and the γ_i's are the correction phases to be determined. Examining the numerator of the formula for G shows that the term $\mathbf{p}^{*t}\mathbf{p}$ is constant independent of the choice of the γ_i's. Hence maximizing G amounts to minimizing the term in the denominator $\Gamma = \mathbf{p}^{*t}(\mathbf{H}\mathbf{H}^{*t})^{-1}\mathbf{p}$, which can be expressed as a double sum of the form

$$\Gamma = \sum_m \sum_n p_m^* S_{mn} p_n e^{j(n-m)}, \tag{7.3}$$

where S_{mn} is the mnth element of the matrix $(\mathbf{H}\mathbf{H}^{*t})^{-1}$. Now, taking the derivative of Γ with respect to γ_l yields

$$\frac{\partial \Gamma}{\partial \gamma_l} = -jp_l^* e^{-j\gamma_l} \sum_{n \neq l} S_{ln} p_n e^{j\gamma_n} + jp_l e^{j\gamma_l} \sum_{m \neq l} p_m^* e^{-j\gamma_m} S_{ml}. \tag{7.4}$$

Using the fact that $(\mathbf{H}\mathbf{H}^{*t})^{-1}$ is Hermitian, i.e., $S_{mn} = S_{nm}^*$, and setting the derivative equal to zero results in an extremum at

$$\hat{\gamma}_l = \arg\left(\sum_{n \neq l} S_{ln} p_n e^{j\gamma_n}\right) + \arg(p_l^*). \tag{7.5}$$

For γ_l to be a minimum, the condition

$$\frac{\partial^2 \Gamma}{\partial \gamma_l^2} > 0 \tag{7.6}$$

must be satisfied at $\hat{\gamma}_l$. The second derivative can be easily obtained and shown to have the following form

$$\frac{\partial^2 \Gamma}{\partial \gamma_l^2} = -2\mathrm{Rc}\left\{p_l^* e^{-j\gamma_l} \sum_{n \neq l} S_{ln} p_n e^{j\gamma_n}\right\}, \tag{7.7}$$

which shows clearly that if $\hat{\gamma}_l$ corresponds to a maximum, then $\hat{\gamma}_l + \pi$ corresponds to a minimum.

The derivation shown above suggests that the current value of $\hat{\gamma}_l$ that minimizes Γ (maximizes G) is a function of all the other γ_n's. This means that the final phase distribution of the complex pressure on the control points needs to be determined iteratively. An iterative algorithm to determine the optimal phase distribution at the control points is as follows:

Step 0: Choose $\gamma_1^{(0)}, \gamma_2^{(0)}, \ldots, \gamma_M^{(0)}$

Step 1: For $i = 1, 2, \ldots$ Do Steps 2 and 3

Step 2: For $l = 1, 2, \ldots, M$

Compute

$D = \sum_{n \neq l} S_{ln} p_n^* e^{j\gamma_n^{(i-1)}}$

$\hat{\gamma}_l^{(i)} = \arg(p_l^* D)$

If

$\frac{\partial^2 \Gamma}{\partial \gamma_l^2} = -2\mathrm{Re}\left\{p_l^* e^{-j\hat{\gamma}_l^{(i)}} D\right\} > 0$

Then next l

Else $\hat{\gamma}_l^{(i)} = \hat{\gamma}_l^{(i)} + \pi$ Next l

Step 3: Update the p_m's

$p_m = p_m e^{j\hat{\gamma}_m^{(i)}}$ for $m = 1, 2, \ldots, M$

If $|\hat{\gamma}_m^{(i)} - \hat{\gamma}_m^{(i-1)}| < \epsilon \ \forall m = 1, 2, \ldots, M$

Then Stop

Else Go to Step 1.

One problem encountered with this technique is its slow convergence. This is due to the fact that the phases are updated one at a time and not as a vector. Although the computation time involved for implementing this technique is not very large, it would be desirable to find a more efficient gain maximization scheme. The following subsection describes such a scheme.

7.3.2 Direct method for gain maximization

This method replaces the vector $\mathbf{p}$ by a vector $\tilde{\mathbf{p}}$ which is assumed to have arbitrary amplitude and phase distribution and seeks the value of $\tilde{\mathbf{p}}$ which maximizes G. Once the maximizing vector is found, its phase distribution is used to determine the phase distribution for the vector $\mathbf{p}$ as illustrated below.

This technique starts by expressing G as a function of $\tilde{\mathbf{p}}$ as follows:

$$G = \frac{\tilde{\mathbf{p}}^{*t}\tilde{\mathbf{p}}}{\tilde{\mathbf{p}}^{*t}(\mathbf{H}\mathbf{H}^{*t})^{-1}\tilde{\mathbf{p}}}. \tag{7.8}$$

Rearranging this equation and taking the derivative of G with respect to $\tilde{\mathbf{p}}$, one

obtains

$$\tilde{\mathbf{p}}^{*t}(\mathbf{H}\mathbf{H}^{*t})^{-1}G + \tilde{\mathbf{p}}^{*t}(\mathbf{H}\mathbf{H}^{*t})^{-1}\tilde{\mathbf{p}}\frac{\partial G}{\partial \tilde{\mathbf{p}}} = \tilde{\mathbf{p}}^{*t}. \tag{7.9}$$

Setting the derivative to zero and taking the conjugate of the equation yields

$$(\mathbf{H}\mathbf{H}^{*t})\tilde{\mathbf{p}} = G\tilde{\mathbf{p}}. \tag{7.10}$$

This is an eigenvalue problem, the solution of which is the eigenvector corresponding to the largest eigenvalue of the matrix $(\mathbf{H}\mathbf{H}^{*t})$ [15].

The amplitude distribution of the vector $\tilde{\mathbf{p}}$ does not correspond to the specified pressure amplitudes at the control points. However, it is possible to achieve increased intensity gain by choosing the elements of the vector $\mathbf{p}$ such that

$$p_i = |p_i|e^{j\arg(\tilde{p}_i)} \quad \text{for } i = 1, 2, \ldots, M \tag{7.11}$$

where the $|p_i|$'s are the specified amplitudes of complex pressures at the control points. This technique provides a fast direct means of maximizing the intensity gain. Although this method yields a suboptimal solution, it proved useful in producing dramatic reductions in the interference patterns associated with several useful multiple-focus patterns. Furthermore, the iterative gain maximization algorithm described in the previous section often converges to the phase distribution obtained by this direct approach.

To demonstrate the effect of the direct gain maximization method described in this section, it will be applied to the field patterns shown in Figure 6.5 (three-focus pattern) and Figure 6.7 (annular ring pattern). Using a 12×10 CSA2D, a three-focus pattern was synthesized by focusing the array at three points symmetrically distributed along a vertical line at a depth of 140 mm and 15 mm off-axis distance. The control points were placed at $z = -10, 0, 10$ with equal relative intensity. This case is equivalent to the case shown in Figure 6.5. The phases at the control points were determined using the gain maximization algorithm. Using these phases, the

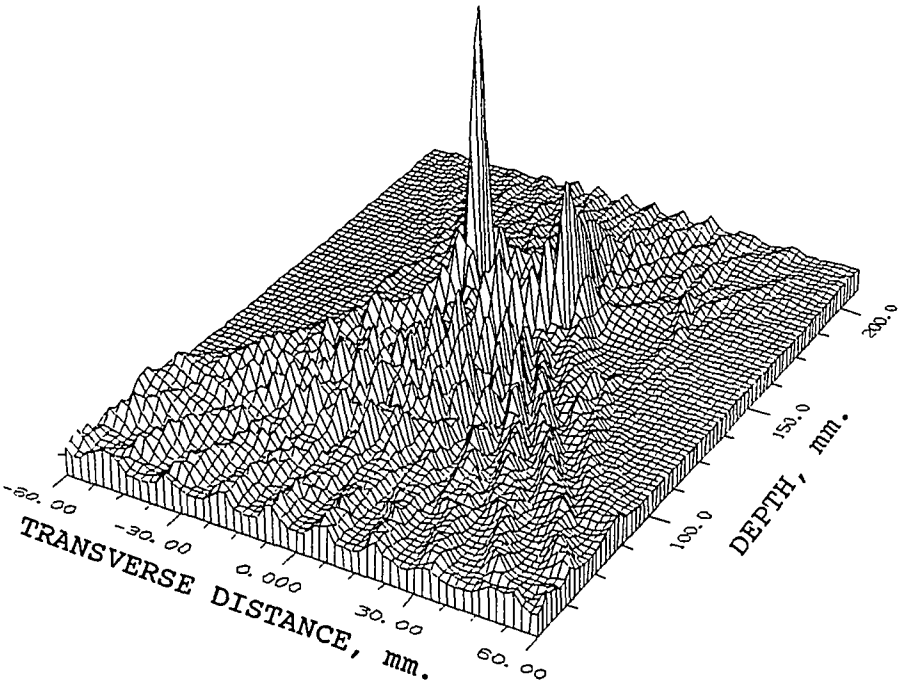

a) $z = 0$ plane.

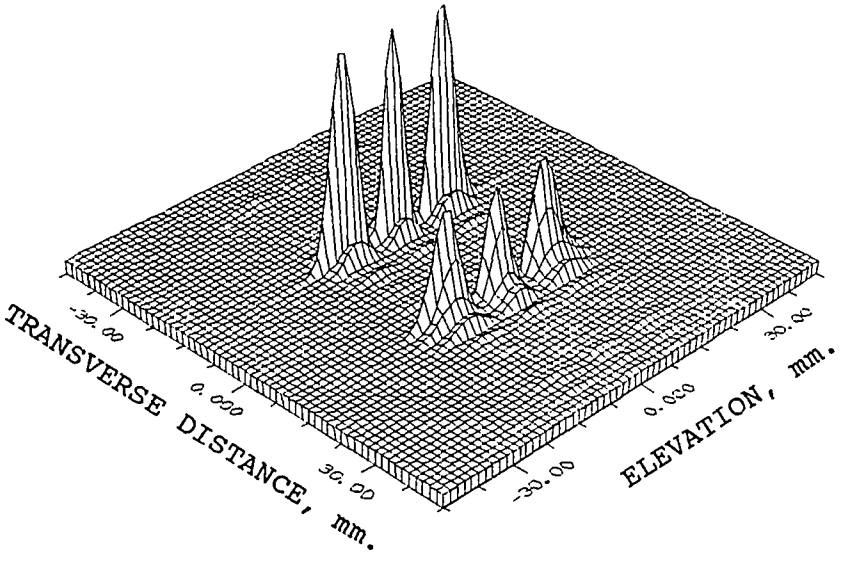

b) Focal plane.

Figure 7.5. Intensity profiles of a three-focus field pattern produced by the CSA2D using the pseudoinverse method with gain maximization.

three-focus pattern shown in Figure 7.5 resulted. The field pattern obtained with gain maximization is different from the unoptimized case in two ways. First, the three foci are more distinctly separated from each other in the optimized case. Secondly, and more importantly, a dramatic decrease in the interference pattern in the $z = 0$ plane occurred. As will be shown in Chapter 8, this reduction in the interference pattern will have a profound effect on the scanned field pattern. In fact, the field pattern shown in Figure 6.5 will be shown to fail in inducing localized heating for a simple scan path. The optimized three-focus pattern successfully generates localized heating when used to scan the same path.

The removal of the interference pattern achieved by the gain maximization algorithm is not a special case. In fact, it is the rule rather than the exception. This should not be very surprising if one considers the physical significance of the intensity gain. This quantity represents the ratio of the effective cross section of the wavefront at the surface of the array to the effective cross section of the wavefront in the focal plane. Since the effective cross section of the wavefront in the focal plane is fixed by the selection of the control points, the gain maximization amounts to maximizing the effective cross section of the wavefront at the surface of the array. The fact that the wavefront converges to the focal plane from a larger cross section minimizes the chances of interference between the different components of the wavefront as they approach the focal plane. The following example also shows that the gain maximization method significantly reduces the interference patterns associated with annular-ring patterns.

The SSA was used to directly synthesize an annular ring with 30 mm diameter parallel to the aperture of the array at a depth of 100 mm with its axis coinciding with the central axis of the array. A total of 28 control points were uniformly distributed around the ring with equal pressure magnitude assigned to each point. The phases of the complex pressure at the control points were determined by the

gain maximization algorithm. This case is equivalent to the case shown in Figure 6.7. Figure 7.6 shows the intensity profiles of the annular ring field pattern synthesized using the pseudoinverse method with the gain maximization algorithm. Comparing this field pattern to Figure 6.7 clearly shows that the gain maximization algorithm removes the axial interference pattern prior to and beyond the focal plane. Examining the focal pattern of the annular ring shows that a distinct focal spot now appears for every focal point. This is due to the fact that the pressures at the control points are no longer in phase with each other and the pressure field switches its polarity between consecutive control points which produces zeros in the field. This is also an indication of the higher divergence of the wavefront outside the focal plane which explains the disappearance of any high intensity interference patterns from the synthesized field.

The significance of the gain maximization technique becomes even more remarkable when it is compared with the phase rotation technique described in Section 6.5. The annular ring pattern described above was synthesized using the pseudoinverse method with the phases of complex pressures at the control points set according to Equation (6.41) with $m = 4$ and $M = 28$. Figure 7.7 shows the resulting intensity profiles. As indicated in the previous chapter, the phase rotation technique results in removing the axial interference patterns beyond the focal plane. However, the result still shows high-intensity interference prior to the focal plane. This result is typical of what can be obtained using the phase rotation index. In general, one cannot "choose" a specific value of the phase rotation index that will result in "optimum" intensity gain or minimize the interference pattern prior to the focal plane.

Finally, it is instructive to examine the phase distribution of the complex pressures at the control points which is chosen by the gain maximization technique. Figure 7.8 shows the phase distribution determined by the gain maximization technique at 28 control points (indexed 1 to 29) uniformly distributed around a 30 mm annular ring. A close examination of this seemingly random phase distribution reveals an

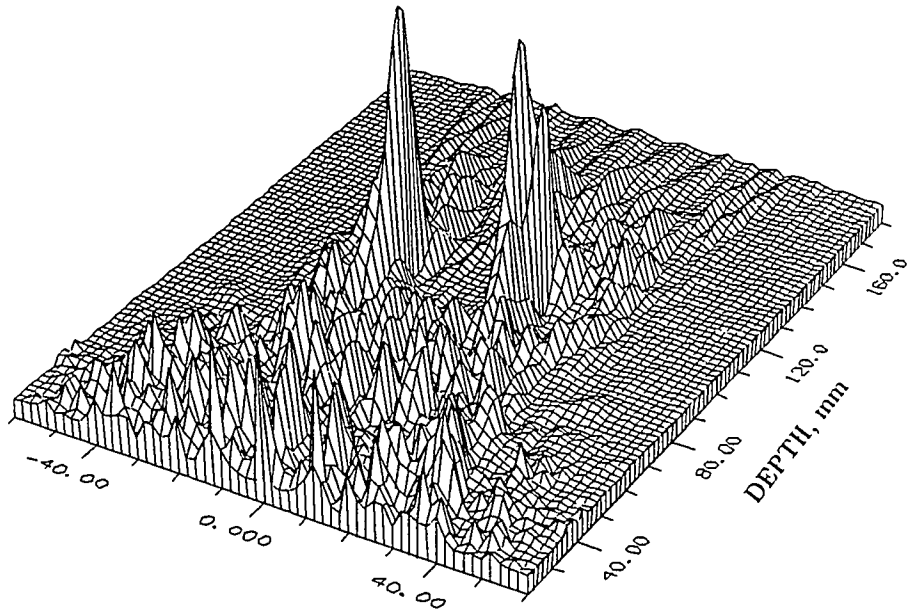

a) $z = 0$ plane.

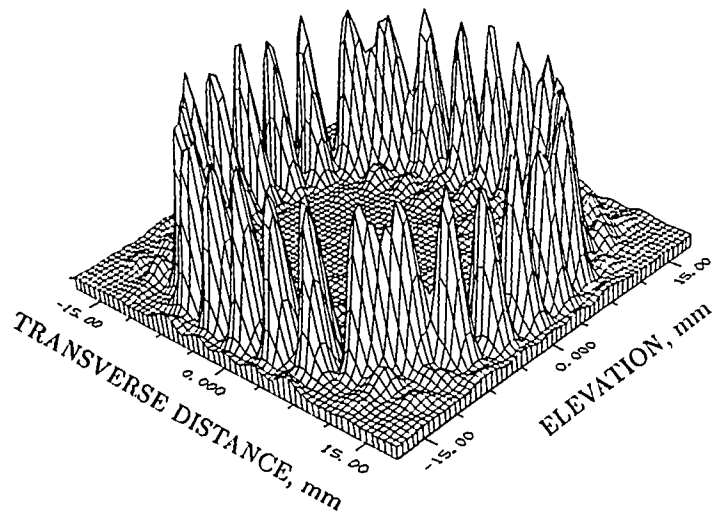

b) Focal plane.

Figure 7.6. Intensity profiles of an annular ring pattern produced by the SSA using the pseudoinverse method with gain maximization method.

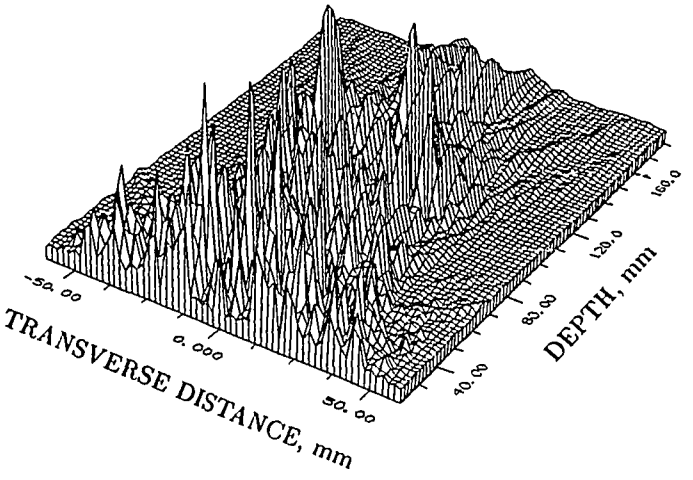

a) $z = 0$ plane.

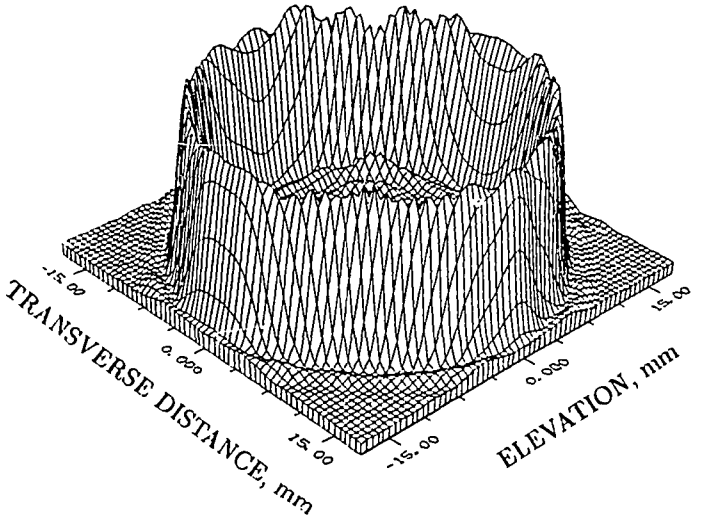

b) Focal plane.

Figure 7.7: Intensity profiles of a directly synthesized annular ring using the pseudoinverse method with phase rotation technique with $m = 4$ and $M = 28$.

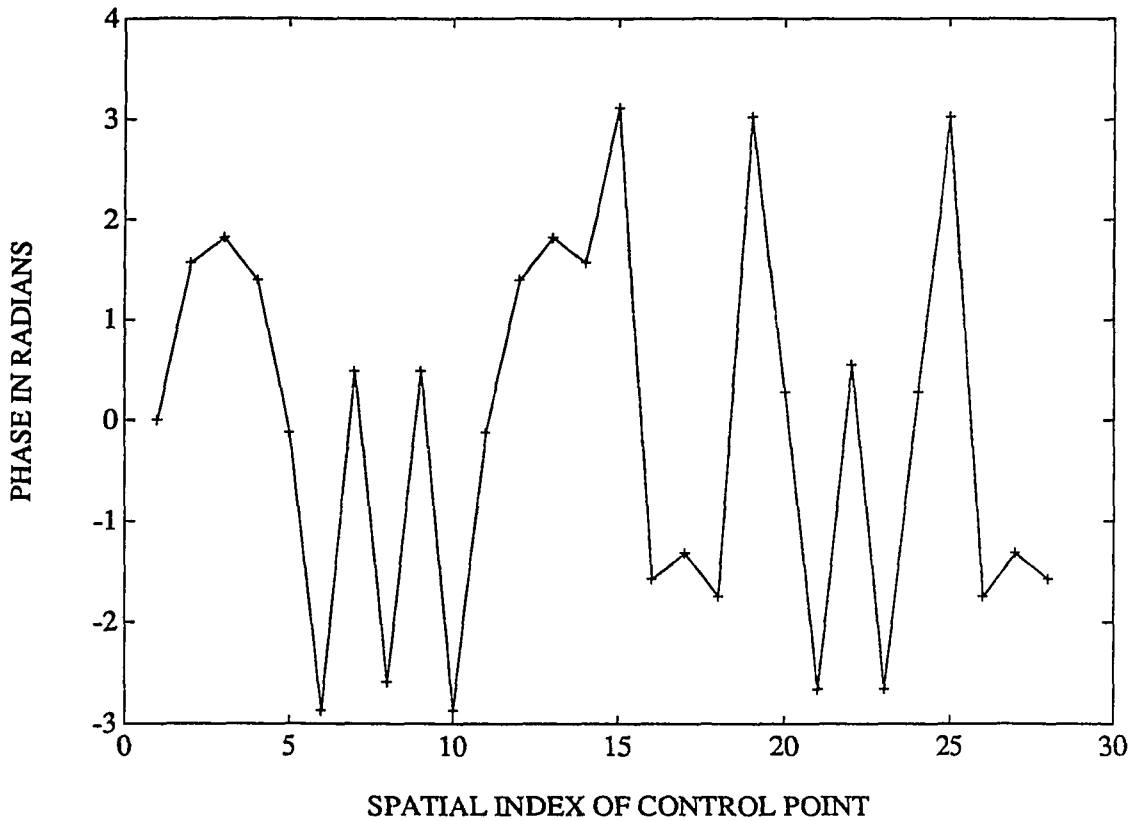

Figure 7.8. Phase distribution of complex pressures at 28 control point on a 30 mm diameter annular ring as determined by the gain maximization technique.

interesting property. Any two points that are π radians apart spatially (opposing points on a ring, e.g., points 1 and 15) have complex pressures that differ in phase by $\pm\pi$ radians. This phase difference is shown in Figure 7.9 where the abscissa represents the spatial indices of the first 14 points only (the phase difference shown at every point is that between the complex pressure at that point and the opposing one on the ring). This phase distribution guarantees the removal of the axial interference pattern.

7.4 Optimal Placement of Control Points

The definition of the pseudoinverse operator given in the previous chapter is based on an integral operator of the form given in Equation (6.7). This equation is known as a Fredholm integral equation of the first kind [76]; it is known to be ill-posed in the sense that small changes in the observation vector result in large changes in the solution. However, for the purposes of this thesis, the discretized form of this equation for the minimum-norm case (number of control points is less than the elements of the array), results in a matrix operator that is generally well-conditioned. This is true for cases when the control points are arbitrarily distributed in the field and sufficiently spaced apart.

Chapter 5 described the different methods of heating pattern generation. Two important methods are diffuse-focus scanning and direct synthesis of heating patterns. In both of these methods, the synthesized field pattern is generated by the selection of the set of control points along a specified trajectory, e.g., annular ring or line. In such cases, an important question arises; given the location and the dimensions of a focal pattern to be synthesized, what is the optimal number and locations of control points along the specified trajectory that will result in a well-conditioned propagation operator that results in the desired field pattern?

To attempt to answer this question, one would need a definition of the "condition" of a matrix operator which takes the following form:

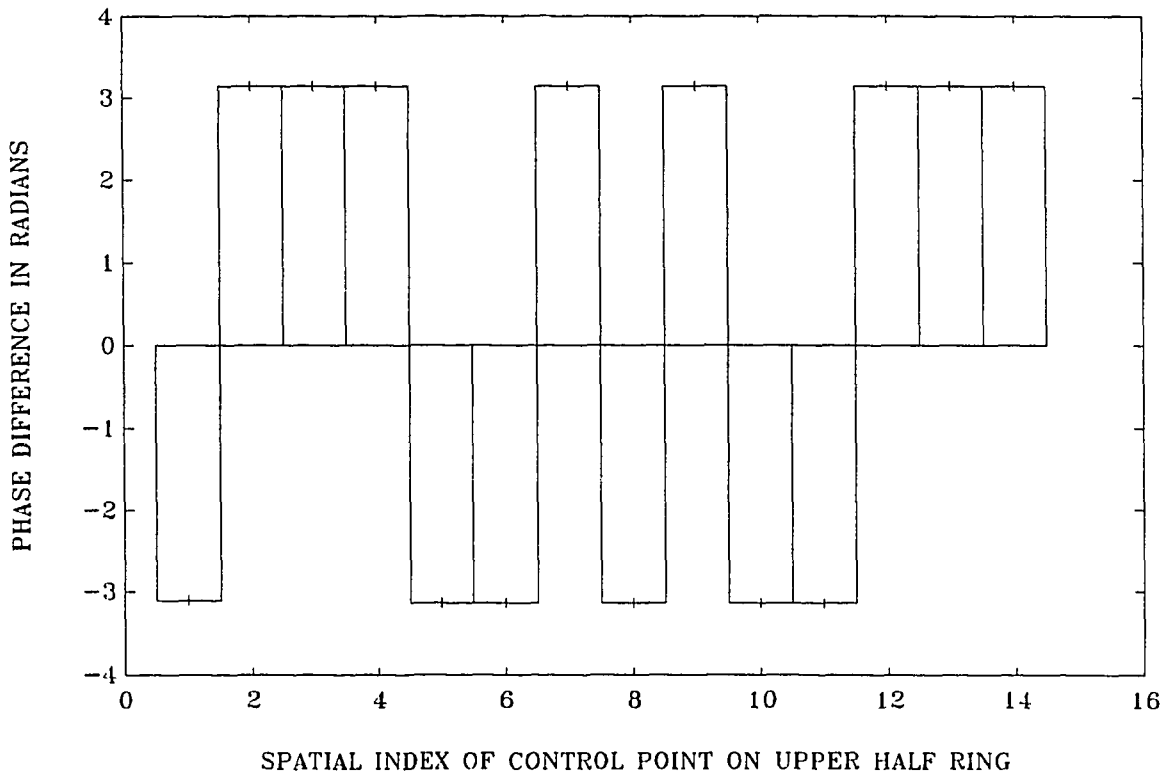

Figure 7.9. Phase differences between opposing points on the annular ring.

Definition 1 *A matrix* $\mathbf{H}$ *is said to be* **ill-conditioned** *if relatively small changes in the entries of* $\mathbf{H}$ *can cause relatively large changes in the solutions to* $\mathbf{Hu} = \mathbf{p}$. *A matrix* $\mathbf{H}$ *is said to be* **well-conditioned** *if relatively small changes in the entries of* $\mathbf{H}$ *result in relatively small changes in the solutions to* $\mathbf{Hu} = \mathbf{p}$.

It is important to note that if the matrix $\mathbf{H}$ is ill-conditioned, then the synthesis problem will result in large error even if the entries of $\mathbf{H}$ are represented exactly as floating-point numbers. On the other hand, a well-conditioned propagation matrix results in a robust synthesis of the desired field pattern. To be able to assess the conditioning of a propagation operator, one would need a measure which could be used to derive a bound for the relative error in the computed solution. This measure is provided by the *condition number* of $\mathbf{H}$, $cond_2(\mathbf{H})$. For $M < N$, the condition number is given by

$$cond_2(\mathbf{H}) = \frac{\sigma_1}{\sigma_m}, \tag{7.12}$$

where σ_1 and σ_m are the largest and smallest singular values of $\mathbf{H}$, respectively. The condition number, $cond_2(\mathbf{H})$, equals the product $\| \mathbf{HH}^{*t} \|^2 \| (\mathbf{HH}^{*t})^{-1} \|^2$ where the norm of the matrix $\mathbf{HH}^{*t}$ is defined by the *operator norm*

$$\| \mathbf{HH}^{*t} \|^2 = \max_{\mathbf{x} \neq \mathbf{0}} \frac{\| \mathbf{HH}^{*t}\mathbf{x} \|^2}{\| \mathbf{x} \|^2} \tag{7.13}$$

which can be shown to be equal to σ_1, the largest singular value of $\mathbf{H}$. The larger the value of $cond_2(\mathbf{H})$, the closer the matrix to being singular. If the vector $\mathbf{e_u}$ represents the error in $\mathbf{u}$ and the vector $\mathbf{e_p}$ represents the corresponding error in $\mathbf{p}$, then the relative errors are related by the following

$$\frac{\| \mathbf{e_p} \|^2}{\| \mathbf{p} \|^2} \leq cond_2(\mathbf{H}) \frac{\| \mathbf{e_u} \|^2}{\| \mathbf{u} \|^2}, \tag{7.14}$$

which suggests that the relative error in the synthesized field is directly proportional to the relative error in the excitation vector via the condition number of the propagation matrix. That is, the relative error in the excitation vector is amplified by the

condition number of the matrix, which can be extremely large if the matrix is nearly singular resulting in large errors in synthesis.

The condition number of the matrix $\mathbf{H}$ also provides valuable information on the sensitivity of the pseudoinverse solution to errors in the entries of $\mathbf{H}$. If the matrix $\mathbf{E_H}$ represents the error in the entries of $\mathbf{H}$, then the relative error in the solution to $\mathbf{Hu} = \mathbf{p}$ due to the error in the entries of $\mathbf{H}$ is bounded by

$$\frac{\| \mathbf{e_u} \|^2}{\| \mathbf{u} \|^2} \leq cond_2(\mathbf{H}) \frac{\| \mathbf{E_H} \|^2}{\| \mathbf{H} \|^2}, \tag{7.15}$$

where the matrix norms are defined similarly to Equation (7.13) above. These results demonstrate the importance of the conditioning of the matrix $\mathbf{H}$ on the synthesis process. Therefore, when one has a choice of selecting a specific arrangement of control points, the optimum arrangement is the one which results in the lowest condition number of the propagation matrix $\mathbf{H}$.

The choice of the number of control points and the spacing between them is explained by the following two examples. First, consider the annular ring pattern described above. For a fixed radius of the focal ring, the number of control points on the ring was incremented from 12 points in steps of 4. The condition number of the propagation matrix was recorded for each case. Figure 7.10 shows the behavior of the condition number as a function of the number of control points. The figure shows a sharp increase of the condition number when the number of control points is increased beyond 32. When the same experiment was repeated for a ring of 10 mm diameter, the condition number exhibited this sharp increase for numbers of control points larger than 40. This result is shown in Figure 7.11.

From the results shown in Figures 7.10 and 7.11, one might be tempted to relate the sharp increase in the condition number to the increase in the number of control points. It turns out that the number of control points is not responsible, by itself, for this sharp increase in the condition number. Rather, it is the spacing between the control points that causes this behavior. To show this, the condition number was

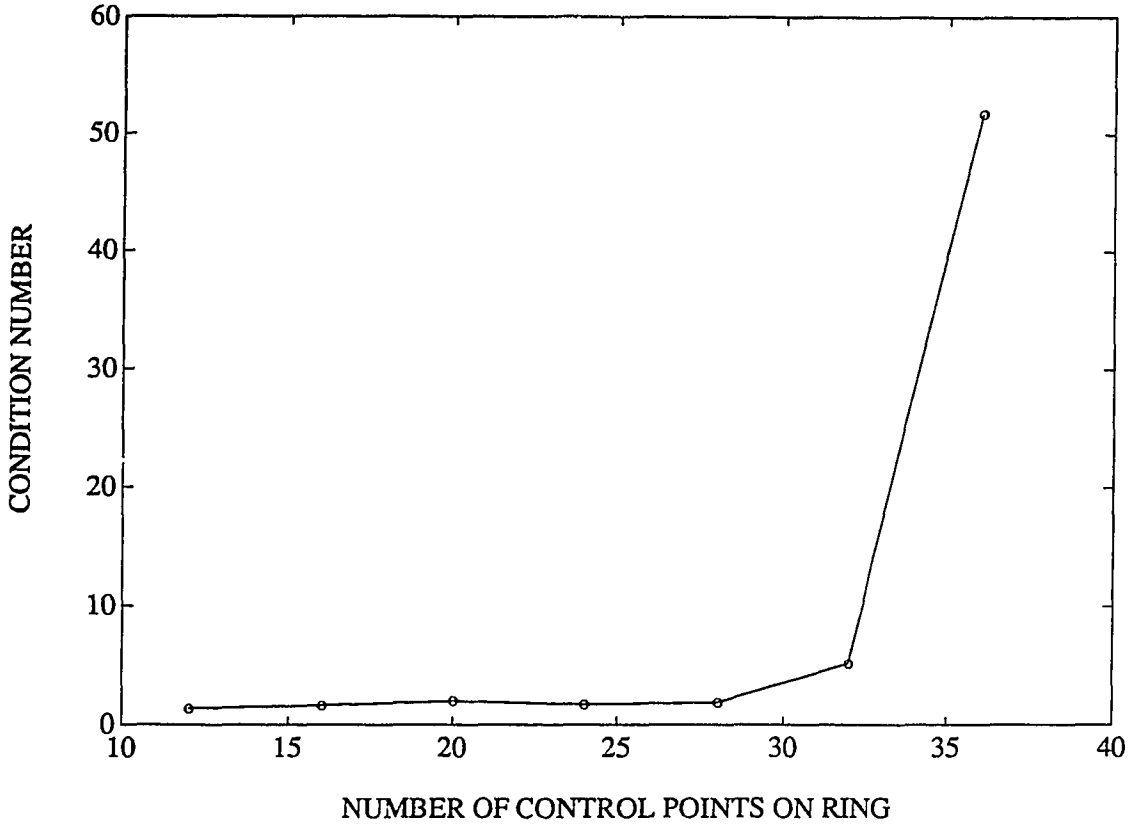

Figure 7.10. Condition number of propagation matrix vs. number of control points on a 30 mm diameter ring.

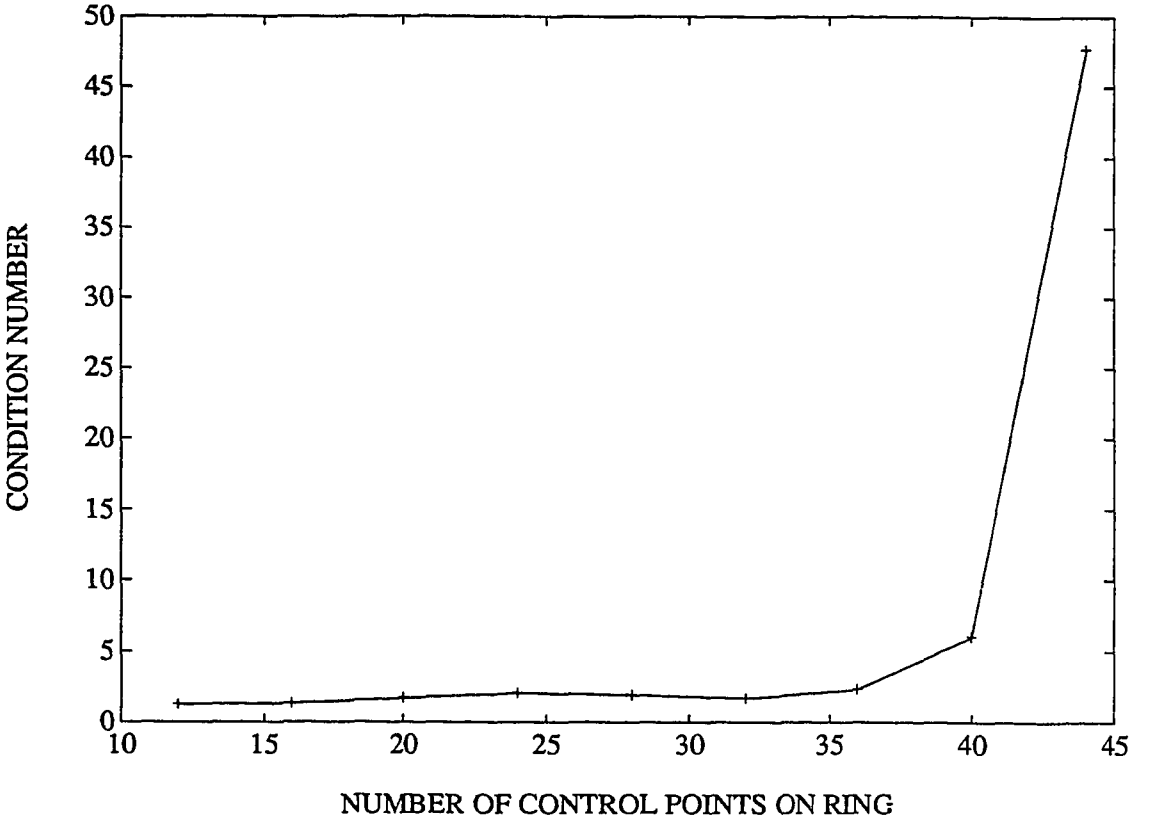

Figure 7.11: Condition number of propagation matrix vs. number of control points on a 40 mm diameter annular ring.

plotted against the spacing between the control points for the two cases discussed above. The results are shown in Figure 7.12. The figure shows that the two curves are almost identical when plotted against the spacing between control points.

The results shown in Figure 7.12 suggest that the ill-conditioned nature of the propagation matrix starts to appear as the spacing between the control points approaches 3 mm. This spacing corresponds to the width of the focal spot produced by the SSA. To see if this is the parameter that is causing the propagation matrix to become singular, the condition number of the propagation matrix associated with the diffuse focus pattern shown in Figure 6.5 was examined. The number of control points along the vertical line from $z = -10$ to $z = 10$ was incremented from 5 in steps of 2. Figure 7.13 shows a plot of the condition number against the spacing between the control points along the line. This case shows that the matrix approaches singularity as the spacing between control points approaches 5 mm which corresponds to the height of the focal beam for a single focus. In general, the propagation matrix becomes ill-conditioned when the spacing between the control points in any direction is comparable to the dimension of the focal beam in that direction.

7.5 Effect of Quantization

Usually the elements of the excitation vector, $\mathbf{u}$, are obtained theoretically assuming infinite precision representation. For practical realization, however, the elements of $\mathbf{u}$ must be quantized to a fixed number of bits. As a consequence, the realized field pattern differs from the ideal one which would have been obtained if the elements of $\mathbf{u}$ were realized with infinite precision. This adds another source of error to the synthesis process. The error bounds for the reconstructed field can be obtained using Equation (7.14) from the previous section. This section, however, aims at providing some examples to identify conditions under which error due to quantization can be significant. An iterative method for the reduction of error due to quantization is also given.

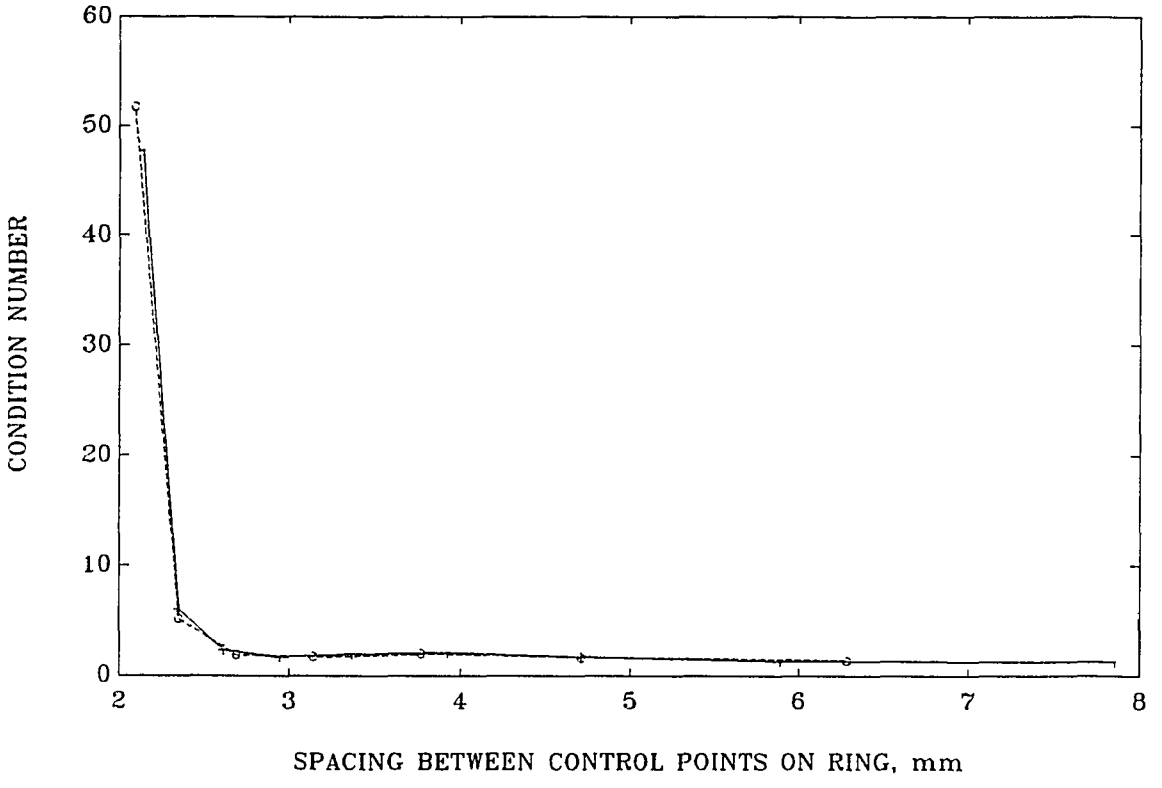

Figure 7.12: The results of Figures 7.10 and 7.11 plotted against the spacing between control points.

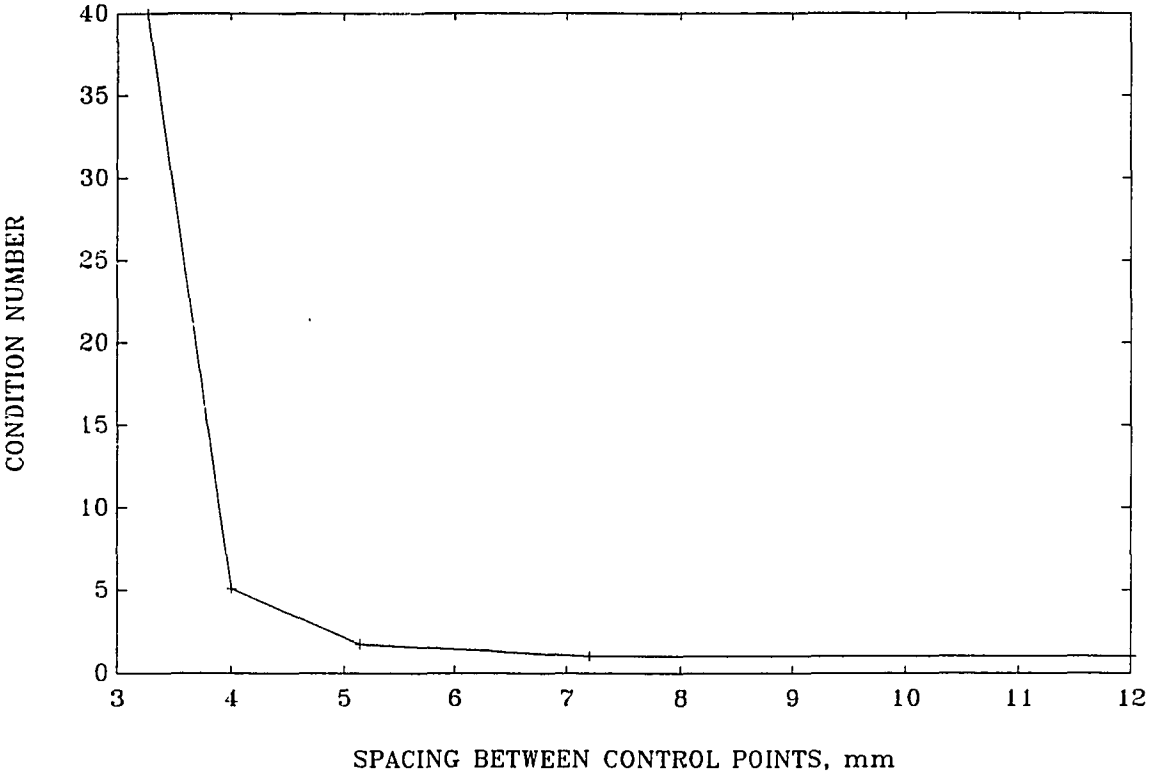

Figure 7.13: The condition number of a propagation matrix responsible for generating a diffuse focus against the number of control points.

The driver circuit to the array elements is assumed to be capable of independently setting the amplitude and phase of the excitation signal at each element. The digital driver circuit is assumed to generate a periodic rectangular pulse of the form

$$f(t) = \begin{cases} A & t - \phi \leq |\tau|, \\ 0 & |\tau| \leq t - \phi \leq T; \end{cases} \tag{7.16}$$

and

$$f(t+T) = f(t), \tag{7.17}$$

where T is the period of the pulse, ϕ represents a time (phase) shift, and $\left\{\frac{\tau}{T}\right\}$ is the duty cycle. A matching circuit which passes only the fundamental component of this signal to the piezoelectric elementis assumed to be used. From the Fourier series representation of $f(t)$, the Fourier coefficient of the fundamental frequency of this signal is given by

$$a_1 = \left(\frac{A}{\pi}\right) e^{-j\frac{2\pi\phi}{T}} \sin\left(\frac{\pi\tau}{T}\right) \tag{7.18}$$

which defines the amplitude, $\left(\frac{A}{\pi}\right)\sin\left(\frac{\pi\tau}{T}\right)$, and phase, $\frac{2\pi\phi}{T}$, of the driving signal to the transducer element.

Quantization allows τ and ϕ to assume a finite number of discrete values determined by the number of bits supported by the digital controller. The digital controller used to drive the array is assumed to provide 3-bit amplitude quantization and 4-bit phase quantization. Consequently, the phase shift can assume the values determined by

$$\phi_n = n\frac{T}{2^4}; \quad \text{for } n = 0, 1, \ldots, 2^4 - 1. \tag{7.19}$$

The duty cycle can take values determined by

$$\begin{aligned} \left\{\frac{\tau}{T}\right\}_n &= \frac{1}{\pi}\sin^{-1}\left(\frac{\pi|a_1|}{A}\right) \\ &= n\frac{T}{2^4}; \quad \text{for } n = 1, 2, \ldots, 2^3 - 1. \end{aligned} \tag{7.20}$$

The latter equation implies that the maximum duty cycle allowed is 0.5 (50 %). The quantized phase, ϕ_q is obtained from its continuous value, ϕ, according to the

following rule:

$$\phi_q = \phi_n; \quad \text{for } \phi_n \leq \phi + \frac{\Delta\phi}{2} \leq \phi_{n+1}, \tag{7.21}$$

where $\Delta\phi = \frac{2\pi}{2^4}$ is the phase quantization step. The quantization rule given herein is nothing more than a rounding operator. Similarly, the quantized duty cycle, $\left\{\frac{\tau}{T}\right\}_q$, is obtained from its continuous value, $\left\{\frac{\tau}{T}\right\}$, according to the following rule:

$$\left\{\frac{\tau}{T}\right\}_q = \left\{\frac{\tau}{T}\right\}_n; \quad \text{for } \left\{\frac{\tau}{T}\right\}_n \leq \left\{\frac{\tau}{T}\right\} + \frac{\Delta\tau}{2} \leq \left\{\frac{\tau}{T}\right\}_{n+1}, \tag{7.22}$$

where $\Delta\tau = \frac{T}{2^4}$ is the duty cycle quantization step.

The phase and amplitude quantization levels given above were determined to be sufficient for the accurate generation of single-focus field patterns. Independent simulations and experimental data obtained with an existing phase and amplitude controller (with the same quantization levels) support this claim. However, when synthesized multiple-focus patterns are generated with the quantized phase and amplitude levels given above, one needs to examine the effect of quantization on the "quality" of the resulting pattern. The "quality" of the resulting pattern is determined based on a "measure" of the error between the reconstructed pattern and the ideal pattern which would be obtained assuming infinite precision phase and amplitude control.

To demonstrate the effect of quantization on the synthesis process, consider the four-focus pattern given in Figure 6.1. Figure 7.14 shows the intensity profiles of the ideally reconstructed pattern (solid line) and the quantized pattern (dashed line). (The term quantized pattern means the reconstructed field pattern with quantized excitation vector.) One can make two observations from examining the quantized pattern. The first is that the four focal points are still clearly identifiable in the reconstructed field and they occur at their original positions. This is generally true for multiple-focus field patterns, i.e., the error due to quantization is not likely to result in total loss of the synthesized pattern. The second observation is that there

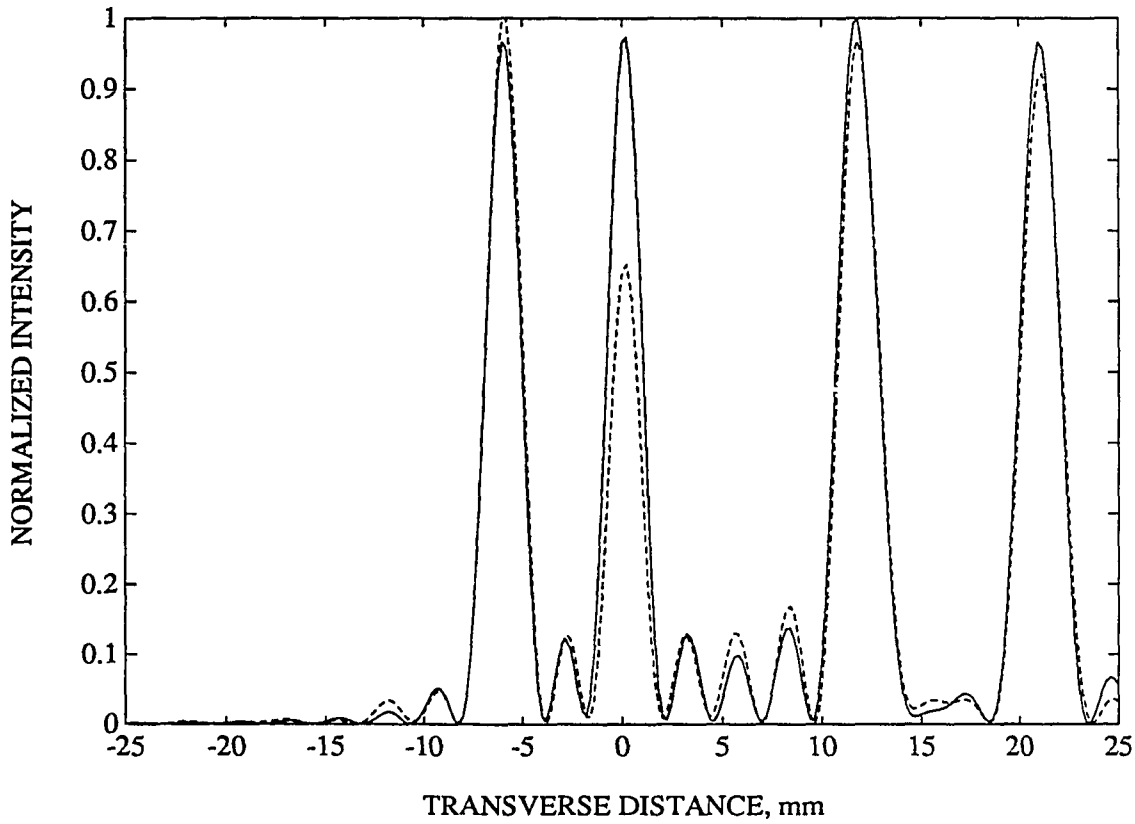

Figure 7.14. Intensity profiles of the ideally reconstructed four-focus field pattern (solid line) and the reconstructed field pattern with quantized excitation vector (dashed line).

is some directionality associated with the resulting error; one can see clearly that the focus at $x = 0$ suffers the most from quantization. This also indicates a general trend in the effect of quantization errors on the reconstructed fields. The maximum error in the reconstructed field can be expected to occur at those control points where the array has maximum directivity. To illustrate this, let the quantized excitation vector be

$$\mathbf{u}_q = \mathbf{u} + \mathbf{e}_\mathbf{u}, \tag{7.23}$$

where $\mathbf{u}$ is the unquantized excitation vector and $\mathbf{e}_\mathbf{u}$ is the error due to quantization. The resulting error in the reconstructed field can be given by

$$\mathbf{e}_\mathbf{p} = \mathbf{H}\mathbf{e}_\mathbf{u}. \tag{7.24}$$

The error at the ith control point can be expressed explicitly in terms of the rows of the propagation matrix as follows:

$$e_{pi} = \mathbf{h}_i \mathbf{e}_\mathbf{u}, \tag{7.25}$$

where $\mathbf{h}_i$ is the ith row of the matrix $\mathbf{H}$. Using the Cauchy-Schwartz inequality, the upper bound of this error can be given by

$$\max |e_{pi}|^2 = \| \mathbf{h}_i \|^2 \| \mathbf{e}_\mathbf{u} \|^2 . \tag{7.26}$$

Recognizing that $\| \mathbf{h}_i \|^2$ is nothing more than the directivity of the array at the ith control point, one can see that the maximum error in the reconstructed field is likely to occur at points where the directivity of the array is maximum. This maximum error occurs when $\mathbf{h}_i^{*t} = \gamma \mathbf{e}_\mathbf{u}$ where γ is a real constant, i.e., the $\mathbf{e}_\mathbf{u}$ is in phase with $\mathbf{h}_i^{*t}$. On the other hand, the error will be zero when $\mathbf{h}_i^{*t}$ and $\mathbf{e}_\mathbf{u}$ are orthogonal.

The above discussion gives the value of the maximum possible error in the reconstructed field at any one of the control points. Therefore, by the mere selection of the control points (and consequently forming the operator $\mathbf{H}$), one can identify

the control points where this error is likely to be maximum. However, the actual error distribution varies randomly from one pattern to another. More precisely, it varies from one excitation vector to another. Figure 7.15 shows the quantized field patterns in the focal plane corresponding to those given in Figure 7.6a (28 control points around a 30 mm diameter annular ring with gain maximization) and Figure 7.7a (same as Figure 7.6a but obtained with the phase rotation method with $m = 4$). One can see from these results that the first observation made above is still true.

To minimize the error in the reconstructed field due to quantization, the following simple algorithm was implemented based on the conjugate gradient, CG, algorithm given in Section 6.4.

Step 0: Find $\mathbf{u}_o$. The infinite precision excitation vector.

Step 1: For $i = 1, 2, \ldots$ iterate.

Find $\mathbf{u}_q = Q[\mathbf{u}_{i-1}]$. The quantized excitation vector.

If $\| \mathbf{e_p} \|^2 \leq \epsilon$ Go to Step 3.

Step 2: Use CG algorithm with $\mathbf{u}_0 = \mathbf{u}_q$ to find new infinite precision vector $\mathbf{u}_i$.

Go to Step 1

Step 3: Excitation vector $\mathbf{u} = \mathbf{u}_i$.

In the above algorithm, $Q[\cdot]$ denotes quantization, and $\mathbf{e_p}$ is as in Equation (7.17) above. Applying this algorithm to the four-focus field pattern shown in Figure 7.14 resulted in the field pattern given in Figure 7.16. This result shows that a reduction in error due to quantization is possible using this algorithm.

Finally, the fact that the error in the reconstructed field has a directivity suggests that more than one error measure be used in examining the effect of quantization. The L_2 norm of the vector $\mathbf{e_p}$, $\sqrt{\| \mathbf{e_p} \|^2}$, gives a measure of the square error in the

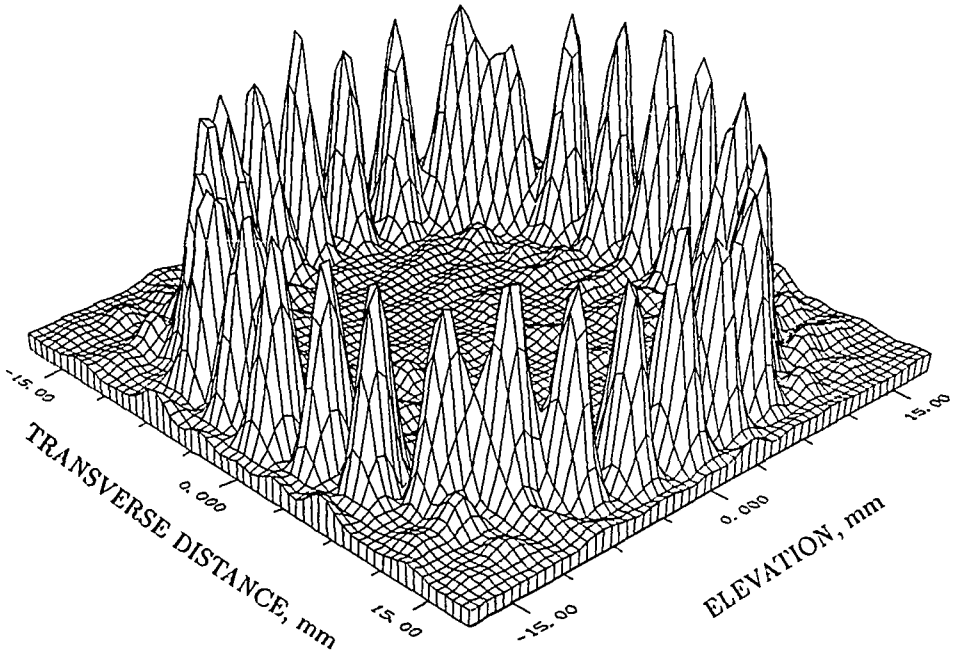

a) Quantized annular ring pattern (Gain maximization).

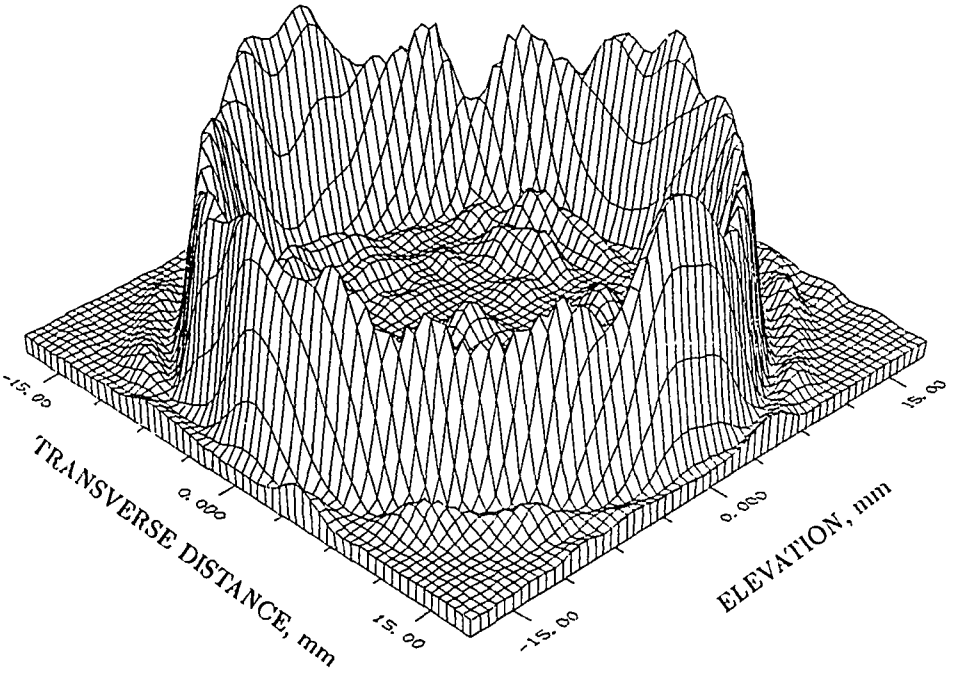

b) Quantized annular ring pattern (Phase rotation with $m = 4$).

Figure 7.15. Quantized annular ring patterns.

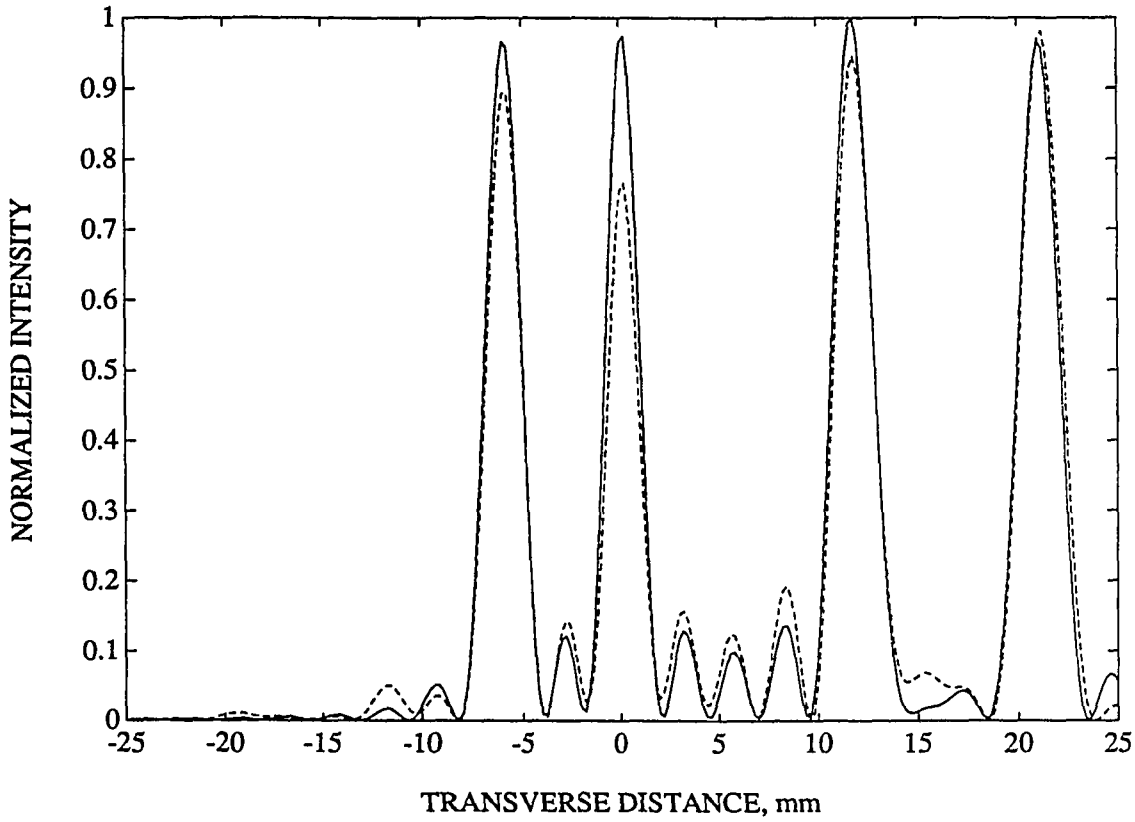

Figure 7.16. Intensity profiles of the ideally reconstructed four-focus field pattern (solid line) and the reconstructed field pattern with quantized excitation vector with reduced quantization error (dashed line).

reconstructed field. The L_p norm of $\mathbf{e_p}$, defined as

$$\| \mathbf{e_p} \|_p = \left(\sum_{i=1}^{M} e_{pi}^p \right)^{1/p}, \tag{7.27}$$

gives a measure of the absolute maximum error in the reconstructed field (when $p \rightarrow \infty$). An optimal quantization scheme can be designed to minimize both of these measures simultaneously. This would result in minimizing the square error while maintaining the uniformity of error distribution over all the control points. The effect of quantization is analyzed in more detail in [28].

CHAPTER 8

EXAMPLES OF HEATING PATTERNS

8.1 General

This chapter discusses examples of simulated phased-array heating patterns as described in Chapter 5. Rather than giving an exhaustive list of examples for the different combinations of applicator geometries and heating pattern generation methods, this chapter aims at defining the heating pattern generation as a design problem. Towards this objective, the various steps for choosing driving signal distributions based on the specified tumor size and geometry are highlighted. This is followed by the definition of a set of *performance criteria* or *figures of merit* for heating patterns for the evaluation of their heating efficacy. Section 8.2 describes the parameters used simulating both acoustic wave propagation and thermal response to power deposition patterns. Section 8.3 discusses energy considerations which guide the choice of a specific heating pattern generation method. This is followed by Section 8.4 which defines some figures of merit for the evaluation of the heating efficacy of power deposition patterns. Sections 8.5 and 8.6 discuss specific heating pattern generation methods.

The example discussed in Section 8.5 of this chapter is chosen to illustrate the use of multiple-focus scanning as an alternative for single-focus scanning. The multiple-focus scanning is performed using multiple-focus beams obtained both with and

without the gain maximization technique described in Chapter 7. The results indicate that gain maximization plays a vital role in inducing localized heating when multiple-focus scanning is used. Section 8.6 discusses the direct synthesis of annular ring heating patterns.

8.2 Model Parameters

The propagation model used in this chapter and throughout this thesis is assumed to be homogeneous and lossy. The speed of sound is assumed to be 1500 m/s and the density is assumed to be 1000 kg/m^3. The attenuation coefficient, a, was taken to be 0.01 neper/mm at 1 MHz. The frequency dependence of the attenuation coefficient was assumed to follow the power law

$$a = a_o\,(f)^{\gamma}, \tag{8.1}$$

where a_o is the attenuation coefficient at 1 MHz, f is the frequency in MHz, and γ is a constant. The value of γ used in the simulations was taken to be 1.1 [11]. All the simulations were performed at an operation frequency of 500 kHz.

The thermal model described in Chapter 3 is used throughout this chapter. The blood perfusion is assumed to be uniform throughout the treatment volume (including the tumor). The tumor tissues are assumed to be the same as normal tissues both for acoustic wave propagaion and thermal conduction. The rest of the model parameters are shown in Figure 3.2 (the thermal conductivity, K, is given in SI units). The boundary conditions are such that the skin temperature is kept constant at 25^oC and the walls of the treatment volume are at the body temperature of 37^oC. The absorption coefficient was assumed to be equal to the attenuation coefficient. This thermal model is adapted from one used in [26].

8.3 Energy Requirements

Simple design formulae have been derived for computing the power dissipation inside a spherical tumor volume which would raise its temperature to a specified

level both under transient and steady-state conditions [4]. For example, the power required to sustain T_h $^\circ C$ of hyperthermia inside a spherical tumor of radius r_t can be estimated by

$$P_t = 4\pi r_t \; T_h K, \tag{8.2}$$

where K is the thermal conductivity of the tissue. Of course, the power deposition inside the tumor is concentrated around a finite number of points in the tumor volume (the focal points along the scan path or the control points in a directly synthesized pattern). For clarity, the following discussion will assume that the selected points inside the tumor correspond to the focal points along the scan trajectory.

The total power in the tumor can be approximated by

$$P_t = \sum_{i=1}^{N_f} Q_i V_i, \tag{8.3}$$

where Q_i is the power deposition level at the ith focal point, and V_i is the effective volume of the focal spot, and N_f is the number of focal spots along the scan trajectory. Assuming that the effective size of the focal points does not change as they traverse the scan trajectory and equal power deposition at each of these points, the power deposition at each point can be given by

$$Q_{av} = \frac{P_t}{NV}, \tag{8.4}$$

where V is the effective size of any focal point along the scan trajectory.

The pressure level at a focal point can be determined as follows:

1. The spatial-peak time-average intensity at a focal point is given by

$$I_{SPTA} = \frac{Q_{av}}{2\alpha}$$

where α is the absorption coefficient.

2. Assuming equal dwell time at each focal point, the factor $\frac{\tau}{T}$ in Equation (2.7) becomes $\frac{1}{N_f}$ where N_f is the number of focal points along the scan trajectory.

Therefore, the spatial-peak pulse-average intensity at the focal point can be given by

$$I_{SPPA} = \frac{N_f Q_{av}}{2\alpha}.$$

This quantity is very important because it determines the spatial-peak time-peak intensity level, I_{SPTP}.

3. The pressure magnitude at the focal point is given by (using Equation (2.6))

$$p = \sqrt{\frac{\rho c N_f Q_{av}}{\alpha}}.$$

This value is then used to determine the excitation vector, u, at the surface of the array corresponding to this focal point.

The above procedure can be modified to accommodate multiple-focus scanning in a straightforward manner. Assuming that a multiple-focus pattern with n_f foci is used to replace the single-focus pattern in scanning the same trajectory, the above steps can be used in the multiple-focus case in the same way by substituting $\frac{N_f}{n_f}$ for N_f in steps 1, 2, and 3 above.

8.4 Evaluation of Heating Patterns: Figures of Merit

The choice of a specific applicator or heating pattern generation method depends on such factors as availability, constraints, and efficacy for a specific tumor environment. Assuming that the therapist has a choice of different alternatives for a specific situation, it would be useful to guide his or her choice by defining some *figures of merit* for the realized heating patterns. The following parameters were identified as possibly useful performance criteria for heating pattern generation methods:

1. Power Concentration Ratio, η_Q.

This parameter expresses the ratio of the average power deposition in the tumor to the average power deposition in the treatment volume, i.e.,

$$\eta_Q = \frac{\frac{1}{V_t}\int_{V_t} Q(\mathbf{r})dV}{\frac{1}{V}\int_{V} Q(\mathbf{r})dV},$$

where V_t and V are the volumes of the tumor and the treatment regions, respectively. This parameter is defined in a similar way to the directivity function of an antenna. It reflects the ability of a heating pattern to concentrate energy in a tumor.

2. Average Power at the Surface of the Array, $\overline{P}_A$.

   This quantity is important from the engineering point of view. It determines whether or not a specific applicator is capable of providing the necessary power deposition in the tumor. It is also important if the operating efficiency of a specific applicator is taken into consideration.

3. Percentage of Tumor Volume over $43°C$, η_{43}.

   This parameter has obvious clinical value since $43°C$ is the accepted value by most clinicians as the threshold for therapeutic heating. This parameter, combined with the maximum temperature outside the tumor volume, is probably the ultimate parameter for evaluating the efficacy of a specific heating pattern.

The heating patterns discussed in the following sections will be compared based on these parameters. The value of the power concentration ratio, η_Q, as an indicator of heat localization will become apparent from the following results.

8.5 Single-Focus Scanning versus Multiple-Focus Scanning

A 12 × 10 CSA2D array with a radius of 140 mm and an angular opening of 90° was chosen to heat a 30 mm diameter spherical tumor centered at a depth of 90 mm beneath the skin. For comparison purposes, both single-focus scanning and multiple- focus scanning were used to generate the same heating pattern in the treatment region. The heating pattern was specified for conventional scanning by choosing a scan trajectory which consists of 27 points distributed over three rhombi as shown in Figure 8.1. The rhombi were positioned at $z = -10, 0$, and 10 mm with

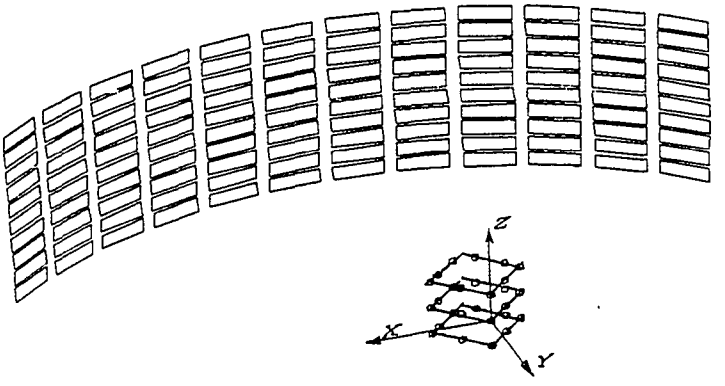

Figure 8.1. A 27-point scan trajectory consisting of 3 rhombi fitted inside a 30 mm diameter tumor.

their centers at the same vertical line passing the center of the tumor. The sides of each rhombus were 17 mm. The array was positioned such that its geometrical center coincides with the back of the tumor, i.e., the center of the tumor is 130 mm from the vertex of the array.

The blood perfusion in the treatment volume was assumed to be uniform with a value of 5 kg/m^3/sec. Experience with the *BHTE* shows that Equation (8.2) underestimates the power requirement for well-perfused tumors. Therefore, based on that equation and allowing for blood perfusion, the power dissipated within the tumor volume to sustain a $7°C$ hyperthermia was determined to be 2.5 W. Using Equation (8.4), the time-average power deposition level at each of the focal points was specified to be 0.4 W/cm^3 which requires a focal intensity $I_{SPPA} = 108$ W/cm^2 at each of the scan points specified above (the effective volume of the focal spot is nearly 200 mm^3, see Section 4.3). The single-focus field patterns needed to traverse

the scan path were synthesized using the pseudoinverse method. The average power at the surface of the array, $\overline{P}_A$ was 81 W. Figure 8.2 shows the resulting scanned field intensity profile. The maximum power deposition was 0.48 W/cm^3. The increase in power deposition in the field is due to the overlap in the intensity profiles of the different foci which always add to each other. The power concentration ratio for this pattern, η_Q is 18.1. The resulting temperature profile is shown in Figure 8.3. The percentage of the tumor over $43°C$, η_{43} is 88% with a maximum temperature equal to $46.1°C$ occurring inside the tumor. This result indicates that the single-focus scanning successfully achieves localized heating in the tumor volume. Although the $41°C$ profile can be seen to extend from the skin surface to the tumor, this is not considered to be an objectionable condition. The only potential problem with this technique is that the spatial-peak pulse-average intensity might be objectionable if it causes cavitation or intensity saturation to occur.

The three-focus field pattern shown in Figure 6.5 was designed to substitute for the single-focus scanning technique in generating the heating pattern described above. The average power available at the surface of the array necessary to produce 2.5 W inside the tumor was 73 W. The three focal points correspond to three points on the scan trajectory that lie on a vertical line shown in Figure 8.1. The maximum focal intensity needed in this case is 36 W/cm^2 which is probably safe under ordinary conditions. However, as shown in Figure 8.4, the scanned field pattern exhibits large power deposition build-up outside of the tumor which cannot be tolerated. This power deposition build-up is due to the interference pattern appearing in Figure 6.5. Figure 8.5 shows the temperature profile produced by the power deposition pattern of Figure 8.4 which shows clearly that the power deposition build-up leads to unacceptable temperature levels outside the tumor. The highest temperature outside the tumor was $44.5°C$ which occurs near the skin. The power concentration ratio, η_Q, for this pattern was 18.1 and the percentage of tumor volume over $43°C$ was 81%.

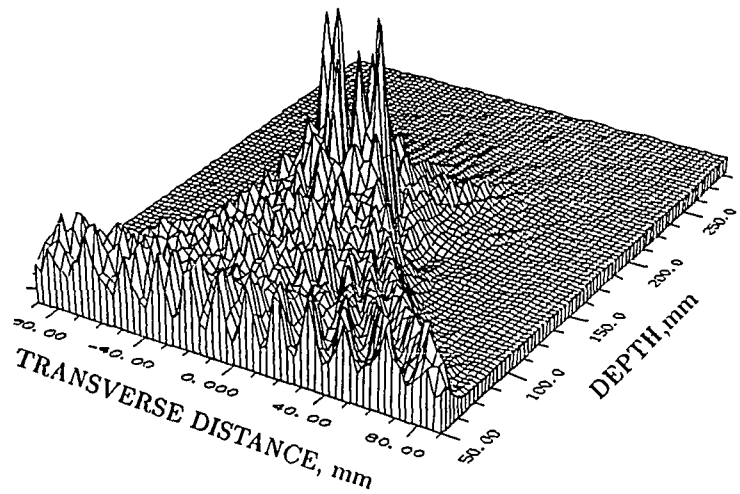

Figure 8.2. Heating pattern generated by single-focus scanning of trajectory shown in Figure 8.1.

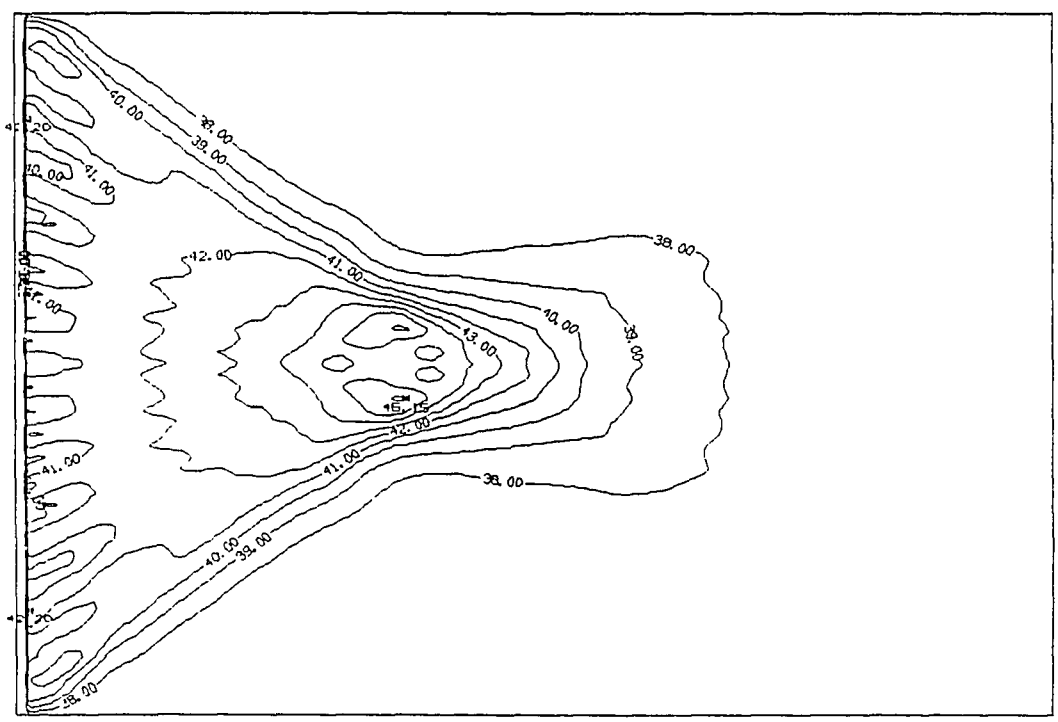

Figure 8.3. Temperature profile resulting from the heating pattern of Figure 8.2.

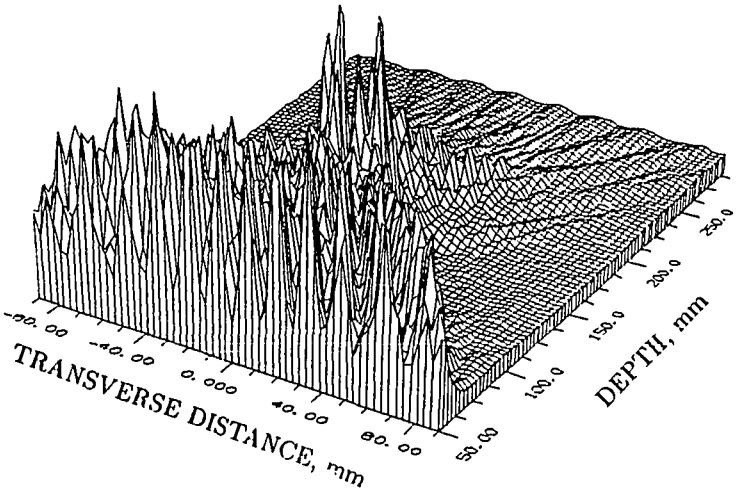

Figure 8.4. Heating pattern generated using multiple-focus scanning with the three-focus pattern shown in Figure 6.5.

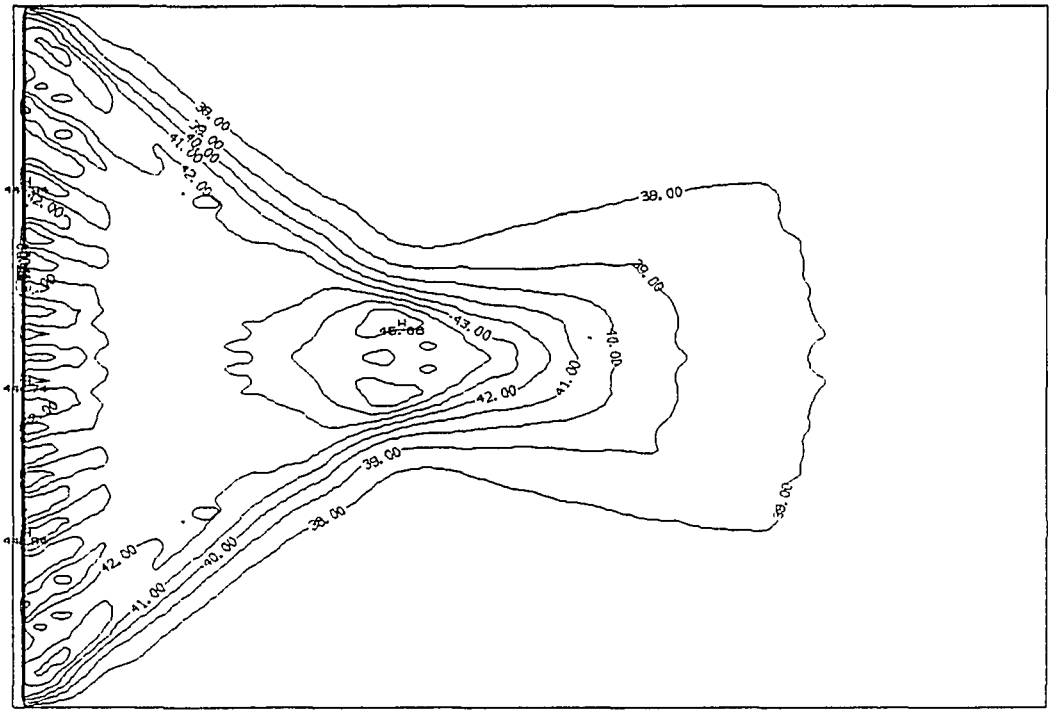

Figure 8.5. Temperature profile resulting from the heating pattern shown in Figure 8.4.

The three-focus pattern shown in Figure 6.5 fails to provide a viable alternative to single-focus scanning. Although it reduces the required focal intensity to an acceptable level, it generates unacceptably high power deposition build-up outside the tumor volume. This problem is effectively solved by using the three-focus pattern of Figure 7.5 which was obtained with the gain maximization technique. The scanned field profile resulting from scanning this three-focus pattern is shown in Figure 8.6. This power deposition pattern results in the steady-state temperature distribution shown in Figure 8.7. The average power available at the surface of the array was 86 W. The power concentration ratio was 17.6, and the percentage of tumor over $43°C$ was 87.1%. These results indicate clearly that the gain maximization technique successfully generated localized heating of the tumor. As a matter of fact, the results clearly indicate that it outperforms the single-focus scanning.

8.6 Directly Synthesized Annular Heating Patterns

Directly synthesized annular-ring patterns similar to that shown in Figure 7.6 can be very useful in heating tumors with spherical or cylindrical geometries. The gain maximization technique described in Chapter 7 allows such heating patterns to be synthesized to produce the desired profile in the focal plane while the rest of the treatment volume is virtually free of high-intensity interference patterns. This eliminates one of the major disadvantages of using directly-synthesized patterns for localized heating. This section illustrates the use of such patterns in heating a 30 mm diameter tumor centered 90 mm beneath the skin.

As in the previous section, the power required to maintain a $7°C$ hyperthermia was determined to be 2.5 W. The tumor was to be heated using the directly synthesized annular ring pattern shown in Figure 8.8. The 24 mm diameter ring was synthesized using 20 control points distributed uniformly around its circumference. The effective size of a focal spot generated by the SSA was nearly 0.140 cm^3. The power deposition value at the control points was determined to be 0.9 W/cm^3 to

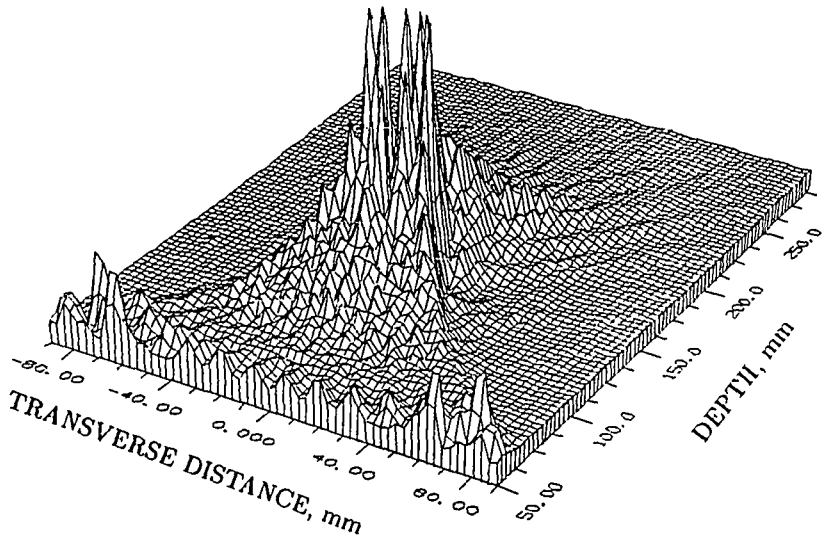

Figure 8.6. Heating pattern generated using multiple-focus scanning with the three-focus pattern (maximum gain) shown in Figure 7.5.

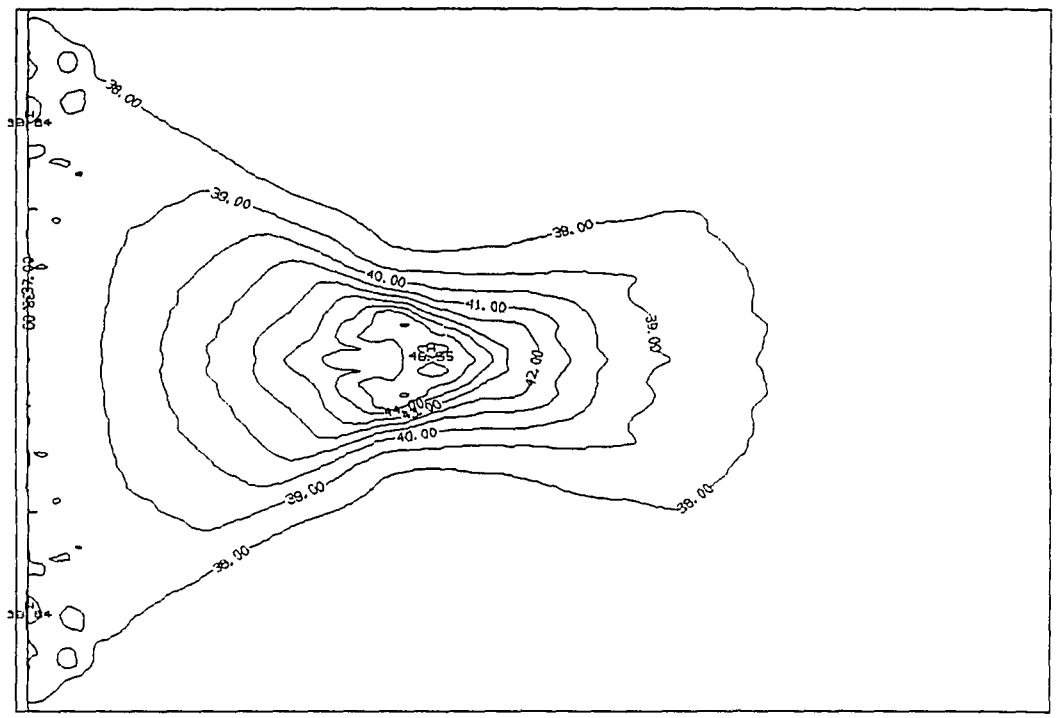

Figure 8.7. Temperature profile resulting from the heating pattern shown in Figure 8.6.

achieve 2.5 W inside the tumor (based on a blood flow of 5 kg/m^3/s). The power at the surface of the array necessary to achieve this power deposition level was 61.6 W. The power concentration ratio for this pattern was 44.4. The resulting temperature distribution reflects the high-power concentration ratio where one can easily see that any significant heating is confined to the tumor region. However, the percentage of the tumor volume above $43°C$ is only 62% which might not be acceptable. Therefore, this heating pattern cannot adequately heat the specified tumor volume.

The annular ring heating pattern of Figure 8.8 fails to deposit sufficient power at the center of the tumor. Therefore, for this relatively well-perfused tumor (blood flow of 5 kg/m^3/sec), a temperature drop occurs in the center of the tumor. This can be remedied by direct synthesis of a pattern that heats the center of the tumor as well as the periphery. Figure 8.10 shows an example of such a pattern. This pattern consists of 30 control points distributed at two annuli, 10 points at the inner (with 12 mm diameter) and 20 points at the outer (with 24 mm diameter). The power deposition level at each of these control points was determined to be 0.62 W/cm^3 to achieve the 2.5 W power inside the tumor. The pattern was synthesized using the pseudoinverse method with the gain maximization technique. The power needed at the surface of the array was 68 W. The power concentration ratio was 53.7. Figure 8.11 shows the temperature profile resulting from the double-ring heating pattern of Figure 8.10. The result shows that the high power concentration ratio leads to a highly localized heating. The percentage of the tumor volume above $43°C$ is 95% and the maximum temperature in the tumor is $47.6°C$.

This last example is very significant since it illustrates that a directly synthesized heating pattern which is capable of therapeutically heating the tumor is possible. This heating pattern eliminates the need for scanning, mechanical or electronic. The importance of the gain maximization technique in the generation of such heating patterns cannot be overemphasized. Not only does this method increase the power

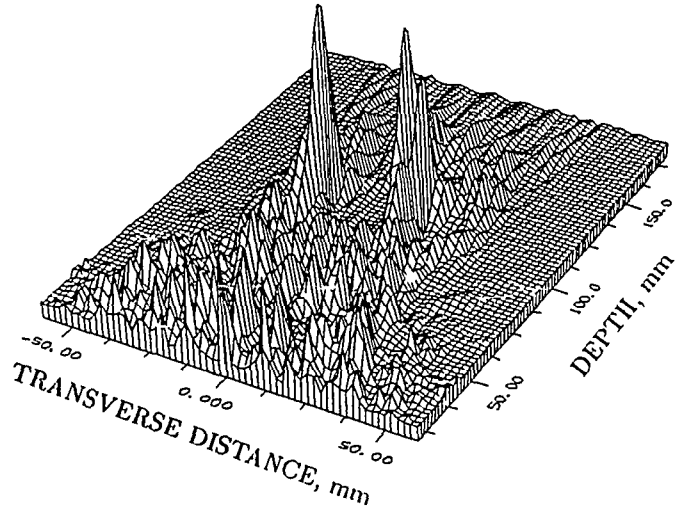

a) $z = 0$ plane.

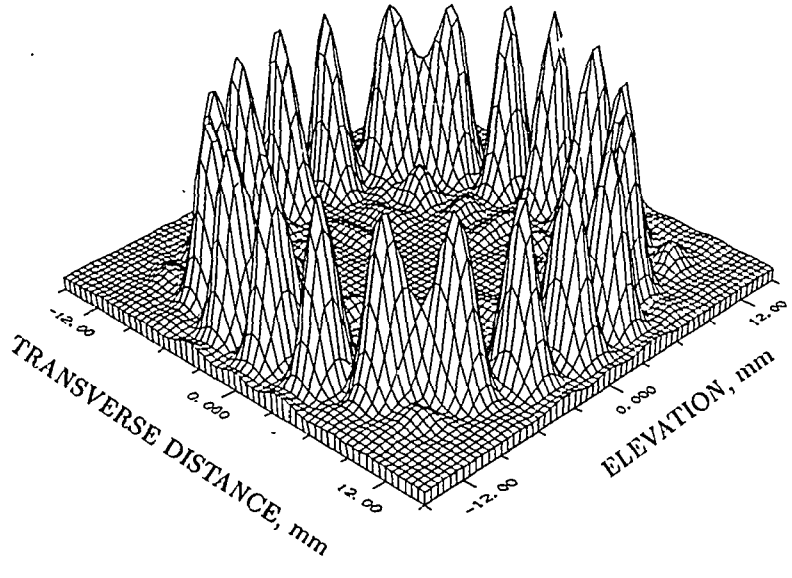

b) Focal plane.

Figure 8.8. Intensity profiles of a 24 *mm* annular pattern synthesized using the pseudoinverse method with gain maximization. The number of control points is 20.

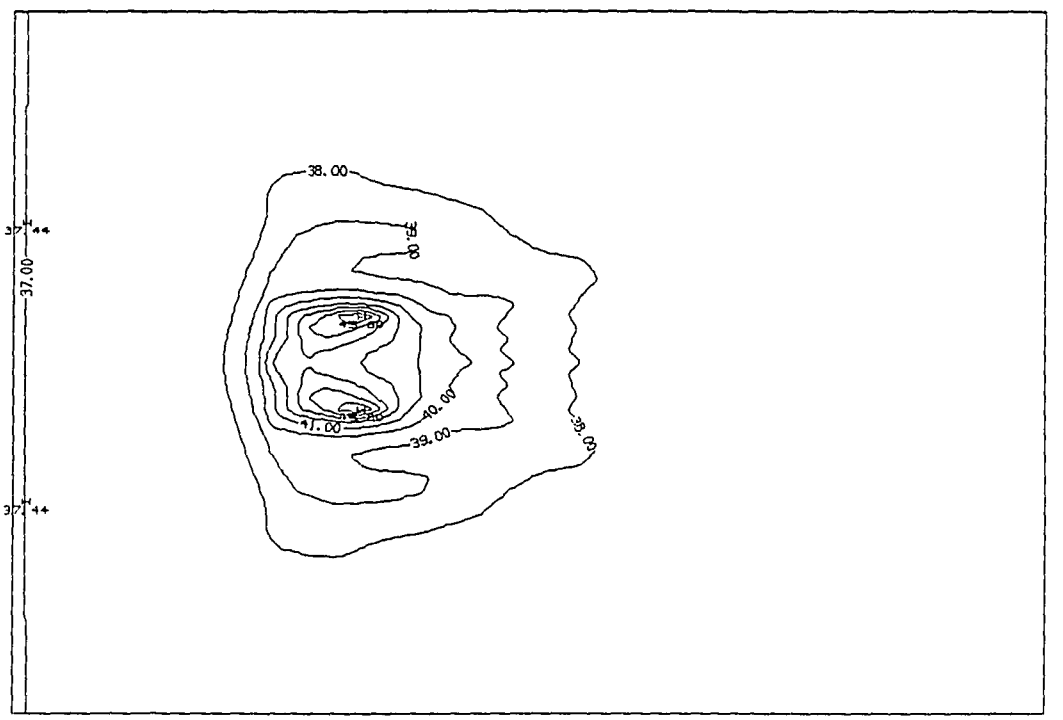

Figure 8.9. Temperature profile resulting from the annular ring pattern of Figure 8.8.

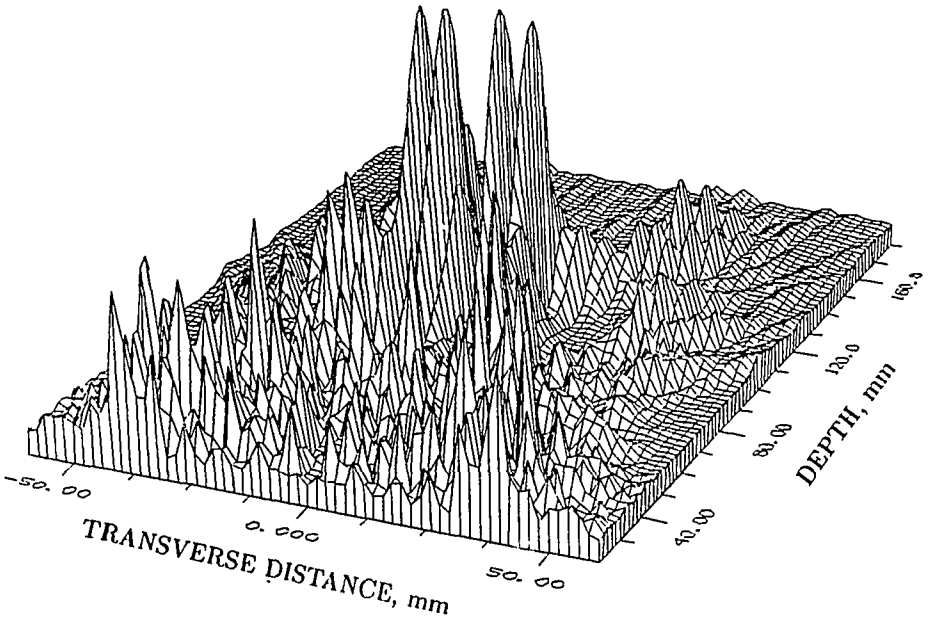

a) $z = 0$ plane.

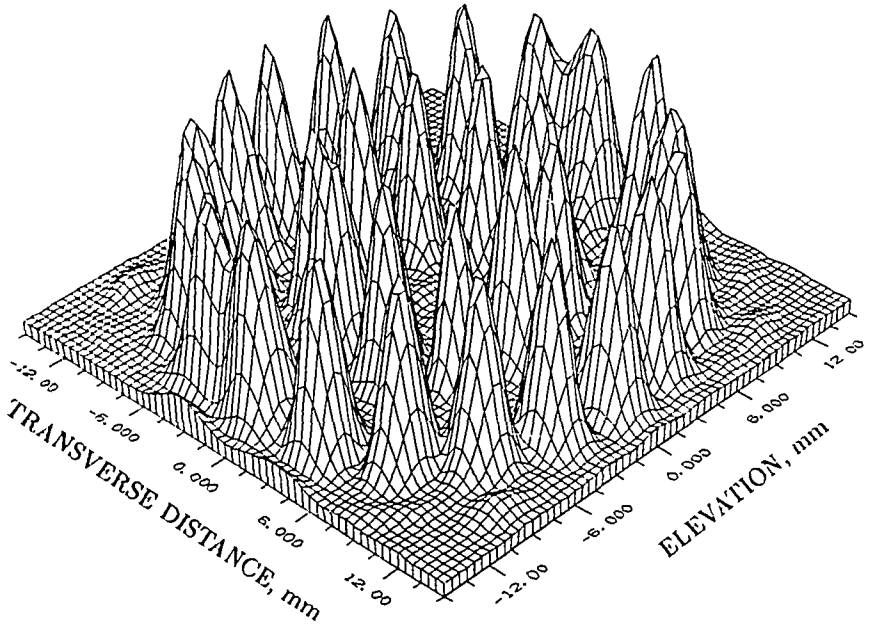

b) Focal plane.

Figure 8.10: Intensity profiles of a directly synthesized double-ring pattern. Inner ring 12 mm diameter, 10 control points. Outer ring 24 mm diameter, 20 control points.

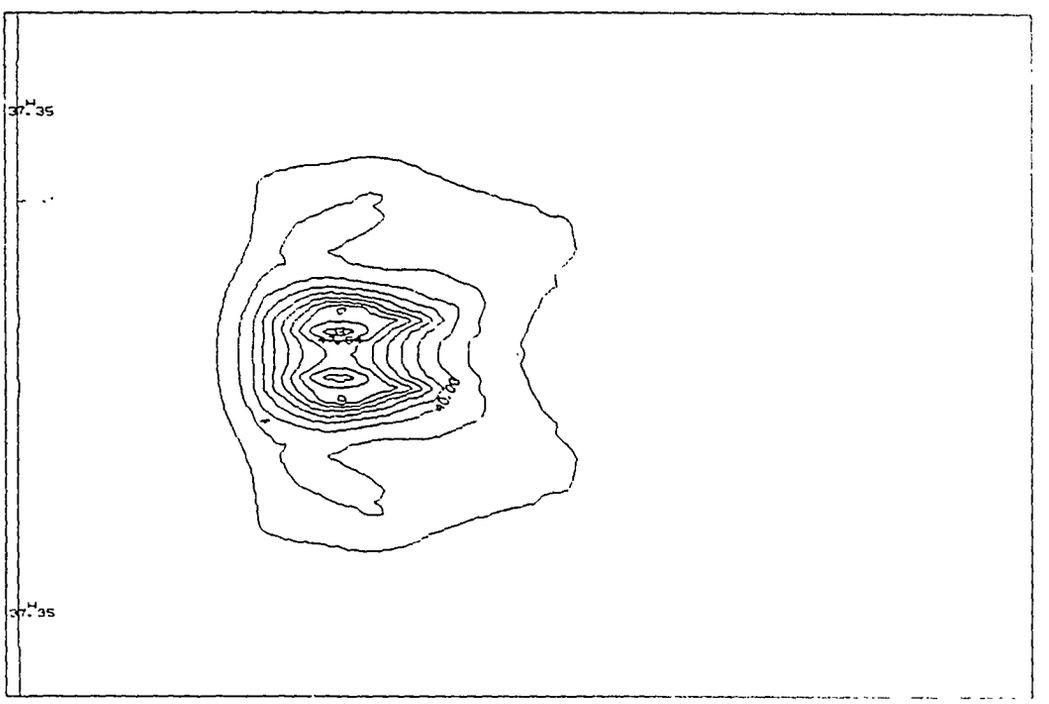

Figure 8.11: Temperature profile resulting from the double-ring pattern shown in Figure 8.10.

deposition at the control points, but it also significantly reduces any high-intensity interference patterns prior to and beyond the focal plane.

Finally, the power concentration ratio, η_Q, seems to provide a good indicator for localization of heat in the tumor. This is seen clearly by comparing the results of Sections 8.5 and 8.6. The three heating patterns described in Section 8.5 have values of η_Q of nearly 18. Although these patterns induce localized heating, the resulting temperature profile in each of these cases has a "tail" which extends from the front of the tumor toward the skin. This extended heating varies from nicely contained (in the case of multiple-focus scanning with gain maximization) to unacceptable (in the case of multiple-focus scanning with no gain maximization) with the single-focus scanning pattern somewhere in between. On the other hand, the heating patterns given in Section 8.6 have more than double the value of η_Q of the previous cases. The resulting temperature profiles indicate that the temperature elevation occurs in the vicinity of the tumor volume in each case.

CHAPTER 9

A PROTOTYPE CYLINDRICAL-SECTION PHASED ARRAY

9.1 General

The previous chapters dealt with the theoretical aspects of the phased-array pattern synthesis problem. The basic tool for verification of theoretical concepts introduced in this thesis was the simulation of wave propagation from the different phased-array structures into an infinite homogeneous medium. Computer simulation provides a powerful tool for the analysis and synthesis of phased-array heating patterns. It provides a controlled environment in which the researcher can isolate the cause and effect factors for the different parameters in the system. This establishes one's understanding of the pattern synthesis problem. Furthermore, computer simulation accelerates the research process especially when a high-performance computer is used. However, the ultimate goal of the research program that made this thesis possible is to design and test prototype phased-array hyperthermia applicators. From the engineering research viewpoint, experimental verification of synthesized field patterns using a phased-array prototype enhances the validity of the simulated field patterns. Furthermore, experimental apparatus would be extremely essential in the verification of the validity of more complicated computer models for the inhomogeneity of the propagation medium.

This chapter describes the initial experience of a prototype cylindrical-section phased-array applicator which has been designed and constructed. The applicator consists of 64 rectangular PZT-8 ceramic elements 3 mm × 50 mm bonded to an aluminum matching plate forming a 75°cylindrical section with a radius of 200 mm. Figure 9.1 shows an isometric view of the CSA with a close-up view of the matching plate and mounted elements. The transducer elements are individually matched to the driving amplifier circuits using the matching circuit configuration shown in Figure 9.2.

9.2 Experimental Setup

Figure 9.3 shows a schematic diagram of the experimental setup used for testing the CSA. The array is driven by a 64-channel amplifier system with independent phase and amplitude control of each element. Amplitude and phase resolutions are 3-bit and 4-bit, respectively. A 16-line Direct Memory Access (DMA) controller card is used for loading the proper driving signals to the digital phase and amplitude controller and a synthesizer/function generator provides a common clock for all the channels to assure proper phasing. The operation frequency is the clock frequency divided by 16. A complete description of the driver assembly is given in [27].

The acoustic output of the CSA is probed by a Nelson-Towmey needle hydrophone. The received electrical signal is digitized and analyzed by a Data Precision D6100 waveform analyzer which filters out the broadband noise and performs rms measurements for the evaluation of the acoustic field strength at the current location of the hydrophone. The probe can be linearly moved in the x-,y- and z-coordinates and rotated in the Φ-direction with a Daedal stepper motor stage driven by Daedal stepper motor indexers. The controller of the driver/stepper motor assembly is provided by a stepper motor control card which is a part of the HP 3852A data acquisition and control unit.

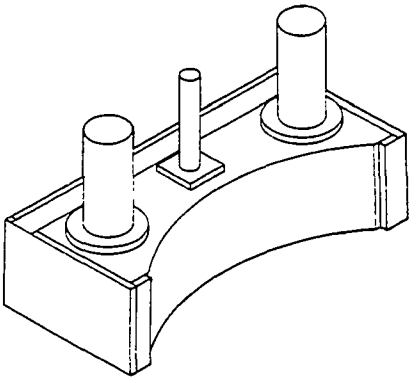

a) Isometric view.

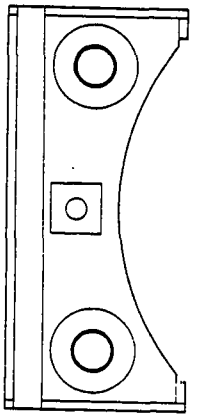

b) Top view.

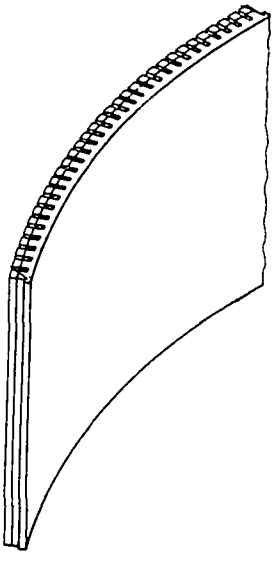

c) Close-up view of matching plate with mounted ceramic elements.

Figure 9.1: The cylindrical-section phased-array prototype.

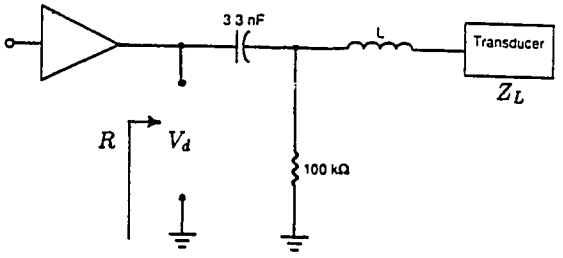

Figure 9.2. Electrical matching circuit between driving amplifiers and transducer elements.

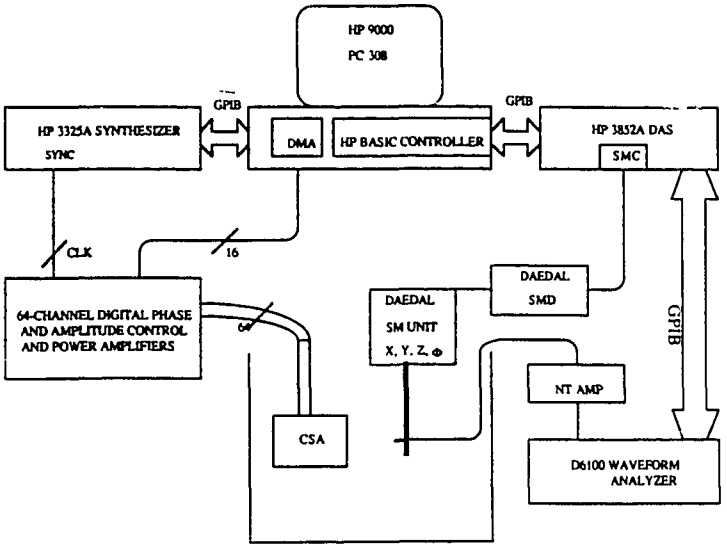

Figure 9.3. Experimental setup for testing the CSA.

9.3 Element Characterization Tests

Two simple tests were performed to characterize the individual elements of the array. First, the array elements were driven individually with a fixed amplitude driving signal and the acoustic signal from each element was recorded at the geometric center of the array. This test provides a measure of the scaling of the magnitude of the driving voltage as it is converted to particle velocity at the surface of each array element. These amplitude scaling factors, η_i, vary from element to element. The results of this test are summarized in Figure 9.4 which shows the distribution of the amplitude scaling factors for the array elements. The nature of the variation in the amplitude scaling factors is modelled in the histogram given in Figure 9.5.

The second test is aimed at estimating the phase shift between the driving voltage and the particle velocity at the surface of each array element. This phase shift is a variable quantity (from element to element) determined by differences in the electrical matching circuit, cable length, and element bonding which might be different for each element of the array. To achieve this, the array elements were driven in pairs with one element designated as a reference element. Assuming that the driving voltages for the reference element and the element under test are $V_r = Ae^{j\phi_r}$ and $V_i = Ae^{j\phi_i}$, respectively, the corresponding particle velocities at the surface of each element are (ignoring mutual coupling between elements) $u_r = V_r\Gamma_r$ and $u_i = V_i\Gamma_i$. The complex constants $\Gamma_r = \alpha_r e^{j\beta_r}$ *and* $\Gamma_i = \alpha_i e^{j\beta_i}$ account for amplitude scaling and phase shift between the driving signals and the surface particle velocity. The complex pressure at the geometrical center of the array is given by

$$p = D(V_r\Gamma_r + V_i\Gamma_i), \tag{9.1}$$

where D is a complex number accounting for the element directivity and propagation from the array surface to the measurement point (this factor is the same for all array elements when the measurement is performed at its center). The intensity of the

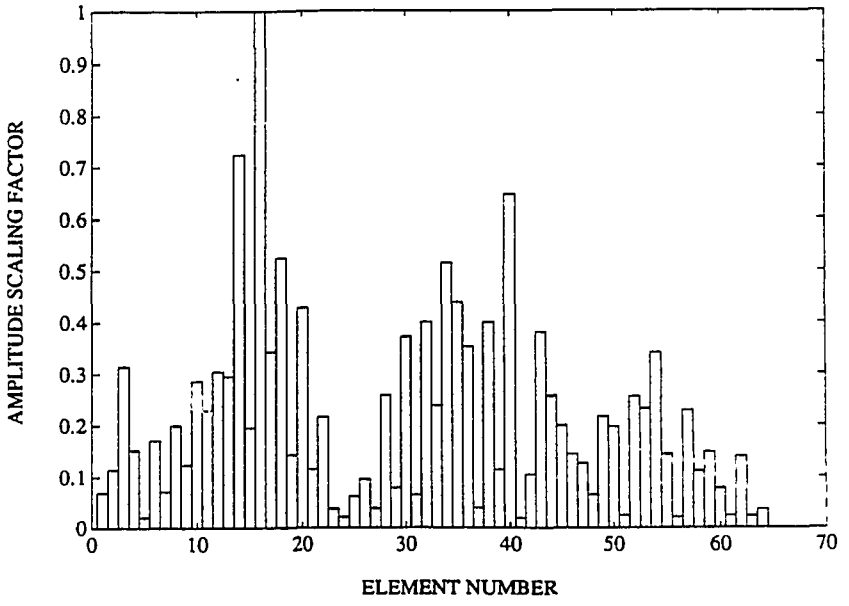

Figure 9.4. Distribution of the amplitude scaling factors for the CSA1D prototype.

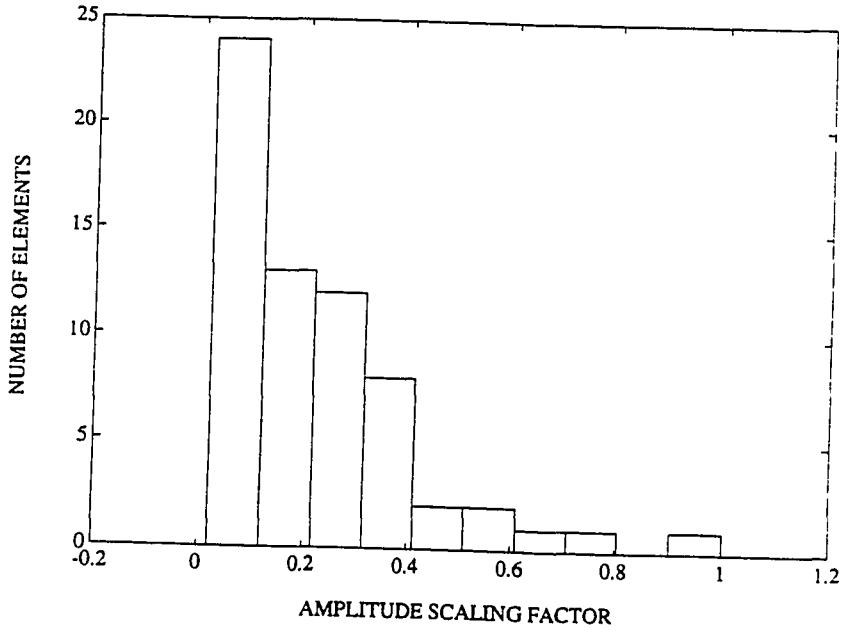

Figure 9.5. A histogram of the amplitude scaling-factor distribution for the CSA1D prototype.

measured signal is

$$I = K(\alpha_i^2 + \alpha_r^2 + 2\ Re(J)), \tag{9.2}$$

where K is a real constant, and J is a complex quantity given by

$$J = \alpha_i \alpha_r e^{j(\phi_i - \phi_r + \beta_i - \beta_r)}. \tag{9.3}$$

Clearly, the measured intensity is maximum when $\arg(J)$ is zero, or

$$\begin{aligned} \Delta\phi_i &= \phi_i - \phi_r \\ &= \beta_r - \beta_i. \end{aligned} \tag{9.4}$$

This quantity, $\Delta\phi_i$, is a measure of the phase shift between the driving voltage and the particle velocity for each element of the array.

The results of the phase-error measurements are summarized in Figure 9.6 which shows the phase-error distribution for the CSA1D. Figure 9.7 shows a histogram of the phase-error variation.

9.4 Simulation Algorithm

An ideal CSA with dimensions corresponding to those given in Section 9.1 was simulated in water to find the excitation vector, $\hat{\mathbf{u}}$, using the pseudoinverse method (see Section 6.4). The elements of the vector $\hat{\mathbf{u}}$ were quantized (according to the quantization rules given in Section 7.5) and downloaded to the digital phase and amplitude controller which provides the electrical driving signal distribution at the output of the amplifiers.

The simulated profiles were obtained by evaluating the Rayleigh-Sommerfeld integral on the surface of the array with and without accounting for the phase shifts and amplitude scaling between the electrical driving signals and the particle velocity at the surface of the array. Assuming ideal conditions, the electrical driving signals were used as surface particle velocity on their corresponding elements of the array

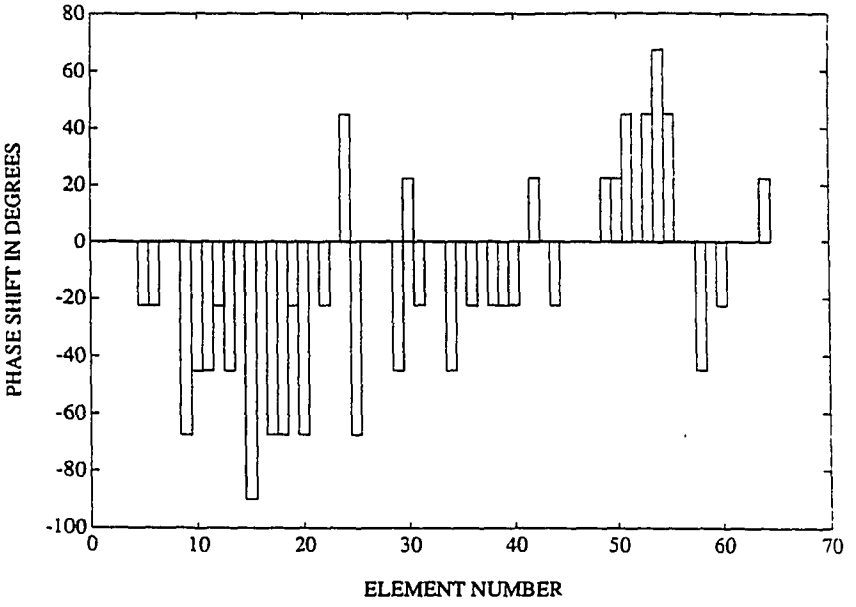

Figure 9.6. Distribution of the phase error for the CSA1D prototype.

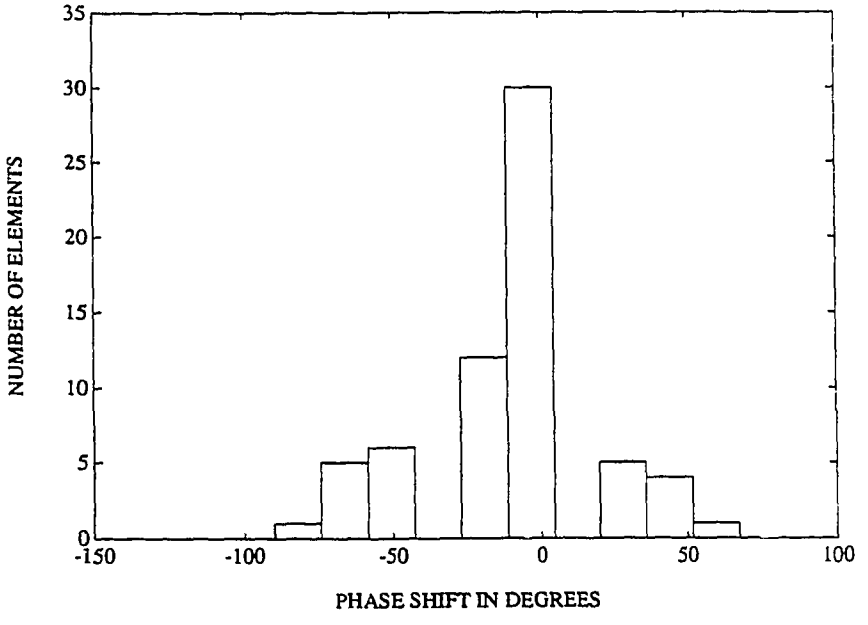

Figure 9.7. A histogram of the phase-error distribution for the CSA1D prototype.

to obtain the simulated intensity profiles. These will be referred to as ideal simulated profiles. Accounting for different amplitude scaling and phase shifts between the electrical driving signals and surface particle velocity, the particle velocity at the surface of the ith element was assumed to take the value

$$u_i = K\eta_i e^{j(\Delta\phi_i+\gamma)}V_i, \tag{9.5}$$

where K is a constant, γ is a constant phase shift across the matching plate, and V_i is the complex driving voltage to the ith element. These will be referred to as phase-compensated intensity profiles, i.e., simulated patterns using the actual measured phase shifts between the driving signals and the surface particle velocity.

9.5 Experimental Results

The prototype CSA was tested in a water tank at an operating frequency of 500 kHz. Acoustic field intensity profiles were measured along a transversal line at a depth of 200 mm from the vertex of the array passing its geometrical center. The span of the measurement line was 40 mm (symmetrical around the axis of the array) with spacing between measurement points of 0.2 mm. Simulated intensity profiles (both ideal and phase-compensated) were evaluated at 500 kHz at a corresponding set of points.

Figure 9.8 is a graph of the simulated (ideal in solid line and phase-compensated in dashed line) and measured (in dashed dotted line) normalized intensity profiles of the characteristic focus of the CSA along the measurement line. This focus was formed by driving the array with uniform amplitude and phase driving-signal distribution. This focus is due to the geometry of the array. The measured intensity profile exhibits asymmetrical side lobes. The phase-compensated intensity profile agrees well with the measured results for the first three side lobes on both sides of the main beam.

The intensity at the geometric focus was measured by a calibrated Marconi PVDF bilaminar shielded hydrophone (Serial Number IP056). A wideband preamplifier was

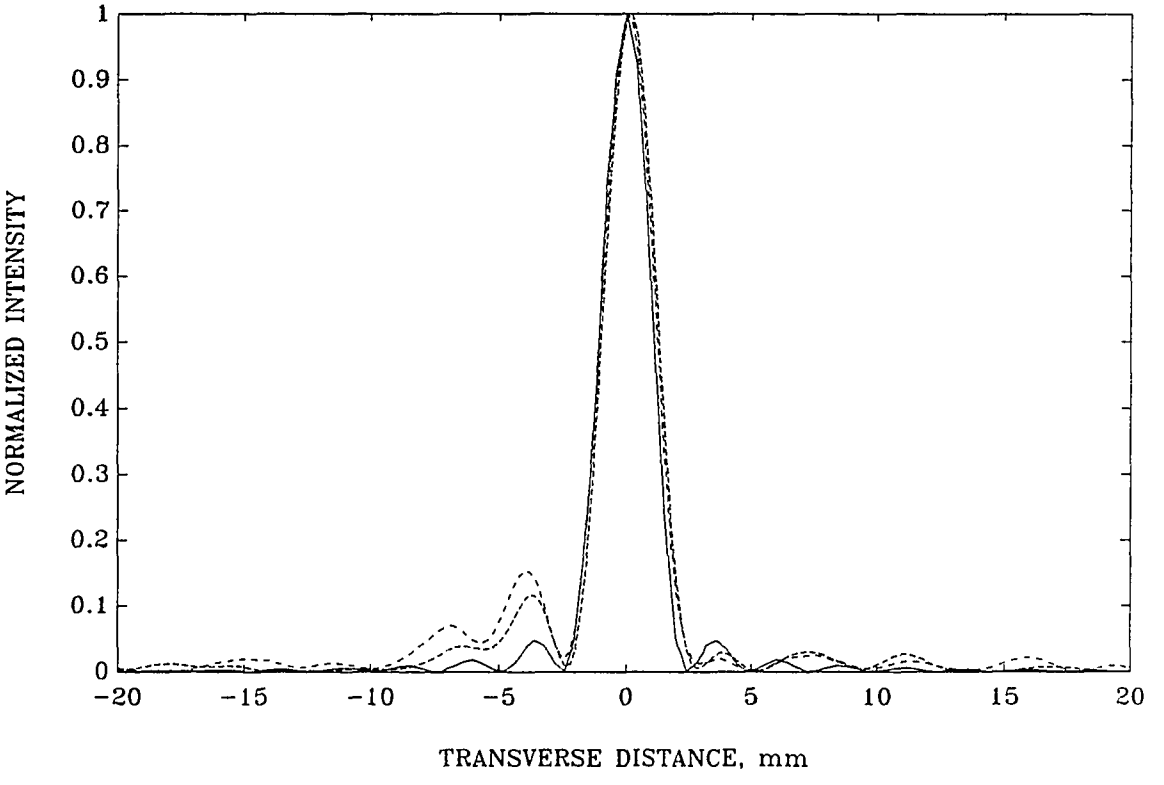

Figure 9.8. Intensity profiles of the characteristic focus of the CSA. (Solid line, ideal; dashed line, phase-compensated; dashed-dotted line, measured.)

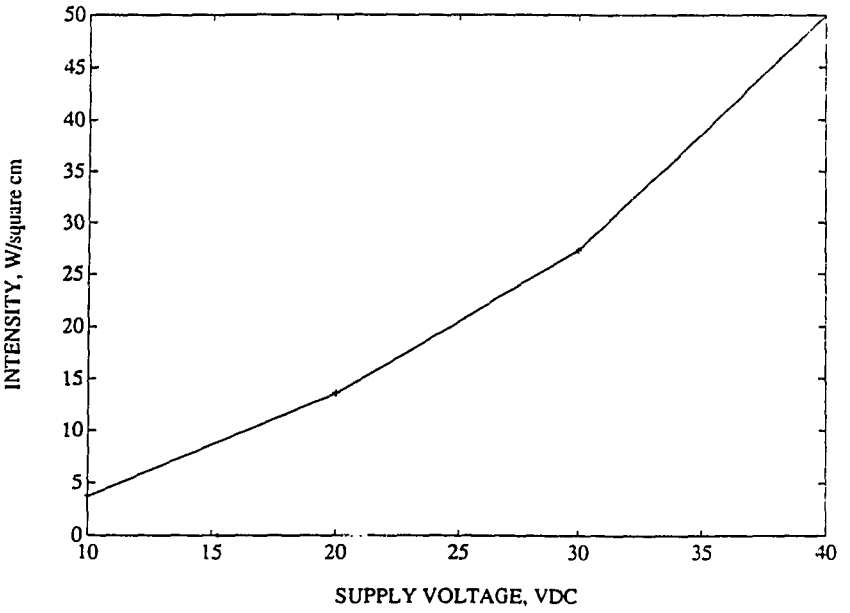

Figure 9.9. The focal intensity at the geometric focus as a function of the dc supply voltage.

also used (G. E. C. Identity Y-33-9724, Serial Number IP135). The hydrophone and the preamplifier were originally calibrated at the National Physical Laboratory, England. Calibration at 500 kHz was performed at the Bioacoustics Research Laboratory at the University of Illinois using the suspended ball technique [30]. Figure 9.9 shows the focal intensity of the geometric focus of the array as a function of the dc supply voltage (which determines the maximum amplitude of the driving signals). The focal intensity of the geometric focus shown in Figure 9.8 was 13.5 W/cm^2 (the dc supply level was 20 VDC).

A shifted focus field pattern was synthesized by focusing the array at a point located 10 mm off the axis of the array at a depth of 200 mm from its vertex. Figure 9.10 shows the simulated and measured normalized intensity profiles. This case also shows that the phase-compensated simulated profile can be used to predict the actual intensity profile.

The pseudoinverse method was used to synthesize a double-focus field pattern in a plane 200 mm deep. The two foci were at -5 mm and 10 mm from the geometrical center of the array. Figure 9.11 shows the simulated and measured normalized intensity profiles corresponding to this case. A slight shift of the focus at 10 mm can be noticed for both the simulated and the measured results. Moreover, the relative intensity of the two foci in the resulting field pattern is different from the intended value (which is 1 : 1). One can see clearly that the phase-compensated simulated intensity profile is still capable of predicting the actual profile even when multiple-focus patterns are simulated.

Finally, the phases of the driving signals to the array elements were preshifted by the $\Delta\phi_i$'s, i.e.,

$$\Delta\phi_i^d = \Delta\phi_i^c - \Delta\phi_i,$$

where $\Delta\phi_i^d$ and $\Delta\phi_i^c$ are, respectively, the actual driving phase and the computed driving phase. This phase distribution was then used to drive the array to produce the shifted focus of Figure 9.10. This was done to examine the possibility of removing the effect of phase error from the measured intensity profile. Figure 9.12 shows a dB plot of the measured phase-corrected intensity profile and the measured intensity profile of Figure 9.10. The dB measurements were made with reference to the focal intensity of the geometric focus in Figure 9.8 (this shows that the focal intensity of the steered focus is reduced by 1.2 dB from the geometric focus intensity level). The results indicate that these two patterns differ mainly in the sidelobes. Furthermore, the result demonstrates the fact that the phase-corrected profile has more balanced side lobes. A similar result was obtained with the geometric focus case of Figure 9.8. However, no significant improvement in the double-focus pattern was observed due to phase correction. The following section summarizes the results obtained with this experimental setup.

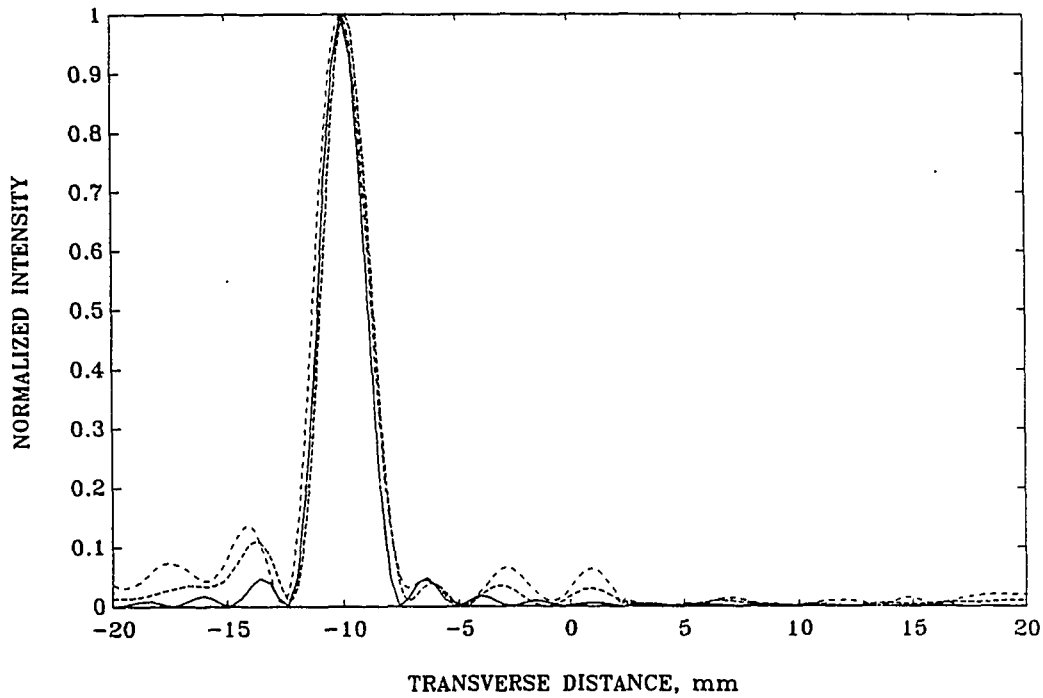

Figure 9.10. Intensity profiles of a shifted focus of the CSA. (Solid line, ideal; dashed line, phase-compensated; dashed-dotted line, measured.)

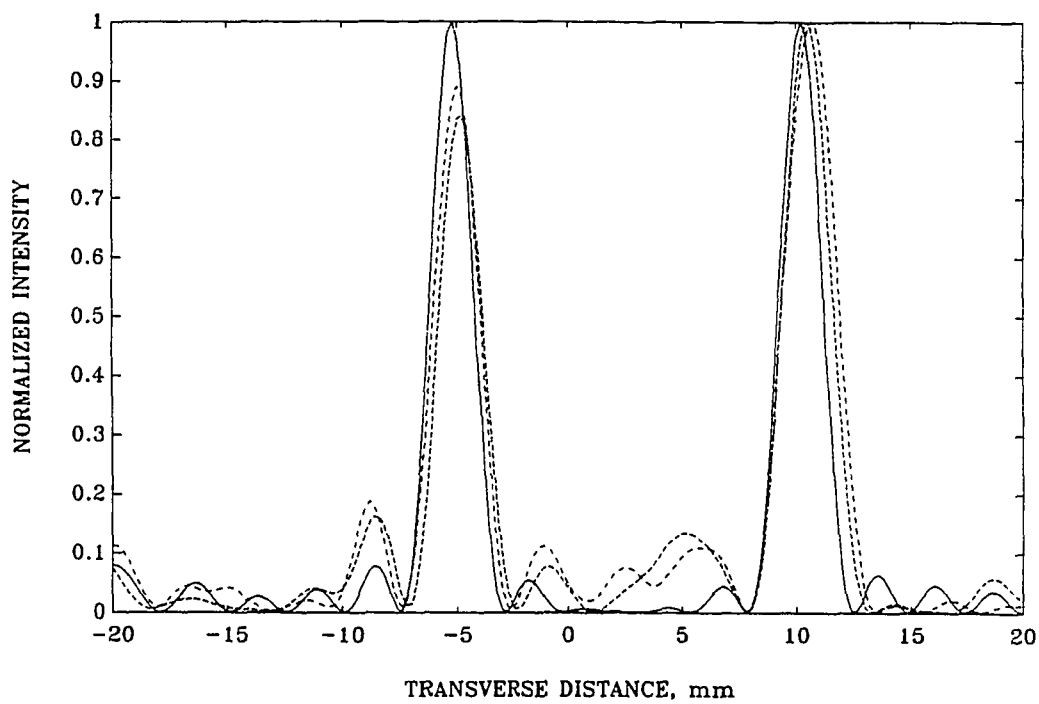

Figure 9.11. Intensity profiles of a double-focus of the CSA. (Solid line, ideal; dashed line, phase-compensated; dashed-dotted line, measured.)

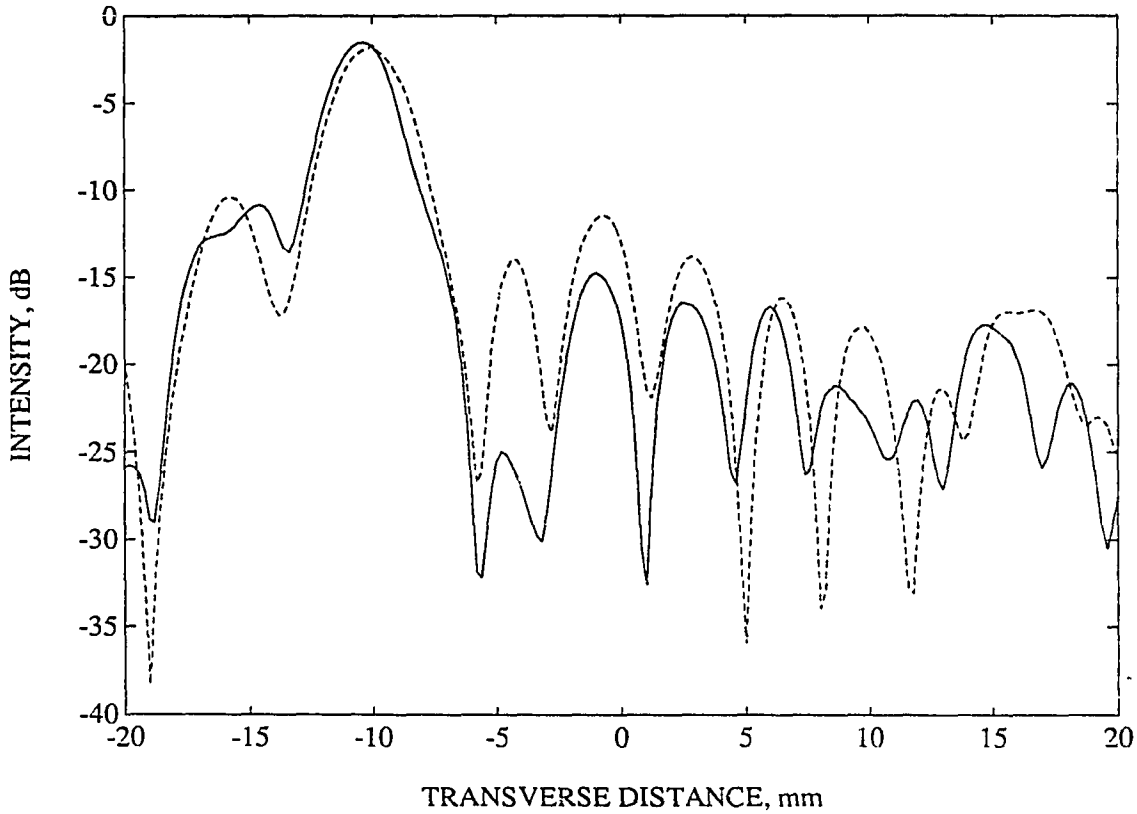

Figure 9.12. Measured intensity profiles in the focal plane of the shifted focus of Figure 9.8. (Solid line, same as Figure 9.8; dashed line, phase-corrected profile.)

9.6 Concluding Remarks

The prototype CSA was tested in a water tank and was shown to be capable of generating single-focus and double-focus field patterns with the pseudoinverse method. Simple tests were performed that enabled the prediction of the surface particle velocity from the electrical driving signal by accounting for differences in matching circuits, cable lengths, and bonding of the individual elements of the array. Thus, the theoretical simulation predicts the actual field pattern generated from the prototype rather than that resulting from an ideal array structure. This simulation technique, although simple and straightforward, proved useful in predicting the actual intensity profiles as the results suggest. Indeed, the phase-compensated intensity profile in Figure 9.11 predicted the slight shift of the focus at 10 mm and the drop of the relative intensity at the focus at -5 mm. These results are encouraging since the values of $\Delta\phi_i$ were measured with 4-bit resolution (using the digital phase and amplitude control circuit). These estimates can be improved substantially by available phase measurement apparatus (a dual-channel synthesizer is available with phase resolution of 1° for each channel), hence allowing improved agreement between the phase-compensated and actual profiles. From a hyperthermia perspective, the fact that the simulated and measured profiles differ only in the sidelobes attests to the robustness of the synthesis procedure.

A significant conclusion that can be made from the above results is that the imperfections in the fabrication of the array can be successfully accounted for. The next step would be to account for these imperfections in the pseudoinverse formulation. This allows for the evaluation of the driving voltages at the output of the amplifiers in terms of the specified pressures at the control points. Although this has no bearing on the synthesis problem, it is an important practical issue which needs to be addressed.

CHAPTER 10

CONCLUSIONS AND RECOMMENDATIONS FOR FUTURE WORK

10.1 Conclusions

The problem of phased-array pattern synthesis for inducing deep localized hyperthermia was considered. The thesis research examined the possibility of improving both the applicator geometry and the phasing scheme to achieve heating patterns capable of therapeutically heating realistically sized tumors at depth. The main components of this thesis research are (in chronological order)

1. New nonplanar (geometrically focused) phased arrays were analyzed for potential usefulness as deep localized hyperthermia applicators. Specifically, the CSA1D, CSA2D, and SSA array structures were examined. These arrays were compared with equivalent planar arrays. Two arrays were considered to be equivalent if they have the same number of elements (with the same size) and the same center-to-center spacing between the elements. The comparison was based on the focal intensity gain and grating- lobe intensity level for shifted and unshifted foci with the same $\frac{F}{D}$ for both arrays. Compared to their equivalent planar arrays, nonplanar phased arrays offer the following advantages which could be significant for deep localized hyperthermia:

(a) Higher focal intensity gain which can be very significant in sparing the intervening tissues and assuring efficient heating within the tumor.

(b) Lower relative intensity at the grating lobe which is very necessary for heat localization.

(c) Smaller focal spot size (especially in the longitudinal direction) which is very important for localized heating of small-to-medium sized tumors.

2. The pseudoinverse pattern synthesis method was introduced and analyzed. The method finds the minimum-norm least-square error solution to an operator equation of the form $\mathbf{Hu} = \mathbf{p}$, which relates the array excitation vector at the surface of the array, $\mathbf{u}$, to the complex pressures at a set of *control points* in the treatment volume, $\mathbf{p}$. The operator equation was discretized and reduced to a system of linear equations which was solved in a finite dimensional space setting.

   The minimum-norm solution was emphasized throughout this thesis. There are several advantages to the use of this solution in phased-array pattern synthesis.

   (a) The minimum-norm solution reproduces the specified power deposition levels exactly at the control points, therefore, allowing for precise control of the heating pattern.

   (b) The field distribution produced by the minimum-norm solution tends to concentrate the energy around the control points, i.e., the energy is focused at these points.

   (c) The minimum-norm solution allows the optimization of the intensity gain and array excitation efficiency. In fact, simulation results indicate that the maximization of intensity using the minimum-norm solution virtually eliminates high-intensity interference patterns from multiple-focus fields, thus eliminating one of the major disadvantages of multiple-focusing.

(d) Exercising reasonable precautions in the selection of the control points typically results in a well-conditioned propagation operator which results in robust synthesis. The only precaution to be observed is not to choose spacing between control points in a specific direction to be smaller than the dimension of the point-spread function of the array in that direction.

3. The various approaches to heating pattern generation with several different phased arrays were considered. The procedure for the determination of excitation signals at the surface of the array capable of producing the specified power deposition in the tumor was outlined. Also, a number of performance indices for heating patterns were identified and used in comparing their heating efficacy. Multiple-focus field patterns obtained with gain maximization techniques were shown to provide an alternative to conventional single-focus scanning. In fact, a directly synthesized double-ring pattern was shown to be capable of adequately heating a tumor without the need for scanning. Significantly, therapeutic temperature profiles obtained with this technique were highly localized to the tumor volume.

4. Initial experimental results with a prototype cylindrical-section phased array are in good agreement with the theoretical predictions. A double-focus pattern was synthesized and realized experimentally despite various sources of error due to array imperfections, quantization, etc. This attests to the robustness of the minimum-norm formulation.

The following conclusions can be drawn from the work performed in the course of this thesis research:

1. Simulation results show that deep localized hyperthermia is achievable when the applicator geometry and the phasing scheme are chosen properly.

2. Multiple-focus scanning and directly synthesized heating patterns can successfully substitute for single-focus scanning.

3. The gain maximization technique generally results in removing high intensity interference patterns. This eliminates the most significant disadvantage of direct synthesis as a method for heating pattern generation.

4. Experimental measurements with the CSA1D prototype prove that computer simulation is a useful tool in the analysis and design of phased-array applicators.

10.2 Recommendations for Future Work

This thesis dealt with the synthesis problem in a deterministic sense. This approach was sufficient to prove the validity of the different concepts introduced in the course of this work. In a practical situation, the entries of the propagation operator, $\mathbf{H}$, can be either measured or computed based on a numerical nonhomogeneous model of the treatment volume. When this is the case, then the entries of $\mathbf{H}$ will be inexact. The propagation operator is generally well-conditioned and the inversion should be stable against errors in the entries of $\mathbf{H}$. However, a statistical description of the form

$$\tilde{\mathbf{H}} = \mathbf{H} + \mathbf{E}, \tag{10.1}$$

where $\tilde{\mathbf{H}}$ is the actual propagation operator, and $\mathbf{E}$ represents the error or uncertainty in $\mathbf{H}$, will be necessary to study the performance of the pseudoinverse in the presence of noise.

The experimental measurements obtained with the cylindrical-section phased-array prototype were very encouraging. Both single-focus and double-focus patterns were successfully synthesized. However, further investigation of this array is necessary. Specifically, its ability to heat realistic tissue volumes, e.g., perfused kidney, needs to be tested. Furthermore, the simulation results given in Section 8.5 were

obtained using a 120 element CSA2D. Fabricating this array would be a straightforward extension of the CSA1D prototype. A prototype CSA2D would provide true three-dimensional control of heating patterns. In addition, it would allow direct synthesis of more complex multiple-focus patterns potentially useful in hyperthermia. Such an applicator prototype would be invaluable to the course of this research.

The concept of *real-time adaptive control* of phased-array heating patterns needs to be developed. With the pseudoinverse method, the power deposition level at any of the control points can be changed at any time (increased or decreased) if the matrix $\mathbf{H}^{*t}(\mathbf{H}\mathbf{H}^{*t})^{-1}$ is available. In addition, potential hot spots can be removed by placing additional control points at the location of the interference which force the field to take relatively low intensity levels there. A recursive algorithm to achieve this is given in [21]. However, the addition of more control points unnecessarily increases the size of the operator $\mathbf{H}$. This could result in an ill-conditioned propagation operator which can produce unacceptable errors in synthesis. A suitable adaptive algorithm for reducing the interference at a point other than the originally specified control points is one that expresses the excitation vector at each time step as a difference between two orthogonal components;

$$\mathbf{u}(t+1) = \mathbf{u}(0) - \mathbf{v}(t), \tag{10.2}$$

at time $t+1$, where $\mathbf{u}(0) = \mathbf{H}^{*t}(\mathbf{H}\mathbf{H}^{*t})^{-1}\mathbf{p}$ (the minimum-norm solution resulting from the definition of the original control points), and $\mathbf{v}(t)$ belongs to the null space of the adjoint $\mathbf{H}^{*t}$. This condition guarantees that $\mathbf{H}\mathbf{u}(t+1) = \mathbf{H}\mathbf{u}(0) = \mathbf{p}; \forall t$, i.e., updating the excitation vector does not disturb the power deposition levels at the original control points. The excitation vector should converge to a value which minimizes the power deposition at the point of interference in a finite number of steps.

The implementation of such an adaptive algorithm will provide the necessary tool for successful realization of a phased-array hyperthermia applicator in the clinic. This

is essential because of the rapidly changing tumor environment during the treatment. In this case, however, the main problem is not the development of adaptive algorithms per se, but identifying the necessary and sufficient feedback parameters that determine the next step of the adaptive algorithm. In the absence of an adequate noninvasive temperature mapping technique, more experimental and theoretical work needs to be done in the area of reconstructing temperature profiles from a limited set of data and an assumed mathematical model. This problem is currently being researched by several groups [33, 65, 66].

Finally, one of the essential tools for treatment planning would be the development of suitable software that realistically models the treatment volume both for wave propagation and thermal computations. For this, one needs an accurate description of the treatment volume if available, e.g., CT scan data. The integration of the pseudoinverse method with a suitable model of the treatment volume will provide a powerful treatment planning procedure.

LIST OF REFERENCES

[1] G. Hahn,"Hyperthermia for the engineer: A short biological primer," *IEEE Trans. Bio-Med. Eng.*, vol. BME-31, no. 1, pp. 3-8, 1984.

[2] T. Sumulski, E. Lee, and G. Hahn,"Hyperthermia as a clinical treatment modality," *Cancer Treatment Reports*, vol. 68, no. 1, pp. 309-316, 1984.

[3] R. Roemer,"The thermal goal of practical, clinical hyperthermia treatments: Definition, rationale, implementations," Presentation to the Eighth Annual Meeting of the North American Hyperthermia Group, Philadelphia, PA, 1988.

[4] P. Lele,"Physical aspects and clinical studies with ultrasonic hyperthermia," in *Hyperthermia in Cancer Therapy.* F. Storm, Ed., Boston, MA: G. K. Hall Medical Publishers, 1983.

[5] R. Dickenson, J. Hand, and S. Leeman, "The design of focused transducers for ultrasound hyperthermia," *Proceedings of the IEEE Ultrasonics Symposium*, pp. 739-742, 1982.

[6] P. Fessenden, E. Lee, T. Anderson, J. Strohbehn, J. Meyer, T. Samulski, and J. Marmor, "Experience with a multitransducer ultrasound system for localized hyperthermia of deep tissues," *IEEE Trans. Bio-Med. Eng.*, vol. BME-31, no. 1, pp. 126-135.

[7] K. Hynenen, R. Roemer, D. Anhalt, C. Johnson, Z. Xu, W. Swindell, and T. Cetas," A scanned, focused, multiple transducer ultrasonic system for localized hyperthermia treatments," *Int. J. Hyperthermia*, vol. 3, no. 1, pp. 21-35, 1987.

[8] E. Ebbini, S. Umemura, M. Ibbini, and C. Cain," A cylindrical-section ultrasound phased-array applicator for hyperthermia cancer therapy," *IEEE Trans. Ultrasonics Ferroelectrics Frequency Control*, vol. 35, no. 5, pp. 561-572, 1988.

[9] E. Ebbini,"Ultrasonic cylindrical phased-array applicators for deep, localized hyperthermia," M.S. thesis, University of Illinois at Urbana-Champaign, 1987.

[10] E. Carstensen, W. Law, and D. McKay," Demonstration of nonlinear acoustical effects at biomedical frequencies and intensities," *Ultrasound in Med. and Biology*, vol. 6, pp. 359-368, 1980.

[11] W.Swindell,"A theoretical study of nonlinear effects with focused ultrasound in tissues: An acoustic Bragg peak," *Ultrasound in Med. and Biology*, vol. 11, no. 1, pp. 121-130, 1985.

[12] K. Ocheltree, "Analysis of power deposition patterns and ultrasonic phased arrays for localized hyperthermia," Ph.D. dissertation, University of Illinois at Urbana-Champaign. 1987.

[13] M. Ibbini and C. Cain, "Ultrasonic phased array hyperthermia field patterns using a field conjugation method," *IEEE Trans. Ultrasonics Ferroelectrics Frequency Control*, vol. 36, no. 1, pp. 1-5, 1989.

[14] E. Ebbini and C. Cain," Multiple-focus ultrasound phased-array pattern synthesis: Optimal driving signal distributions for hyperthermia," *IEEE Trans. Ultrasonics Ferroelectrics Frequency Control*, vol. 36, no. 5, pp. 540-548, 1989.

[15] S. Leon,*Linear Algebra with Applications*, 2nd Ed., New York: Macmillan, 1980.

[16] J. Do Huu and P. Hartmann, "Annular array transducer for deep acoustic hyperthermia," *Proceedings of the IEEE Ultrasonics Symposium*, pp. 705-710, 1981.

[17] C. Cain and S. Umemura, "Concentric-ring and sector-vortex phased-array applicators for ultrasound hyperthermia," *IEEE Trans. Microwave Theory Technique*, vol. MTT-34, no. 5, pp. 542-551, 1986.

[18] T. Cavvichi and W. O'Brien, Jr., "Heat generated by ultrasound in an absorbing medium," *J. Acoust. Soc. Amer.*, vol. 76, no. 4, Oct. 1984.

[19] J. Baish, P. Ayyaswamy, and K. Foster, "Heat transport mechanisms in vascular tissues: A model comparison," to appear in the *Journal of Biomechanical Engineering.*

[20] Jaluria and Yogesh, *Computational Heat Transfer.* Washington, DC: Hemisphere Publishing, 1986.

[21] H. Wang, E. Ebbini, and C. Cain, "Computationally efficient algorithms for control of ultrasound phased array hyperthermia applicators based on a pseudoinverse method," accepted for publication *IEEE Trans. Ultrasonics Ferroelectrics Frequency Control*, 1990.

[22] D. Luenberger, *Optimization by Vector Space Methods.* New York: John Wiley, 1969.

[23] P. Benkeser, "Investigation of linear phased arrays for hyperthermia applicators," M.S. thesis, University of Illinois at Urbana-Champaign, 1981.

[24] K. Ocheltree, "Theoretical analysis of linear phased array for hyperthermia treatment," M.S. thesis, University of Illinois at Urbana-Champaign, 1984.

[25] P. Corry, K. Jabboury, E. Armour, and J. Kong, "Human cancer treatment with ultrasound." *IEEE Trans. Sonics Ultrason.*, vol. SU-31, no. 5, pp. 444-456, 1984.

[26] R. Roemer, W. Swindell, S. Clegg, and R. Kress, "Simulation of a focused scanned ultrasonic heating of deep-seated tumors: The effects of blood perfusion," *IEEE Trans. Sonics Ultrason.*, vol. SU-31, no. 5, pp. 457-466, 1984.

[27] F. Ngo, "Ultrasonic phased-array driver system," M.S. thesis, University of Illinois at Urbana-Champaign, 1989.

[28] H. Wang,"Effects of tissue inhomogeneity on ultrasound phased array field patterns for hyperthermia cancer therapy" M. S. thesis, University of Illinois at Urbana-Champaign, 1989.

[29] P. Benkeser, "Unfocused multielement and tapered phased array ultrasound transducers for hyperthermia treatment" Ph. D. dissertation, University of Illinois at Urbana-Champaign, 1984.

[30] R. Preston et al., "Interlaboratory comparison of hydrophone calibrations," *IEEE Trans. Ultrasonics Ferroelectrics Frequency Control*, vol. 35, no. 2, pp. 206-213, 1988.

[31] R. Magin and A. Peterson, "Noninvasive microwave phased arrays for local hyperthermia: A review," Int. J. Hyperthermia, vol. 5, no. 4, pp. 429-450, 1989.

[32] S. Sapareto, "The biology of hyperthermia in vitro," in *Physical Aspects of Hyperthermia.* G. Nausbaum, Ed., New York: AAPM, 1982.

[33] S. Clegg and R. Roemer, "Toward the estimation of three-dimensional temperature fields from noisy temperature measurements during hyperthermia," Int. J. Hyperthermia, vol. 5, no. 4, pp. 467-484, 1989.

[34] K. Hynynen, D. DeYoung, M. Kundrat and E. Moros, "The effect of blood perfusion rate on the temperature distributions induced by multiple, scanned and focused ultrasonic beams in dogs' kidneys in vivo," Int. J. Hyperthermia, vol. 5, no. 4, pp. 485- 498, 1989.

[35] F. Hetzel, "Hyperthermia in vivo," in *Physical Aspects of Hyperthermia.* G. Nausbaum, Ed., New York: AAPM, 1982.

[36] C. Song, "Physiological factors in hyperthermia of tumors," in *Physical Aspects of Hyperthermia.* G. Nausbaum, Ed., New York: AAPM, 1982.

[37] C. Perez, "Rationale for clinical application of hyperthermia: Alone or combined with irradiation or cytotoxic drugs in cancer therapy," in *Physical Aspects of Hyperthermia.* G. Nausbaum, Ed., New York: AAPM, 1982.

[38] G. Nausbaum, "Conceptual outline of hyperthermia physics," in *Physical Aspects of Hyperthermia.* G. Nausbaum, Ed., New York: AAPM, 1982.

[39] E. Burdette, "Electromagnatic and acoustic properties of tissues," in *Physical Aspects of Hyperthermia.* G. Nausbaum, Ed., New York: AAPM, 1982.

[40] F. Barber and C. Griffice, "Power deposition for ultrasound hyperthermia," in *Physical Aspects of Hyperthermia.* G. Nausbaum, Ed., New York: AAPM, 1982.

[41] P. Lele, "Local hyperthermia by ultrasound," in *Physical Aspects of Hyperthermia.* G. Nausbaum, Ed., New York: AAPM, 1982.

[42] S. Goss and F. Fry, "High intensity ultrasonic treatment of tumors," *Proc. IEEE 1982 Ultrason. Symp.*, 1982.

[43] S. Umemura and C. Cain, "Evaluation of a prototype sector-vortex array applicator," *Proc. IEEE 1987 Ultrason. Symp.*, 1987.

[44] F. Kremkau, "Cancer therapy with ultrasound: A historical review," *J. Clin. Ultrasound*, vol. 7, pp. 287-300, 1979.

[45] H. Underwood, E. Burdette, K. Ocheltree and R. Magin, "A multi-element ultrasonic hyperthermia applicator with independent element control," *Int. J. Hyperthermia*, vol. 3, no. 3, pp. 257-267, 1987.

[46] P. Lele, "Effect of ultrasound on solid mammalian tissues and tumors in vivo," in *Ultrasound.* M. Rapacholi, M. Grandolfo, and A. Rindi Ed.. New York: Plenum Publishing Corp., 1987.

[47] F. Storm, "Background, principles, and practice," in *Hyperthermia in Cancer Therapy.* F. Storm, Ed., Boston, MA: G. K. Hall Medical Publishers, 1983.

[48] J. Dickson and S. Calderwood, "Temperature range and selective sensitivity of tumors to hyperthermia: A critical review," *Ann. N. Y. Acad. Science*, vol 355, p. 180, 1980.

[49] S. Umemura and C. Cain, "The sector-vortex phased array: Acoustic field synthesis for hyperthermia," *IEEE Trans. Ultrasonics Ferroelectrics Frequency Control*, vol. 36, no. 2, pp. 249-257, 1989.

[50] W. Nyborg et al. "Biological effects of ultrasound: mechanisms and clinical implications," NCRP Report no. 74, 1983.

[51] K. Ocheltree and L. Frizzel, "Sound field calculation for rectangular sources," *IEEE Trans. Ultrasonics Ferroelectrics Frequency Control*, vol. 36, no. 2, pp. 242-248, 1989.

[52] E. Moros, R. Roemer, and K. Hynynen,"Simulations of scanned focused ultrasound hyperthermia: The effects of scanning speed and pattern on the temperature fluctuations at the focal depth," *IEEE Trans. Ultrasonics Ferroelectrics Frequency Control*, vol. 35, no. 5, pp. 552-560, 1988.

[53] M. Ibbini, E. Ebbini, and C. Cain, "Ultrasound phased arrays for hyperthermia: New techniques based on the field conjugation method," *Proc. IEEE 1987 Ultrason. Symp.*, pp. 863-866, 1987.

[54] L. Potter and A. Arun, "Energy concentration in bandlimited extrapolation," *IEEE Trans. Acoust, Speech, Signal Processing*, vol. 37, no. 7, pp. 1027-1041, 1989.

[55] T. Huang, J. Sanz, H. Fan, J. Shafii,and B. Tsai, "Numerical comparison of several algorithms for bandlimited extrapolation," *J. Appl. Optics*, vol. 23, pp. 307-317, Jan. 1984.

[56] A. Tikhonov and V. Arsenin (Trans. F. John), *Solutions of Ill-Posed Problems.* Washington, DC: Winston, 1977.

[57] S. Umemura and C. Cain, "Theoretical study of acoustic and thermal fields generated by phased array systems," *Proc. 5th International Symposium on Hyperthermic Oncology*, vol. 2, pp. 674-677, 1989.

[58] W. Brogan, *Modern Control Theory.* New Jersey: Prentice-Hall, 1985.

[59] A. Schell and A. Ishimaru, Chapter 7 in *Antenna Theory, Part 1*, Collin and Zucker Eds., New York: McGraw-Hill, 1969.

[60] J. Proakis and D. Manolakis, *Introduction to Digital Signal Processisng.* New York: Macmillan Publishing Company, 1988.

[61] B. Van Veen and K. Buckley, "Beamforming: A versatile approach to spatial filtering," *IEEE Acoust. Speech, Signal Processing Magazine*, vol. 5, no. 2, pp. 4-24, 1988.

[62] M. Orstaglio and G. Hohmann, "Diffusion of electromagnetic fields into two-dimensional earth: A finite- difference approach," *Geophysics*, vol. 49, no. 7, pp. 870-894., 1984.

[63] L. Lapidus and G. Pinder, *Numerical Solutions of Partial Differential Equations in Science and Engineering.* New York: John Wiley, 1982.

[64] A. Macovski, "Ultrasonic imaging using arrays," *Proc. of the IEEE*, vol. 67, no. 4, pp. 484-495, 1979.

[65] F. Jafary and P. Higgins, "Thermal modeling in cylindrical coordinates using effective conductivity," *IEEE Trans. Ultrasonics Ferroelectrics Frequency Control*, vol. 36, no. 2, pp. 191-196, 1989.

[66] L. Edelstein-Keshet, M. Dewhirst, J. Oleson and T. Samulski, "Characterization of tumour temperature distributions in hyperthermia based on assumed mathematical forms," *Int. J. Hyperthermia*, vol. 5, no. 6, pp. 757-777, 1989.

[67] R. Myerson, B. Emami, M. Pilepich, J. Fields, C. Perez, D. Von Gerichten, W. Straube, G. Nussbaum, L. Leybovich and A. Sathiaseelan, "Physical predictors of adequate hyperthermia with the annular phased array," *Int. J. Hyperthermia*, vol. 5, no. 6, pp. 749-755, 1989.

[68] G. Hahn, "Potential for therapy of drugs and hyperthermia," *Cancer Research*, vol. 39, pp. 2264-2268, 1979.

[69] L. LI, G. Shen, H. Zhang and D. Li, "Enhancement of nitrocaphane cytotoxicity by hyperthermia in vitro," *Int. J. Hyperthermia*, vol. 5, no. 4, pp. 525-533, 1989.

[70] R. Jain, "Bioheat transfer: Mathematical models of thermal systems," Ch. 2 in *Hyperthermia in Cancer Therapy.* F. Storm, Ed., Boston, MA: G. K. Hall Medical Publishers, 1983.

[71] E. Seppi, E. Shapiro, L. Zitelli, S. Henderson, A. Wehlau, G. Wu and C. Ditmar, " A large aperture ultrasonic array system for hyperthermia of deep-seated tumors," *Proc. IEEE Ultrasonics Symposium*, pp. 942-948, 1985.

[72] S. Goss, R. Johnston and F. Dunn, "Compilation of empirical ultrasonic properties of mammalian tissues: II," *J. Acoust. Soc. Amer.*, vol. 68, p.93, 1980.

[73] E. Ebbini, F. Ngo and C. Cain, "The pseudoinverse pattern synthesis method: Experimental verification using a prototype cylindrical-section ultrasound hyperthermia phased array applicator," *Proc. IEEE Ultrasonics Symposium*, 1989, in press.

[74] F. Ngo, E. Ebbini and C. Cain, "An experimental analysis of a sector vortex array prototype," *Proc. IEEE Ultrasonics Symposium*, 1989, in press.

[75] M. Ibbini, E. Ebbini and C. Cain, "NxN square- element ultrasound phased array applicator: Simulated temperature distributions associated with directly synthesized heating patterns," *IEEE Trans. Ultrasonics Ferroelectrics Frequency Control*, accepted for publication.

[76] C. Rushforth, "Signal restoration, functional analysis, and Fredholm integral equations of the first kind." Ch. 1 in *Image Recovery.* H. Stark Ed., Florida: Academic Press, 1987.

VITA

Emad S. A. Ebbini was born in Karak, Jordan, on December 1, 1961. He enrolled at the University of Jordan, Amman, Jordan, in 1980 where he obtained a B.Sc. degree in Electrical Engineering in 1985. During the summer of 1984, he was a trainee student at ASEA, Sweden. He also worked as a laboratory instructor at the University of Jordan (Fall 1984 - Spring 1985). From 1985 to 1986 he was a full-time graduate student and teaching assistant at Yarmouk University, Irbid, Jordan. In 1986 he enrolled at the University of Illinois at Urbana-Champaign. Under the supervision of Professor Charles A. Cain, he obtained his M. S. degree in Electrical Engineering in 1987. Mr. Ebbini is a member of IEEE and of the North American Hyperthermia Group. His current research interests are in the area of medical ultrasonics. His publications include

1. Emad S. Ebbini, S. Umemura, M. Ibbini, and C. A. Cain, "A cylindrical-section ultrasound phased-array applicator for hyperthermia cancer therapy," *IEEE Trans. Ultrasonics Ferroelectrics Frequency Control*, vol 35, no. 5, Sep 1988.

2. Emad S. Ebbini and Charles A. Cain, "Multiple-focus ultrasound phased-array pattern synthesis: optimal driving-signal distributions for hyperthermia," *IEEE Trans. Ultrasonics Ferroelectrics Frequency Control*, vol. 36, no. 5, 1989.

3. M. Ibbini, E. S. Ebbini, and C. A. Cain, "Ultrasound Phased arrays for hyperthermia: new techniques based on the field conjugate method," *Proc. 1987 Ultrasonics Symposium*, pp. 863-866, 1987.

4. E. S. Ebbini, M. Ibbini, and C. A. Cain, "An inverse method for hyperthermia phased array pattern synthesis," *Proc. 1988 Ultrasonics Symposium*, 1988.

5. H. Houshmand, R. McGough, E. Ebbini, H. Lee, and C. Cain, "Ultrasonic transmission mode imaging of the nonlinear parameter B/A: A simulation study," *Proc. 1988 Ultrasonics Symposium*, 1988.

6. C. A. Cain, S. Umemura, M. Ibbini, and E. Ebbini, "Ultrasound phased-array hyperthermia applicators," *Proc. IEEE EMBS Symposium*, 1988.

7. C. A. Cain, M. Ibbini, E. Ebbini, and S. Umemura, "Ultrasound phased arrays for synthesis of precision hyperthermia heating patterns: An alternative to mechanical scanning," *Proc. 1988 International Symposium on Hyperthermic Oncology*, 1988.

8. H. Wang, E. Ebbini, and C. Cain, "On-line algorithms for control of ultrasound phased array hyperthermia applicators based on a pseudoinverse method," *IEEE Trans. Ultrasonics Ferroelectrics Frequency Control*, accepted for publication.

9. M. Ibbini, E. Ebbini, and C. Cain, "$N \times N$ square- element ultrasound phased array applicator: Simulated temperature distributions associated with directly synthesized heating patterns," submitted to *IEEE Trans. Ultrasonics Ferroelectrics Frequency Control.*

10. E. Ebbini, F. Ngo, and C. Cain, "The pseudoinverse pattern-synthesis method: Experimental verification using a prototype cylindrical-section ultrasound hyperthermia phased-array applicator," *Proc. IEEE 1989 Ultrasonics Symposium*, in press.

11. F. Ngo, E. Ebbini, and C. Cain, "An experimental analysis of a modified sector-vortex phased array applicator for ultrasound hyperthermia," *Proc. IEEE 1989 Ultrasonics Symposium*, in press.